DEVELOPMENT OF METAL PHOSPHATE INCORPORATED POLYANILINE ELECTRODES FOR SUPERCAPATTERY

FATIN SAIHA BINTI OMAR

THESIS SUBMITTED IN FULFILMENT
OF THE REQUIREMENTS FOR THE DEGREE OF
DOCTOR OF PHILOSOPHY

DEPARTMENT OF PHYSICS
FACULTY OF SCIENCE
UNIVERSITY OF MALAYA
KUALA LUMPUR

2018

UNIVERSITY OF MALAYA

ORIGINAL LITERARY WORK DECLARATION

Name of Candidate: **FATIN SAIHA BINTI OMAR**
Matric No: **SHC 14**
Name of Degree: **DOCTOR OF PHILOSOPHY**
Title of Thesis:
DEVELOPMENT OF METAL PHOSPHATE INCORPORATED POLYANILINE ELECTRODES FOR SUPERCAPATTERY
Field of Study: **EXPERIMENTAL PHYSICS**

I do solemnly and sincerely declare that:

(1) I am the sole author/writer of this Work;
(2) This Work is original;
(3) Any use of any work in which copyright exists was done by way of fair dealing and for permitted purposes and any excerpt or extract from, or reference to or reproduction of any copyright work has been disclosed expressly and sufficiently and the title of the Work and its authorship have been acknowledged in this Work;
(4) I do not have any actual knowledge nor do I ought reasonably to know that the making of this work constitutes an infringement of any copyright work;
(5) I hereby assign all and every rights in the copyright to this Work to the University of Malaya (“UM”), who henceforth shall be owner of the copyright in this Work and that any reproduction or use in any form or by any means whatsoever is prohibited without the written consent of UM having been first had and obtained;
(6) I am fully aware that if in the course of making this Work I have infringed any copyright whether intentionally or otherwise, I may be subject to legal action or any other action as may be determined by UM.

Candidate’s Signature Date:

Subscribed and solemnly declared before,

Witness’s Signature Date:

Name:

Designation:

DEVELOPMENT OF METAL PHOSPHATE INCORPORATED POLYANILINE ELECTRODES FOR SUPERCAPATTERY

ABSTRACT

As the demand for green and sustainable energy increases, the advantages of high power density, instantaneous charge and discharge capabilities as well as long life span have made supercapacitor as one of the important device for energy storage and power supply management. Nevertheless, one of the main issues is their low energy density which has limit the employment of supercapacitors in broader applications. To address this issue, developing electrode materials that are efficient, cost-effective, tunable and have high surface area is an appealing alternative to boost the performance of supercapacitor (i.e. capable to store high charge and yet undergo minimal decayed during prolong life cycle). Herein, this work is reported on the synthesis of electrode materials and their relationships with supercapacitor performance. In this study, different nanostructures and morphologies of nickel phosphate $Ni_3(PO_4)_2$ have been prepared by sonochemical method followed by calcination (with different calcination temperatures). The crystallinity, purity, morphology and surface area of $Ni_3(PO_4)_2$ were authenticated by X-ray diffraction (XRD), fourier transform infrared (FTIR), field emission scanning electron microscopy (FESEM) and X-ray photoelectron spectroscopy (XPS) analysis. The electrochemical performances such as specific capacity, rate capability and electrical conductivity of the synthesized materials were studied through cyclic voltammetry (CV), galvanostatic charge-discharge (GCD) and electrochemical impedance spectroscopy (EIS) techniques. It was observed that the amorphous structure of $Ni_3(PO_4)_2$ renders in high specific capacity (539 C/g at the current density of 1 A/g)) mainly because of its highly porous structure that augmented the electroactive sites for redox reaction. Nevertheless, it exhibited low rate capability due to its poor electrical conductivity which motivated the incorporation of $Ni_3(PO_4)_2$ with silver (Ag) ions to form binary composite of nickel phosphate-silver phosphate nanocomposite ($Ni_3(PO_4)_2$-Ag_3PO_4). $Ni_3(PO_4)_2$-Ag_3PO_4 was prepared by fixing the amount of Ag precursor with various mass of $Ni_3(PO_4)_2$. Crystalline structure of Ag_3PO_4 nanoparticles were found to be intimately decorated on the surface of $Ni_3(PO_4)_2$ and had significantly improved the rate capability of the host $Ni_3(PO_4)_2$ from 29 to 78 % of capacity retention. Unfortunately at low current rate, the specific capacity achieved by $Ni_3(PO_4)_2$-Ag_3PO_4 was lower than that of $Ni_3(PO_4)_2$ with the specific capacity of 478 C/g at 1 A/g. $Ni_3(PO_4)_2$-Ag_3PO_4 was further blended with polyaniline (PANI) (synthesized by chemical oxidative polymerization of aniline monomer) without any binder to form tertiary composite of polyaniline-nickel phosphate-silver phosphate (PANI-$Ni_3(PO_4)_2$-Ag_3PO_4). The specific capacity shown by PANI-$Ni_3(PO_4)_2$-Ag_3PO_4 was increased to 677 C/g at 1 A/g with the rate capability of 76 % capacity retention. Overall, the improved performance displayed by PANI-$Ni_3(PO_4)_2$-Ag_3PO_4 electrode is attributed to (i) the utilization of the surface area from each material for the effective redox reaction, (ii) the presence of Ag_3PO_4 nanoparticles which increased the electrical conductivity and (iii) tubular shape of conductive PANI that support $Ni_3(PO_4)_2$-Ag_3PO_4, providing the interconnected paths for quick electron transfer rate and preventing closely packed of $Ni_3(PO_4)_2$-Ag_3PO_4 particles. For real application, PANI-$Ni_3(PO_4)_2$-Ag_3PO_4 was fabricated into hybrid supercapacitor (PANI-$Ni_3(PO_4)_2$-Ag_3PO_4//activated carbon) and obtained energy density of 38.9 Wh/kg at 400 W/kg with 88 % capacity retention after 5000 cycles.

Keywords: supercapacitor, polyaniline, metal phosphate, electrode materials

PEMBANGUNAN ELEKTROD HASIL CAMPURAN LOGAM FOSFAT DAN POLYANILINE UNTUK SUPERKAPATERI

ABSTRAK

Memandangkan permintaan terhadap peningkatan tenaga hijau dan mampan, kelebihan ketumpatan kuasa tinggi, keupayaan muatan dan pelepasan segera serta jangka hayat yang panjang telah menjadikan superkapasitor sebagai salah satu peranti penting bagi penyimpanan tenaga dan pengurusan bekalan kuasa. Walau bagaimanapun, salah satu isu utama adalah ketumpatan tenaga yang rendah yang membatasi penggunaan superkapasitor dalam aplikasi yang lebih luas. Untuk menangani masalah ini, membangunkan bahan-bahan elektrod yang cekap, kos efektif, merangkumi dan mempunyai permukaan permukaan yang tinggi adalah alternatif menarik untuk meningkatkan prestasi supercapacitor (iaitu berupaya untuk menyimpan caj yang tinggi dan masih mengalami kerosakan yang minimum semasa memanjangkan kitaran hayat). Di sini, karya ini dilaporkan pada sintesis bahan elektrod dan hubungan mereka dengan prestasi supercapacitor. Dalam kajian ini, pelbagai struktur nano dan morfologi nikel fosfat ($Ni_3(PO_4)_2$) telah disediakan oleh kaedah sonokimia diikuti dengan penalaan (dengan suhu kalsinasi yang berbeza). Kelakuan kristal, kesucian, morfologi dan kawasan permukaan $Ni_3(PO_4)_2$ telah disahkan oleh analisis pembelauan xinar-X (XRD), transformasi empatier inframerah (FTIR), mikroskop elektron pengimbasan emisi lapangan (FESEM) dan sinaran-X fotoelektron spectroskopi (XPS). Persembahan elektrokimia seperti keupayaan khusus, keupayaan kadar dan kekonduksian elektrik bahan-bahan yang disintesis telah dikaji melalui teknik kitaran voltametri (CV), teknik pelepasan caj galvanostatik (GCD) dan teknik spektroskopi impedans elektrokimia (EIS). Ia diperhatikan bahawa struktur amorf $Ni_3(PO_4)_2$ menghasilkan kapasiti khusus yang tinggi (539 C/g pada ketumpatan semasa 1 A/g)) terutamanya kerana strukturnya yang berliang yang menambah tapak elektroaktif untuk reaksi redoks. Walau bagaimanapun, ia memperlihatkan keupayaan kadar yang rendah disebabkan oleh kekonduksian elektriknya yang rendah yang memotivasi penggabungan $Ni_3(PO_4)_2$ dengan ion perak (Ag) untuk membentuk komposit bineri nikel fosfat-perak fosfat ($Ni_3(PO_4)_2$-Ag_3PO_4). $Ni_3(PO_4)_2$-Ag_3PO_4 telah disediakan dengan menetapkan jumlah prekursor Ag dengan jisim yang berlainan $Ni_3(PO_4)_2$. Struktur kristal dari zarah nano Ag_3PO_4 didapati dihiasi dengan intim di permukaan $Ni_3(PO_4)_2$ dan telah meningkatkan keupayaan kadar $Ni_3(PO_4)_2$ dari 29 hingga 78 % dari pengekalan kapasiti. Malangnya pada kadar yang rendah, kapasiti khusus yang dicapai oleh $Ni_3(PO_4)_2$-Ag_3PO_4 adalah lebih rendah daripada $Ni_3(PO_4)_2$ dengan kapasiti khusus 478 C/g pada 1 A/g. $Ni_3(PO_4)_2$-Ag_3PO_4 komposit nano digabungkan dengan polyaniline (PANI) (disintesis oleh pempolimeran oksidatif kimia monomer aniline) tanpa sebarang pengikat untuk membentuk komposit tertiari polyaniline-nikel fosfat-perak fosfat (PANI-$Ni_3(PO_4)_2$-Ag_3PO_4). Kapasiti khusus yang ditunjukkan oleh PANI-$Ni_3(PO_4)_2$-Ag_3PO_4 meningkat kepada 677 C/g pada 1 A/g dengan kemampuan kadar pengekalan kapasiti 76 %. Secara keseluruhannya, peningkatan prestasi yang ditunjukkan oleh elecktrod PANI-$Ni_3(PO_4)_2$-Ag_3PO_4 komposit nano adalah disebabkan oleh (i) penggunaan tapak elektroaktif untuk reaksi redoks yang berkesan, (ii) kehadiran zarah nano Ag_3PO_4 yang menawarkan kekonduksian elektrik yang meningkat dan (iii) bentuk tiub konduktif PANI yang menyokong $Ni_3(PO_4)_2$-Ag_3PO_4 komposit nano yang menyediakan jalur yang saling berkait untuk kadar pemindahan elektron pesat dan menghalang $Ni_3(PO_4)_2$-Ag_3PO_4 yang rapat. Untuk aplikasi sebenar, PANI-$Ni_3(PO_4)_2$-Ag_3PO_4 telah direka sebagai superkapasitor hibrid (PANI-$Ni_3(PO_4)_2$-Ag_3PO_4//diaktifkan karbon) dan memperoleh kepadatan tenaga 39 Wh/kg pada 400 W/kg dengan 88 % pengekalan kapasiti selepas 5000 kitaran.

Kata kunci: superkapasitor, polyaniline, logam fosfat, bahan elektrode

ACKNOWLEDGEMENTS

First and foremost, I pay my obeisance to God Almighty, for His showers of blessings and strength given to me to undertake this research study.

I would like to express my deep and sincere gratitude to my supervisors, Professor Dr. Ramesh T. Subramaniam and Associate Professor Dr. Ramesh Kasi, for giving me the opportunity to do my Ph.D research under their guidance. Their constant encouragement, patience, continuous support, and vision have inspired me and I am grateful for whatever they have offered me. I am extending my thanks to Dr. Navaneethan Duraisamy for his scientific advice, positiveness, research ideas and insightful discussion in my work. I will never forget that he was my first resource for getting my scientific question answered during the initial phases of the thesis work. I owe my sincere gratitude to Dr. Numan Arshid, who taught me about supercapacitor, and gave critical comments and suggestions for both in my published papers and in this thesis. His motivation and sharing of knowledge have been very helpful for this study.

My research colleagues, Khuzaimah Aziz, Shairah Saidi, Dr. Lu, Dr. Shahid Mehmood, Dr. Shahid Bashir, Suresh, Steven, Vhaiss, Dr. Vicky, and Dr. Chong Mee Yoke also deserve a sincere thank you for creating a wonderful lab environment and their innumerable assistance throughout my study duration. My sincere appreciation also goes to all the staffs of Physics Department; Mr. Amir, Mrs. Endang, Mr. Mohamad Arof, Mr. Ismail Che Lah and Mr. Ismail Jaafar for their kindness and assistance for my sample characterizations and material purchases. I am also immensely indebted and very grateful for the support of my beloved family members especially my parents, to whom I dedicated this thesis. I would not be where I am now without the love, understanding and endless support from them.

TABLE OF CONTENTS

LIST OF FIGURES

LIST OF TABLES

LIST OF SYMBOLS AND ABBREVIATIONS

E_d : Energy density

IR_{drop} : Current drop

m : Mass

OH^- : Hydroxide ions

P_d : Power density

Q_S : Specific capacity

R_{ct} : Charge transfer

ν : Scan rate

V : Voltage

W_d : Warburg impedance

Z' : Real impedance

$Z"$: Imaginary impedance

AC : Activated carbon

Ag_3PO_4 : Silver phosphate

APS : Ammonium peroxydisulfate

CV : Cyclic voltammetry

EDLC : Electric double layer capacitor

EES : Electrochemical energy storage

EIS : Electrochemical impedance spectroscopy

ESR : Equivalent series resistance

FESEM : Field emission scanning electron microscopy

FTIR : Fourier transform infrared spectroscopy

GCD : Galvanostatic charge discharge

HRTEM : High resolution transmission electron microscopy

MnO_2	:	Manganese oxide
$Ni_3(PO_4)_2$	:	Nickel phosphate
PANI	:	Polyaniline
RuO_2	:	Ruthenium oxde
XPS	:	X-ray photoelectron spectroscopy
XRD	:	X-ray diffraction

CHAPTER 1: INTRODUCTION

1.1 Background of research

To date, the emission of carbon dioxide have dramatically increased by about 90 % since 1970, and 78 % of the total release of greenhouse gases is contributed from the usage of fossil fuels and industrial emission. In recent decades, countries worldwide are urged to take substantial steps towards creating less carbon dioxide emissions due to its impact to the climate change. Realized that the implementation of renewable energy would decarbonize the world energy production, energy research has concentrated on hydropower, biomass, solar panel and wind turbine to reduce reliance on fossil fuels. However, solar and wind power is intermittent nature which could not guarantee the constant supply of energy to meet consumer demand, and any surplus power may be thrown away if it is not stored. This has led to an increased call for the deployment of energy storage as a backup if the energy generated by solar or wind is less or higher than expected.

Energy storage devices play a major role in providing uninterrupted and stable energy supply. The integration of energy storage device between renewable energy source and power grid can balance out the inconsistent power supply from the renewable energy source and able to satisfy the fluctuation energy demands. Lithium-ion battery (LIB) which is the most common form of energy storage device offers an outstanding energy density but its low power density (0.1-1 kW/kg) risks its service life and may cause explosion when overheated or overcharged. On the other hand, supercapacitor which is also called as electrical double layer capacitor (EDLC) has been known as an ideal device that can satisfies the applications that require fast bursts of energy due to its great power density (1-10 kW/kg), but it suffers from unsatisfactory energy density.

One of the strategy to bridge the energy/power density gap between LIB and EDLC is to develop hybrid device, called supercapattery. Supercapattery is latest version of energy storage which combine capacitive- and battery-type electrode into one device. It is designed to utilize the different charge storage mechanisms from both types of electrodes so that it could store high energy (compared to EDLC) while retaining its power density and cycle life. However, the exploration for better performance of supercapattery is highly pivotal. Electrode material is the main pillar in supercapattery which is responsible for energy storage mechanism. Thus, many efforts have been focused on the development of highly efficient nano-sized electrode materials. Generally, nano-sized materials can enhance the energy density of supercapattery by maximizing the interfacial area between electrode and electrolyte. Nevertheless, another challenge is to obtain fast charge/discharge rates without any significant capacitance decay under prolonged cycling. Thus, the nano-sized materials can be optimized through the synthesis of nanocomposite materials as well as the modification of material surface and structure.

Currently, commercial EDLCs use two identical carbon-based materials (known as capacitive material) (e.g. activated carbon, carbon nanotube and graphene) as the electrode materials. These materials guarantee high power density of EDLCs due to its low ionic and electronic charging resistance. Nonetheless, the specific capacitance exhibited is low, results in low energy density of EDLC. Ruthenium oxide which is the best pseudocapacitor material inherent high electrical conductivity and achieves large specific capacitance approaching its theoretical value. However, it is expensive and environmental toxic which restrain its commercial application. In this aspect, the option is to explore phosphate-based materials (recognized as battery-type material) as the potential electrode materials as they are safe, cheap and has high redox properties. Therefore, in this research, nickel phosphate ($Ni_3(PO_4)_2$) was synthesized using sonochemical and subsequent calcination (with various calcination temperature) and its performance in electrochemical experiment was studied. $Ni_3(PO_4)_2$ especially in its amorphous structure not only contain phosphate polyanions which can ensure higher redox reactions than metal oxide, but also has porous structure which can shorten the pathways for the electrolyte ions diffusion. However, $Ni_3(PO_4)_2$ displayed poor electrical conductivity, which can affect the rate capability of electrode. Thereby, the electrical conductivity of $Ni_3(PO_4)_2$ can be elevated by the incorporation of lower band gap of silver phosphate (Ag_3PO_4) to form binary nanocomposite of nickel phosphate-silver phosphate ($Ni_3(PO_4)_2$-Ag_3PO_4). To further boost the electrochemical performance of $Ni_3(PO_4)_2$-Ag_3PO_4, it can be amalgamated with conducting nature of polyaniline (PANI) to form tertiary nanocomposite of polyaniline-nickel phosphate-silverphate (PANI-$Ni_3(PO_4)_2$-Ag_3PO_4). A compromise between the surface area (to enhance redox reaction), porosity (to shorten the length of ions diffusion) and electrical conductivity (to alleviate the internal resistance of the materials) is discussed. The synthesized materials were fabricated into battery-type electrode for supercapattery evaluation.

1.2 Hypothesis

1) Metal phosphate in its amorphous phase is anticipated to give high energy density as compared to its crystalline phase as supercapattery electrode. This is mainly attributed to the high number of structural defects, which can serve as reversible active sites, and abundance of inner pores that can facilitate the penetration of ions throughout its disordered structure.

2) High band gap of nickel phosphate results in poor rate capability of supercapattery. However, this shortcoming can be improved by the incorporation with another metal phosphate that has comparatively narrower band gap to form composite. The

interfacial resistance of the composite material can be alleviated due to high number of efficient electron transfer between the two metal phosphates.

3) Polyaniline can be easily incorporated with nanoparticles by facile physical blending method to form nanocomposites. The development of nanocomposites can lead to the synergetic effect between electrical conductivity and redox properties on polyaniline based nanocomposites.

1.3 Aim and objectives of research

The primary goal of this work is to establish the quantitative understanding on the effect of material structure, morphology and electrical conductivity on electrochemical behaviour and supercapacitor performance, which would benefit future electrode design. In order to achieve this goal, following major objectives were established and achieved;

1) To synthesize different structure and morphology of $Ni_3(PO_4)_2$ using sonochemical with subsequent calcination method (with different temperature).
2) To characterize $Ni_3(PO_4)_2$ using various techniques such as X-ray diffraction (XRD), X-ray photoelectron spectroscopy (XPS), fourier transform infrared spectroscopy (FTIR), field emission scanning electron microscopy (FESEM) and high-resolution transmission electron microscopy (HRTEM).
3) To analyse and propose the possible mechanism behind the electrochemical performance of $Ni_3(PO_4)_2$ via different analysis techniques; cyclic voltammetry (CV), galvanostatic charge discharge (GCD) and electrochemical impedance spectroscopy (EIS).
4) To improve the properties and electrochemical performance of $Ni_3(PO_4)_2$ by incorporating the optimized $Ni_3(PO_4)_2$ with Ag_3PO_4 and PANI to form nanocomposites.

5) To assemble supercapattery and assess its performances in terms of energy density, power density and cyclic stability.

1.4 Outlines of thesis

This thesis is consists of six chapters. Chapter one exemplifies the research background, hypothesis, goal, and objectives of the work. Chapter two presents the literature review on metal phosphates (including $Ni_3(PO_4)_2$ and Ag_3PO_4), conducting polymers (focussing on PANI), different mechanisms of charge storage by electrode materials, different types of supercapacitor including supercapattery and the synthesis technique used to prepare electrode materials. Chapter three demonstrates the synthesis steps of electrode materials and the electrochemical techniques used to evaluate the performance of the fabricated electrodes. Chapter four discusses the characterization and electrochemical performance results as well as the proposed mechanism of surface reaction at the electrode material. For both chapter three and four start with the characterization results and electrochemical performance of polyaniline-zinc cobaltite (PANI-$ZnCo_2O_4$) nanocomposite before proceed with the works on $Ni_3(PO_4)_2$, Ag_3PO_4 and PANI-$Ni_3(PO_4)_2$-Ag_3PO_4. The purpose of including work on PANI-$ZnCo_2O_4$ in this thesis is to show the improvement in specific capacity, rate capability and stability exhibited by PANI based metal phosphate nanocomposite as compared to PANI based metal cobaltite nanocomposite. The comparison between each system discussed in chapter four was reviewed in the chapter five. And finally chapter six concludes the whole thesis and proposes the future work.

CHAPTER 2: LITERATURE REVIEW

This chapter reviews the different types of supercapacitors and the electrodes based on different charge storage mechanisms. Nanostructure materials with different crystal structure which play a significant role in supercapacitor also discussed. In addition to this, a literature on phosphate based materials and conducting polymers, especially polyaniline are explained. The final section of this chapter presents the synthesis techniques for the preparation of electrode materials used in this research.

2.1 Supercapacitors

2.1.1 History of supercapacitors

The concept of storing charge at the interface of electrolyte and solid material was first discovered in the late 1800s. In the early 1950s, General Electric researchers experimented two-terminal device with porous carbon electrodes. This led to Becker patented the electrolytic capacitor with porous carbon electrodes after discovered its exceptionally high capacitance without understand its energy storage principle. However, the works did not pursue until Standard Oil of Ohia (SOHIO) invented the first supercapacitor. Unfortunately, SOHIO failed to commercialize the technology and eventually licensed it to Nippon Electric Company (NEC) who eventually marketed the invention under the name of “supercapacitor” in 1978. The commercialized supercapacitors were rated at 5.5 V (with the capacitances up to 1 F) and were used as backup power for computer memories. In 1980, Russian company called ELIT designed the first asymmetric supercapacitors and symmetric supercapacitor in the following year. From 1975 to 1980, Conway worked on the application of ruthenium oxide (RuO_2) for supercapacitors and found the difference in electrochemical storage mechanism between supercapacitors and batteries in 1991. The history of supercapacitor is illustrated in Figure 2.1.

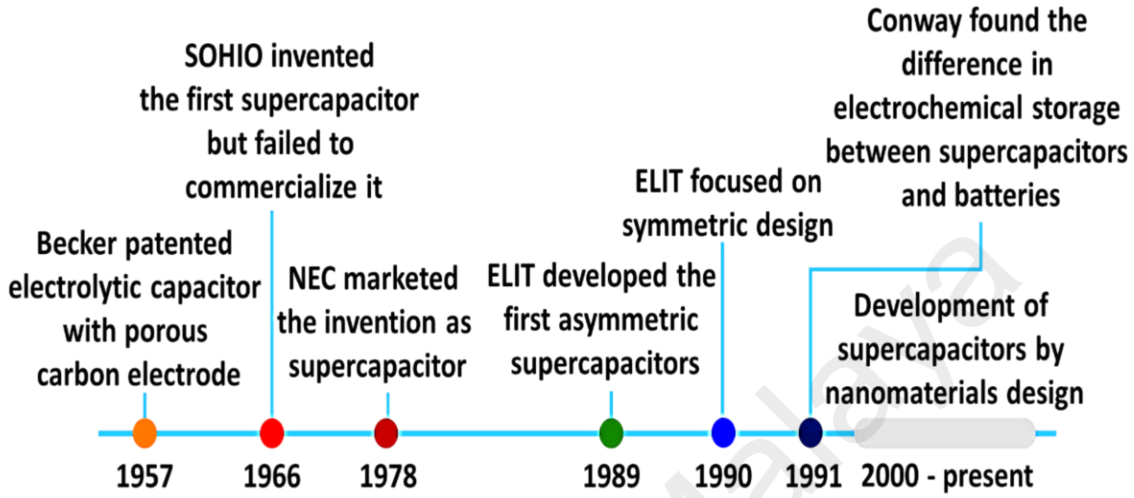

Figure 2.1: Timeline presenting the important phases in supercapacitors progress.

2.1.2 Supercapacitor components

Supercapacitors are constructed by a combination of two conductive electrodes that are separated by a molecule-thin layer of electrolyte separator. Unlike capacitors which use metal plates as the electrodes and store charge at the dielectric layer, supercapacitors store charge at the electrode material-electrolyte interface.

2.1.1.1 Electrolytes

Electrolytes are used to provide ions for charge transportation. Generally, electrolytes should guarantee wide potential window, high ionic conductivity, electrochemically stable, low resistivity and high wettability in order to afford an excellent performance of supercapacitors. Electrolytes can be categorized into three classes; aqueous electrolytes, organic electrolytes and liquid salts (also known as ionic liquids). Aqueous electrolytes such as potassium hydroxide (KOH) and sulphuric acid (H_2SO_4) are mostly used for alkaline and acidic electrolyte, respectively. However, acidic electrolytes can dissolute the electrode materials and can corrode the device (Balakrishnan & Subramanian, 2014). The maximum operating voltage of supercapacitor is corresponding to the voltage at which the electrolyte undergoes electrochemical reactions. For instance, the voltage of supercapacitor utilizing aqueous electrolytes is ~1 V while for organic electrolyte is ~3-3.5 V, depending on the device operating temperature. For supercapacitors that storing energy through faradaic reactions, the redox activity and ionic conductivity can be enhanced by adding redox active species (e.g. quinones, phenylamide and halide ions) into the electrolytes.

2.1.1.2 Electrodes

Supercapacitor electrodes are fabricated by coating current collector with active materials such as carbonaceous materials, metal oxides, conducting polymers etc. The current collector (e.g. nickel foam, nickel foil and aluminium foil) functions to conduct electron from the electrode material, and it must be electrochemically inactive in the cell environment. The electrode can be fabricated by physically coating the current collector with active material in the presence of polymer binder or chemically grow the material on the current collector during material synthesis. The fabrication of electrode is crucial as it is one of the factor to the high/low value of equivalent series resistance (ESR).

2.1.3 Electrodes with different charge storage mechanisms

The performance of supercapacitor is varied in several ways including charge storage mechanism, type of electrode material (different type of materials have different charge storage mechanisms), type of electrolyte and the design of the device. The interaction between the electrolyte ion with the electrode material is highly influence the efficiency of supercapacitor. The good properties of electrode material depend on several criteria such as surface area or porosity, ionic and electrical conductivity as well as chemical stability.

Understanding of charge/ion transport mechanisms is important as this develops a strong basis for analysing the electrochemical performance and fabrication of devices. Electrodes can be distinguished into three types based on different charge storage mechanisms (i.e. electrostratic (non-faradaic) and faradaic reactions); (i) supercapacitive, (ii) pseudocapacitive and (iii) battery-type electrodes. Commonly, capacitive and pseudocapacitive electrodes provide greater rate capability but lower charge storage capacity than battery-type electrodes (depending on the physico-chemical properties of electrode material) because of their charge storage are based on surface reaction of the electrode. Whereas for battery-type electrodes, their charge storage process involve ion diffusion within the bulk of electrode materials (Wang et al., 2016). The difference in charge storage mechanism influences the shape of cyclic voltammetry (CV) and galvanostatic charge-discharge (GCD) curve as illustrated in Figure 2.2. The details of different electrode materials are explained in the following sections.

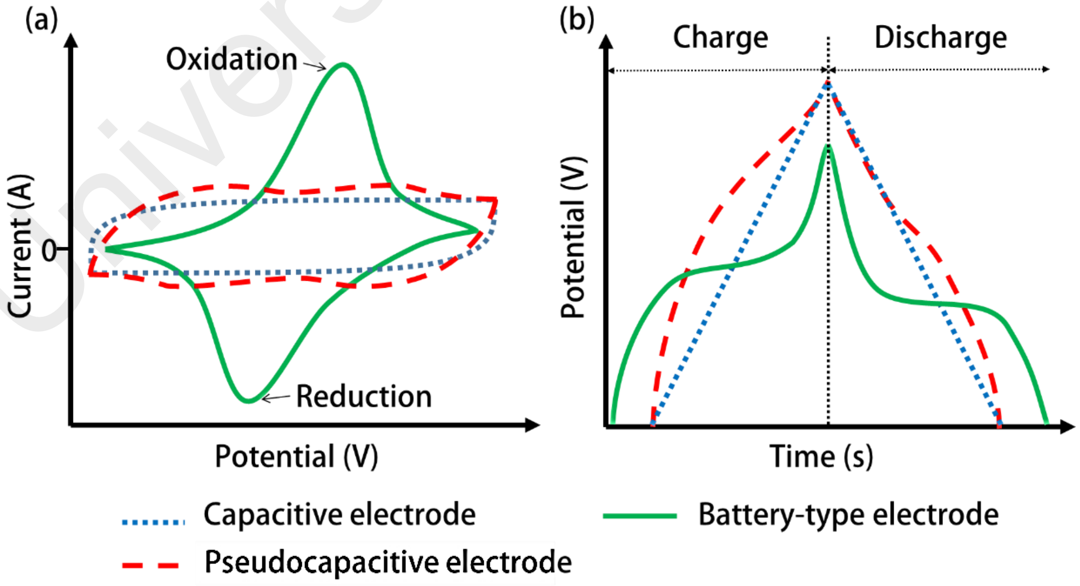

Figure 2.2: Influence of capacitive and faradaic charge storage on (a) CV and (b) GCD.

2.1.3.1 Capacitive electrode

Capacitive electrode stores charge electrostatically (i.e. non-faradaically) or through physical adsorption of electrolyte ions at the surface of electrode material in the absence of diffusion limitations. It can store higher charge than conventional electrode (capacitor metal plate electrode) because of the presence of the large surface area (1000 - 2500 m^2/g) of active materials (e.g. high porosity of activated carbon). Blue dotted line of CV and GCD curve (Figure 2.2) shows the capacitance is constant or independent over a fixed potential window. If the voltage is plotted against time as shown by GCD curve, capacitive electrode exhibits linear rectangular shape of curve during charging and discharging. There are several example of capacitive electrode materials such as activated carbons (ACs), carbon aerogels and carbon nanotubes (CNTs). The major advantages of these materials are low ionic and electronic charging resistance.

2.1.3.2 Pseudocapacitive electrode

Pseudocapacitive electrode stores charge through highly reversible faradaic reaction at the interface of electrode-electrolyte without limited by the diffusion process. The charge storage at the electrode involves fast electron transfer, hence, the specific capacitance of pseudocapacitive electrode is larger than capacitive electrode. The additional term of “pseudo” to “capacitive” describes to the behaviour of electrode materials that have the electrochemical signature of capacitve electrode. But as a matter of fact, the charge storage for pseudocapacitive electrode originates from redox reaction. The appearance of pseudocapacitive behaviour is influenced by the structure and conductivity of materials as well as their hydration properties. Basically, pseudocapacitance reaction can be categorized into three classes depending on the types of materials. First is underpotential deposition in which metal ions in electrolyte form an adsorbed monolayer on the electrode material surface. Second is redox capacitance where the electrolyte ions are adsorbed at or near the electrode material surface accompanied with the faradaic reaction. Third is intercalation pseudocapacitance where the electrolyte ions intercalates into the layers of the electrode material associated with faradaic reaction without affecting the crystal structure of the material (Wang et al., 2017).

Usually, transition metal oxides such as RuO_2, MnO_2, V_2O_5, SbO_2 and F_2O_3 exhibit pseudocapacitive reaction. The specific capacitance of these metal oxides depends on their structural and hydration (surface-bound water) properties. Conducting polymers (e.g. polypyyrole (Ppy), polyaniline (PANI) and poly3,4-ethylenedioxythiophene (PEDOT)) may also show the same behaviour but in a narrower potential range. In terms of performance, a pseudocapacitive electrode (dotted red line in Figure 2.2) displays the electrochemical signature of capacitive electrode with the additional of broad redox peak at CV, and the deviated from the linear rectangular shape of GCD curve. The pseudocapacitance is linearly dependent with the potential window of interest, but the difference is the charge storage originates from the faradaic reaction (Brousse & Daniel, 2015).

2.1.3.3 Battery-type electrode

Battery-type electrode often erroneously considered as pseudocapacitive electrode by many authors because of its charge storage also based on faradaic reaction. However, recently, few authors have critically reviewed the confusion that made by many reports on the wrong application of capacitance formula and “Farad (F)” unit on battery-type behaviour (Chen, 2017). In fact, battery-type electrode is considered as non-capacitive with purely faradaic behaviour and the process is rarely reversible. Typically, CV curve of battery-type electrode (solid green line in Figure 2.2) potrays the peak potential of oxidation and reduction shifted positively and negatively, respectively. While on GCD, the battery-type electrode exhibits non-linear curve with a flat discharge plateau (which is the reason of larger energy storage by battery than supercapacitor) due to the phase transformation of the electrode materials. For instance, some of transition metal oxides like Co_3O_4 and $NiCo_2O_4$ form metal oxyhydroxide during charging in an alkaline electrolyte and the reaction can be expressed in the equation below;

$$M_3O_4 + OH^- + H_2O \leftrightarrow 3MOOH + e^- \tag{2.1}$$

Where M is Co, Ni or combination of these. However, phase transformation of battery-type materials is diffusion limited which can cause to the distortion of the rate capability of the electrode. Because of its different electrochemical signature (i.e. inconstant capacity over the working potential window), the term of “capacity” with the unit of “Coulomb (C)” or “milliamp hour, mAh” are the appropriate units to use for calculating the stored charge in battery-type electrode instead of capacitance (Farad (F)) as used for capacitive and pseudocapacitive electrodes.

2.1.4 Different types of supercapacitors

The performance of supercapacitor is strongly dependent on the properties of electrode and electrolyte. As shown in Figure 2.3, supercapacitors can be designed into two different arrangements, symmetry (device with two identical electrodes/same charge storage mechanisms) and asymmetry (device with difference types of electrodes/difference charge storage mechanisms) designs. Electric double layer capacitors (EDLCs) and pseudocapacitors are categorized under symmetry while hybrid supercapacitor (specifically supercapattery) under asymmetry.

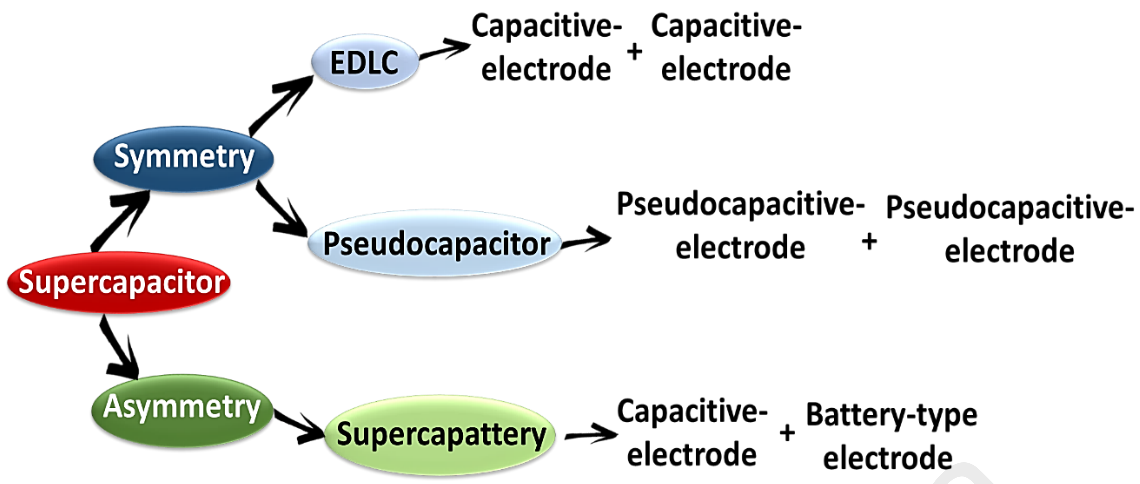

Figure 2.3: Classification of supercapacitors.

2.1.4.1 Electric double layer capacitor (EDLC)

EDLC uses two identical capacitive electrode, hence, it stores charge through instantaneous electrolyte ions separation towards the high porosity of electrode materials. When the EDLC is charged, cations and anions rapidly align themselves and diffuse toward negative and positive polarized electrodes, respectively. This process creates a thin electrical double-layer over the entire surface of electrode material. Technically, EDLC electrode has higher surface area than capacitor electrode (which only consists of metal plate) due to the presence of material that coated on the electrode surface. The generation of electrical double layer on the high surface area of electrode allow EDLC to store higher amount of energy than capacitor. When an EDLC is discharged, the electrolyte cations and anions will be diffused back from the electrode surface to the bulk electrolyte. Owing to the absence of electron transfer at the electrode-electrolyte interface, there is no chemical changes or compound formation happen in EDLC. Thus, the energy storage process in EDLC is highly reversible, leading to a very high power density and high degree of recyclability. However, the challenge for EDLC is it suffers from very low energy density as compared to batteries due to the charge storage is governed by electrostatic reaction.

Electrode materials for EDLC must possess high surface are so that more interaction between electrode and electrolyte can happen and more energy can be stored. Activated carbon (AC) and carbon nanotube (CNT) are the mostly used materials in commercial EDLC.

i) ACs have been mostly used as capacitive electrode materials due to their high porous structure and moderate cost. Porous structure of AC composed of different range of sizes; micropores (< 2 nm wide), mesopores (2 - 50 nm) and macropores (>50 nm). However, not all pores can be accessed by the electrolyte ions especially at high current rate. This is because of some electrolyte ions have larger size than the diameter of micropores of AC, thereby, full interaction between electrode material and electrolyte could not be achieved.

ii) CNTs have entangled structure, with an open network of mesopores (2 - 50 nm). The mesopores in CNTs are interconnected, providing continuous platform for the accessibility of the electrolyte ions. Even though CNTs have lower range of pore sizes than ACs, the surface area of CNTs are efficiently utilized by the electrolyte ions resulted comparable energy storage capability.

2.1.4.2 Pseudocapacitor

Another class of symmetry supercapacitor is pseudocapacitor. Unlike EDLC which stores energy via electrostatic reaction, pseudocapacitor stores energy faradaically by employing fast charge transfer at the electrode-electrolyte interface and this type of capacitance is called pseudocapacitance. Due to the existence of oxidation and reduction reaction during charging and discharging, pseudocapacitor could store 10 to 100 times higher energy than EDLC (Yan, 2015). Other mechanisms that can be employed by pseudocapacitor are electrosorption and intercalation as mentioned under Section 2.1.3.2. Briefly, those mechanisms involve the reaction with lattice structure of electrode materials without disturbing the chemical bonds of the materials.

Generally, there are two types of electrode materials that are commonly used in pseudocapacitors; metal oxides and conducting polymers.

i) Metal oxides

Among other metal oxides, ruthenium oxide (RuO_2) is widely studied as pseudocapacitor electrode material due to its conductivity and oxidation states. RuO_2 exhibits better performance in acidic electrolyte. Thus, the proposed theories of charge storage in literature mostly involves the intercalation of protons into RuO_2 structure. In its hydrous form (i.e. $RuO_2.H_2O_2$), the specific capacitance achieved is higher than carbon-based materials as well as conducting polymers with the maximum value of 1360 F/g. This is attributed to the presence of structural water crystal that facilitates ion diffusion into its inner surface. In addition, the fast redox reaction at the surface of $RuO_2.H_2O_2$ contributes to high power density which added another benefit of $RuO_2.H_2O_2$ (González et al., 2016). However, despite of its excellent performance, the usage of RuO_2 is too costly for practical applications. This issue motivates to the development of cheaper materials with comparable performance.

ii) Conducting polymers

Depending on the operating potential range, conducting polymers such as polypyrrole, polyaniline and polythiophene depict capacitance performance in a narrower potential range than typical pseudocapacitive electrode. If the potential window is extended to a wider range, oxidation and reduction peaks can be obviously seen in cyclic voltametry measurement. The appearance of these peaks indicates the involvement of faradaic reaction at the surface as well as at the interior site of the polymers during charging and discharging. The main drawback of using conducting polymers as bulk materials is their high stability is limited (typically not more than 1000 cycles) due to the physical changes (expanding and shrinking) during repeated charge-discharge cycles (Eftekhari et al., 2017).

2.1.4.3 Supercapattery

Symmetry supercapacitors which implement identical electrode materials (same material, mass, thickness and charge storage mechanism) such as EDLC and pseudocapacitor have narrower potential range (thus lower energy density) than batteries. On account of this, asymmetric device is designed by packing two different electrode materials with different charge storage mechanisms in one device in order to extend the operating potential window. This asymmetric design is called supercapattery (=**supercapa**citor + ba**ttery**) in which it usually employs capacitive material as negative electrode and battery-type material as positive electrode. The purpose of this design is to utilize both electrostatic reaction at the capacitive electrode and faradaic reaction at the battery-type electrode during charging and discharging process. Thus, higher energy and power density can be achieved than EDLC and pseudocapacitor. Typically, the CV and GCD plot of the supercapattery looks almost like the electrochemical signature of EDLC because of the combination of capacitive and faradaic behaviours. Figure 2.4 illustrates the different design of EDLC, pseudocapacitor and supercapattery.

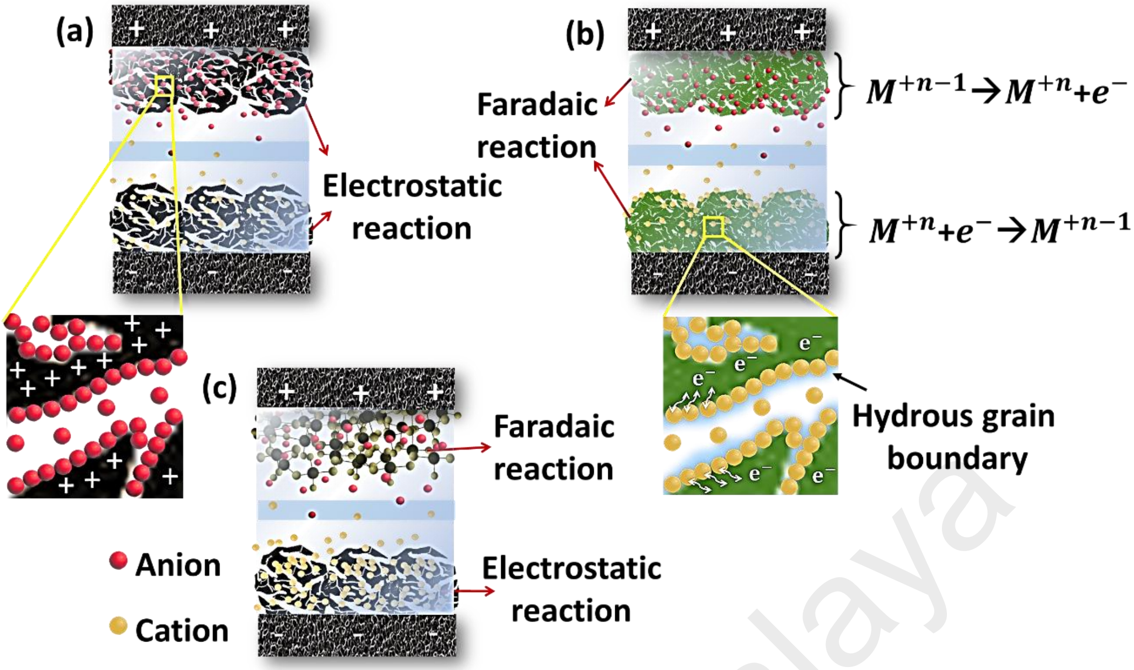

Figure 2.4: Schematic diagram of (a) EDLC (b) pseudocapacitor and (c) supercapattery.

2.1.5 Mechanism of charge storage in supercapacitor

When potential is applied across the device (charging), both connected electrodes become charged; positively and negatively charged electrodes. This causes anions and cations of electrolyte bulk attracted and moves toward the oppositely charge electrodes and induce electric field. At this stage, the device is storing energy. When the applied potential stop (discharging), the separated ions return from the electrode to the electrolyte bulk. The time taken for the electrolyte ions moves back to its initial state indicates how long the device can power the load (application). The slower the ion movements to move to its origin, the longer the device delivering energy. The higher the contact area between electrode material and electrolyte, the more electron transfer during charging and discharging can happen. The electrochemical reaction in general supercapacitor can be presented as (Bagotsky et al., 2015);

$$\text{Positive electrode: } E_S + A^- \leftrightarrow E_S^+//A^- + e^- \qquad (2.2)$$

Negative electrode: $E_S + C^+ + e^- \leftrightarrow E_S^-//C^+$ (2.3)

Overall reaction: $E_S + E_S + A^- \leftrightarrow E_S^-//C^+ + E_S^+//A^-$ (2.4)

Where E_S: the electrode surface, C^+: electrolyte cation and A^-: electrolyte anion

2.2 Nanomaterials with nanoscale structures

Nanotechnology is comprehensively refers to the designation, applications and systems in extremely small size of material, i.e. nano scale. Nanomaterials can be defined as the materials that having constituents of nano scale dimension. Nanomaterials have garnered great attention because of their unique size-dependent properties. One nanometer spans approximately 10 atoms and one may be able to rearrange matter with atomic precision to an intermediate size. In general, materials can be considered as nanomaterials if the materials meets at least one of the following criteria;

(i) consist of particles that have external dimensions in the range of 1 – 100 nm for more than 1 % of their number size distribution;

(ii) have interior structure in one or more dimensions in the range of 1 – 100 nm;

(iii) composed of a specific surface area larger than 60 m^2/cm^3.

Nanomaterials have the same chemical composition of their corresponding bulky-size, except the intrinsic properties due to the factor of size/surface to volume ratio. As presented in Figure 2.5, if bulk material is segmented into smaller size, the total collective surface area is significantly larger although the total volume remains the same. This means, as the dimension of material reduced, the density of atoms on the surface and surface to volume ratio increase significantly. Furthemore, the reduction of the size to nanoscale causes to the alteration of the electronic poperties of materials such as the energy bands and density of states which lead to the significant difference of the nanomaterials properties to the bulk materials.

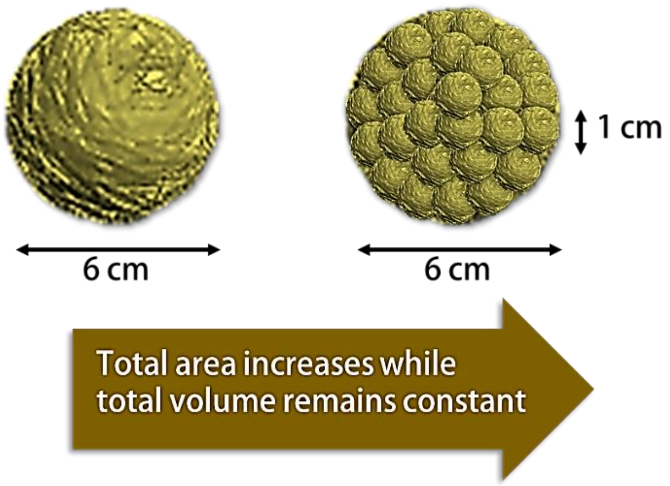

Figure 2.5: Comparison between bulk and collective nanomaterials.

In principle, nanomaterials can be employed in any bulk material-based applications. The question is whether nanomaterials can improve properties and performance or offer any advantages over bulk materials. The answer relies on the application of interest because not all cases nanomaterials are more advantageous. Thus, it is essential to determine in what situation nanomaterials should be used. Generally, nanomaterials can be synthesized with diverse morphologies and structures influenced by the experimental conditions (e.g. concentration of precursor, temperature, pH and size of vessel during synthesis reaction). For instance, too high in reaction concentration leads to particle coalescence, while too high in reaction temperature causes to particle aggregation.

The extraordinary properties and performance of nanomaterials can be manipulated by the nanostructured design. Nanomaterials can be classified into four different dimensions; zero dimension (0 D), one dimension (1 D), two dimension (2D) and three dimension (3 D) (Table 2.1).

Table 2.1: Different properties with different dimensions of nanomateials.

Dimension	Description
0	Materials with spherical-shape that have three dimensions constrained on the nanoscale. Nanoparticles have been demonstrated can improve the rate capability for batteries due to shorter ions diffusion paths. Example: fullerenes, quantum dots, nanoparticles, etc.
1	Materials in which their dimensions are dependent on their functional properties. They typically offer most of the advantages of the 0 D nanomaterial. Moreover, their longitudinal axis offers transport pathway for electrons and ions mobility. Example: nanotubes, nanowires, nanobelts, etc.
2	Ultrathin nanomaterials (thickness of a few atomic layer) with two dimensions outside of the nanometric size range. This structure can provides high number of spontaneous accessible electrochemically active sites at the surface or between layers. Example: nanosheets, nanowalls, branched structure, etc.
3	Bulk materials consist of nanoscale structures/building blocks. Materials with 3 D mesoporosity enables electrolyte deep penetration throughout the material which is favourable in energy storage applications. Example: mesoporous, flower-like, etc.

2.2.1 The role of nanostructure materials in supercapacitors

There are few key parameters of supercapacitos that are greatly dependent on the type of electrode materials and the intimate contact between the electrode material, current collector and electrolyte as shown in Figure 2.6. High specific capacitance/capacity and wide operating voltage can provide high energy density of supercapacitors. Conversely, low ESR and optimum operating voltage can create high power density of supercapacitors. Electrode materials that have high specific surface area and porosity provide abundance active sites to facilitate the electrolyte ion diffusion and enhance redox reactions (and thus increase energy density of the device). While electrode materials with high electrical conductivity can augment the charge mobility and increase the rate capability (and thus elevate power density) of the device.

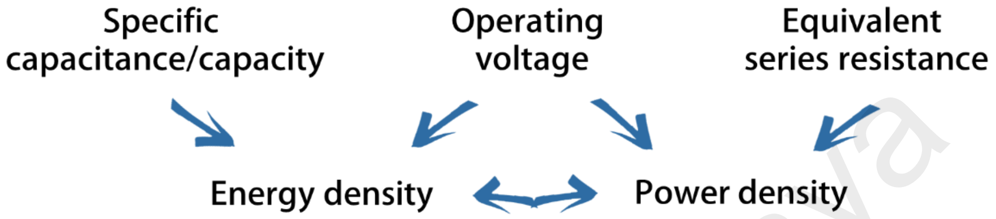

Figure 2.6: Key parameters for supercapacitors.

The motivation for the synthesis of nanomaterials comes from the fact that their physico-chemical properties are strongly influenced by size, composition, structure and surface functionality. Hence, the control over these variables can lead to the design of nanomaterials with desired performance for supercapacitor. The main properties of nanomaterials can be summarized into surface, electrical, and mechanical properties.

2.2.1.1 Surface properties

In supercapacitor, large surface area of material is the key point that can lead to high specific capacitance. Surfaces permit adsorption/diffusion of electrolyte ions through an interface and allow the occurrence of redox activity. Accordingly, one of the approaches to meet these requirements is by developing nano-sized or nanostructured electrode materials. Nanomaterials can give several advantages in supercapacitor compared with bulk materials such as;

(i) The diffusion rate of electrolyte ions and the mobility of electron can be remarkably increased due to the short transport distance within the particles.

(ii) Having immense electroactive surface area for the interaction with electrolyte ions, therefore high number of ions absorption (for capacitive electrode) and redox activity (for faradaic electrode) can occur.

(iii) High contact area between electrode material and current collector can be built so that the leaching of electrode material is minimal. This can reduce the rapid declining capacity especially during extensive charging-discharging.

Another approach to enhance the surface area is by preparing porous structure of material so that more electrode material-electrolyte interaction can happen. As illustrated in Figure 2.7, AC has different sized of channels or interconnected porous networks which enables large amount of charge storage if suitable electrolyte is used.

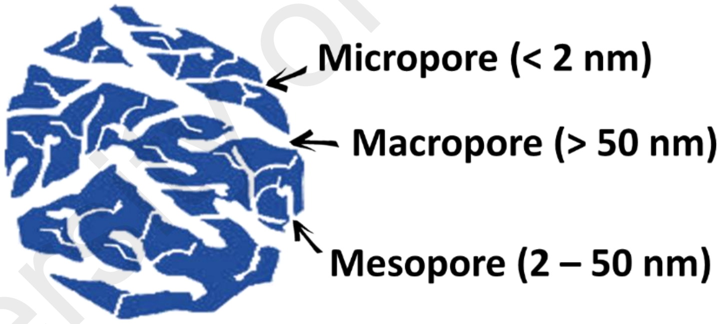

Figure 2.7: The illustration shows the vast amount of surface area of AC.

2.2.1.2 Electrical properties

The specific capacitance/capacity and rate capability are strongly rely on the electrical conductivity of electrode material. The electrical conductivity is size dependent which can be tuned by tailoring the structure of material. Based on traditional concept of nanosize effect, reducing the particle size down to nanoscale can enhance the electrochemical performance of the electrode. This concept is acceptable due to the fact that nanomaterial offers enormous surface area and can shorten the ion diffusion length than the bulk one (Wang et al., 2015). However, it should be pointed out that the electrochemical performance can be affected by the low electrical conductivity of an extremely small particle size of electrode material. When the particle size is smaller than certain values, the electronic band gap is increases depending on the type of materials. This concept is most pronounced for semiconductors, where those values can be in the range from several nm to 10 nm, which is known as the Bohr radius. Thus, if the size of the semiconductor particle is smaller than its Bohr radius, the movement of the electron is confined within the semiconductor crystal. This confinement effect causes the electronic band structure become quantized and as consequence, widen the band gap (Chen et al., 2012).

Inorganic materials (e.g. metal oxides, metal phosphates, metal sulphide etc.) which suffer from low electronic conductivity always face the issue of poor rate capability. Thus, recently these materials have been explored for composition with conducting materials such as graphene, CNT and conducting polymer so that not only the electrical conductivity can be improved, but also the synergistic effect arises from the chemical interaction between the individual elements can be gained.

2.2.1.3 Mechanical properties

High mechanical stability of electrode is important as this factor defines the cyclability of supercapacitor. Mechanical properties of nanomaterials deals with the porosity, grain size and nanoparticle-filled polymers. As mentioned in Section 2.2.1.1, although porous structure of nanomaterial can enhance the charge storage, they may not be able to retain their mechanical stability for prolong cycle life. This can be circumvented by creating composite via supporting the porous materials with electrically conducting materials such as CNT, graphene or conducting polymer (Canobre et al., 2015; Liu et al., 2016). However, the mechanical properties of composite materials depend mainly on the type, shape and agglomeration of nanoparticles as well as the approach taken to embed the nanoparticle into the supporting material. Therefore, the proper synthesis condition is crucial as the advantageous properties of nanoparticles may be lost if the composition forms aggregates, imitating the large particles.

However, the main challenge in synthesizing nanomaterials is the formation of agglomeration. Electrode materials that have high agglomeration can affect the high-performance of supercapacitors through the reduction in interfacial reaction between the electrode material and electrolyte. A large surface to volume ratio indicates that nanomaterials have high-surface energies which makes them thermodynamically unstable. Nanoparticle agglomeration can be avoided if their large surface energeis can be controlled.

2.2.2 Categorization of solids - crystalline, polycrystalline and amorphous

The choice of material structure is important as it can greatly influence the energy storage and rate capability in a supercapacitor. Based on the degree of atomic arrangement, solid can be categorized into crystalline, polycrystalline and amorphous structure (Figure 2.8). Briefly, if the constituent particles (atoms, molecules or ions) of a solid are ordered in regular arrangement or by a repetition of a certain pattern unit, the solid is said to be a crystal. Whereas for amorphous solid, the atoms are not in periodic arrangement. They are randomly arranged, forming a loosely packed structure. While for polycrystalline solid, it composed of more than one small crystals, and the periodicity of the atoms in the solid is interrupted by grain boundaries. Grain boundaries are the defects in the crystalline solid which tend to affect the electrical and thermal conductivity of the solid. The basic knowledge about the arrangement of the atoms in a particle is important as it contributes to the variation of the thermodynamic properties such as melting point, vapour pressure or solubility of the crystalline and amorphous materials. The distinct properties between crystalline and amorphous structure of materials is further explained below;

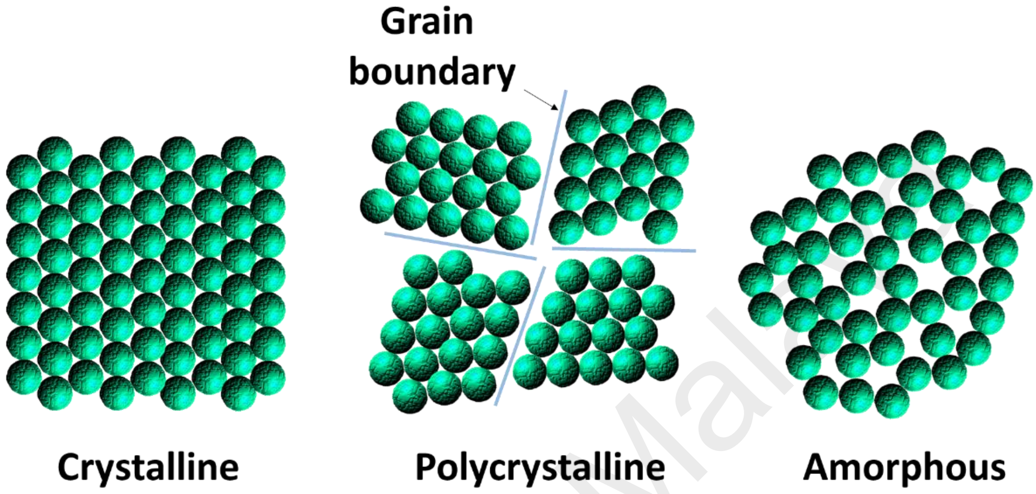

Figure 2.8: Crystalline, polycrystalline and amorphous structure.

2.2.2.1 Crystalline solid

Crystalline solid has specific long order range and because of this, crystalline solid has sharp melting point. In other words, crystalline solid has a well-order of atoms that repeats over long distances and can melt at a small range of temperature. The sharp melting point of crystalline solid can be related with the regularity of the crystalline lattice which creates the same local environment. This causes a uniform strength of bond between the atoms and this uniformity requires the same amount of thermal energy to break the interaction among the atoms (Reddy et al., 2016).

However, not all crystal solid have perfect repeating pattern of atoms or cells with no distortion. In fact, most crystalline solid have interrupted crystal pattern which is caused by a variety of crystallographic defects. Type of defects that can be found in crystal solid are vacancy defects (lacking of atom from the lattice sites), interstitial defects (a foreign atom is located in the crystal structure which is usually unoccupied), and dislocations (atoms are out of position in the crystal structure due to the applied stress to the material). Crystalline solid have various structures that lead to various facets that intersect at different angles. Crystal solid also have different form of facets which is caused by the variation of surface energy. Surface energy to understand the surface structure, surface orientation, reconstruction, roughening and the crystal equilibrium shape (Tran et al., 2016). Among the characterization techniques, X-ray diffraction (XRD) and transmission electron microscopy (TEM) is the most aythentic technique for analysing the molecular structure or degree of crystallinity of materials. If crystalline solid is radiated with X-ray (for XRD) and electron beam (for TEM), each structure able to generate a distinctive pattern that can be analysed to identify the group and compound strcucture of the material. A crystal structure can be identified by its unit cells, which are stacked in three-dimensional space (Huang et al., 2015).

2.2.2.2 Amorphous solid

In contrast, amorphous solids have continuous random network structure of atoms. The solid has shorter order range at the atomic length scale (the atoms are ordered over shorter distance) due to the nature of chemical bonding and has no definite melting point. The consequence of this, the local environment throughout the solid is varied contributed from the irregularity arrangement and distance between the atoms. Thus, it requires different degree of thermal energy to break the various strength of bonds formed between the atoms. As a result, amorphous solid tend to soften gradually over a wide temperature range.

As apposed to crystalline solid where different types of defects can be recognized, amorphous solid can only have one type of defect; coordination defects. This refers to the different coordination of atoms as compared to the atoms of similar type in the structure. Because of In addition, if the amorphous solid is radiated with X-ray or electron beam, the incident ray will be diffracted irregularly and defined peak in XRD diffractogram as well as lattice fringe in TEM image could not be observed. Interestingly, if an amorphous solid is retained at a temperature lower its melting point for prolong time, the atoms have potential to rearrange themselves into crystalline form (Stachurski, 2011).

2.2.3 Influence of crystal structure in supercapacitors

The choice of structure of electrode material, either crystalline or amorphous, greatly influences to the charge storage capability in energy storages. Typically, crystalline materials have been widely chosen due to the ordered structure of the crystalline materials that is believed can provide ample space for electrolyte ions accessibility during charging. The ample space provided by crystalline materials are dependent on the available symmetrical equivalent sites for ion transportation, crystal growth orientation, structural stability, electrochemical active facets and the presence of crystal defects (Liu et al., 2016). Nonetheless, the deployment of crystalline materials can be challenging especially when hosting large electrolyte ions such as Na^+ or K^+. The incapability of electrolyte ion to diffuse easily throughout the bulk electrode materials renders to the low the storage capacities. Recently, amorphous materials have been realized can store high energy as the ionic conductivity of the amorphous material is higher than crystalline materials. This is due to their loosely crystal structure which contributes to a greater volume of free space to accommodate a higher number of different size of ions and also can reduce the migrating distance of the ions. However, the electrical conductivity of the amorphous materials might be lower than that of crystalline materials due to distortion in periodicity.

The properties of carbon-based and transition metal oxide/hydroxide-based materials have been vastly explored to be employed as supercapacitor electrodes. However recently, considerable attention is being switched into metal phosphates due to their high performance in batteries. In this work, phosphate based materials have been chosen as a platform to study the effect of structure i.e. amorphocity/crystallinity on supercapacitor applications by tuning their morphologies and compositions. The characteristics of metal phosphate are presented in Section 2.3.

2.3 Phosphate-based electrode material

2.3.1 Phosphate classification

By general definition, phosphate (PO_4^{3-}) is a salt of monophosphoric acid and is a compound that built up from phosphorus atoms surrounded by a tetrahedron of four oxygen atoms. Elementarily, phosphate can be classified into three categories based on the oxygen to phosphorous ratio;

(i) O/P = 4 – orthophosphate or monophosphate

Monophosphate is categorized by a simple isolated PO_4^{3-} group

(ii) O/P > 4 – oxyphosphate

In atomic arrangement of oxyphosphate, some oxygen atoms are not belonging to the anionic entity. In other words, it is a combination of oxide (or hydroxide) and phosphate.

(iii) 5/2 < O/P < 4 – condensed phosphate

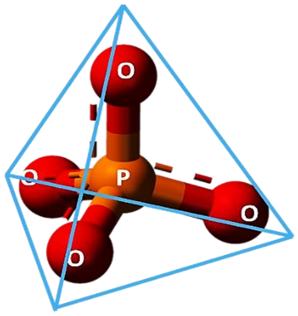

Figure 2.9: Molecular structure of phosphate.

Condensed phosphate corresponds to various anionic entities built from corner-sharing PO_4 tetrahedra (Figure 2.9). The condensed phosphate can be subdivided into three classes (Durif, 1995);

a) Linear polyphosphates − PO_4 tetrahedron shares one or two corners with other PO_4 tetrahedron with general formula of $(P_nO3_{n+1})^{(n+2)-}$. E.g. pyrophosphate with n = 2, $(P_2O_7)^{4-}$

b) Cyclophosphates −constructed by a ring of corner-sharing of tetrahedron PO_4 with general formula of $(P_nO_{3n})^{n-}$. E.g. metaphosphate (infinite chain) $(PO_3)^-$ (Durif, 2005)

c) Ultraphosphate − PO_4 tetrahedra shares its three oxygen atoms with the neighboring PO_4 groups with general formula of $(P_{2m+n}O_{5m+3n})^{n-}$. E.g. samarium pentaphosphate crystal (SmP_5O_{14}).

2.3.2 Metal phosphate advantages and limitations in energy storage

In the past few decades, numerous efforts have been made to develop nanomaterials in order to shorten the diffusion length and/or enhance the effective surface area for high performance energy storage devices. Transition metal oxides have been realized as the excellent electrode materials for most of the technological achievements. However, besides those metal oxides, 3D frameworks constructed from strong covalent bonding between transition metals and polyanions have aroused great interest since the discovery of the electrochemically active $LiFePO_4$ (Padhi et al., 1997). The researchers clarified that the presence of metal ions merge to a variety of metal phosphate structure provides different novel properties for different applications.

Metal phosphates have shown remarkable performance in batteries (Rajammal et al., 2017a), as catalysts (Aaddane et al., 2001), pigments (Meseguer et al., 2007), active substances for corrosion protecting materials (Deyab et al., 2016) etc. Recently, they have been paid great interest to be employed as supercapacitor electrode due to its low-cost, high redox properties, good thermal stability and environmental inertness (Maybodi et al., 2011; Zhao et al., 2015). The phosphate group in general exists with tetrahedral structural unit $(XO_4)^{n-}$ which offers several advantages for energy storage as listed below (Fang et al., 2017);

(i) The three dimensional framework of phosphate contain many roomy interstices that can reduce the volumetric expansion during electrolyte ions diffusion, which is favourable for the structural stability.

(ii) Due to the formation of M–O–P bonds, the electrochemical potential (and hence energy density) can be magnified through the inductive effect of strong P–O bond. The electron density moves away from the M centre and subsequently increase the ionic character of M–O bonds and results in a high electrochemical potential of metal phosphate.

(iii) The strong P–O covalent bonds can prevent the unstabilization of the lattice oxygen.

(iv) The low thermal expansion (around 10^{-6} °C^{-1}) possessed by phosphate framework can guarantee its high structural stability at high temperature, thereby it is safe for extensive usage.

However, PO_4^{3-} groups have low electron conductivity due to their large size and intrinsic isolating nature.

2.3.2.1 Nickel phosphate

Nickel-based materials (e.g. nickel oxide (NiO), nickel sulphide (Ni_3S_2) and nickel hydroxide ($Ni(OH_2)$)) have shown significant role in supercapacitors and have garnered tremendous attention until now mainly due to its common excellent properties; high theoretical specific capacitance, good chemical and thermal stability, have rich redox catalytic property as well as cheap. For example, Xiao et al. reported large scale ultrathin nickel oxide (NiO) nanoflakes grown on nickel foam using hydrothermal method combined with subsequent calcination. The material exhibited high areal capacitance of 870 mF/cm^2 at 1 mA/cm^2 at 3 M KOH (Xiao et al., 2016). Li et al. have demonstrated the preparation of nanoporous nickel sulphide (Ni_3S_2) films on nickel foam which can control pore size by solvothermal-assisted sulfuration. Due to its porous structure, Ni_3S_2 achieved higher specific capacitance of 3.42 F/cm^2 at 1 mA/cm^2 at 1 M KOH (Li et al., 2017). Mao et al. fabricated ultrafine β-$Ni(OH)_2$ nanosheets using hydrothermal treatment. The synthesized material was fabricated on multilayer nickel foam and delivered high specific capacity of 609.2 C/g at 1 A/g in 6 M KOH (Mao et al., 2016).

Inspired from the reported studies, this work has chosen nickel ion to be combined with phosphate polyanion to form nickel phosphate ($Ni_3(PO_4)_2$). $Ni_3(PO_4)_2$ materials have been prepared via various methods such as hydrothermal (Zhao et al., 2015), wet chemical process (Hashimoto et al., 1994), microwave (Maybodi et al., 2011), sol-gel (Rajammal et al., 2017b) and solvothermal (Raju & Ozoemena, 2015). These different synthesis methods led to a diverse structural, morphological, chemical composition and properties which are the reasons for the versatility of $Ni_3(PO_4)_2$. $Ni_3(PO_4)_2$ has largely been employed as catalysts mainly due to their redox properties. Yang et al. explored the electro-oxidation of methanol on mesoporous $Ni_3(PO_4)_2$. Mesoporous $Ni_3(PO_4)_2$ was prepared via sol-gel method and the sample was fabricated on glassy carbon electrode for electro-oxidation of methanol. They found out that the redox transition between Ni^{2+}/Ni^{3+} increases with increasing methanol concentration which indicates the high sensitivity of $Ni_3(PO_4)_2$ towards the determination of methanol (Yang et al., 2012). This is supported by Chong et al. for photoelectrochemical (PEC) glycerol-based fuel cell. They observed the enhancement in photocurrent response towards glycerol oxidation and reduction in charge transfer resistance by phosphate modified hematite (Pi-Fe_2O_3) after loaded with $Ni_3(PO_4)_2$ (Chong et al., 2017).

Besides catalyst, $Ni_3(PO_4)_2$ have been widely employed in lithium-ion battery applications in which the materials are modified with lithium insertion compounds to form olivine metal phosphate. For instance, Minakshi et al. demonstrated the lithium intercalation/de-intercalation process in olivine structure of lithium nickel phosphate ($LiNiPO_4$). The experiment showed that $LiNiPO_4$ is electrochemically active during intercalation/de-intercalation of lithium ions process accompanied with a Ni^{3+}/Ni^{2+} redox reaction. $Ni_3P(O_4)_2$ also has been used as the electrode coating material in battery (Minakshi et al., 2011). Lee et al. coated $LiNi_{0.8}Co_{0.15}A_{l0.05}O_2$ cathode material with $Ni_3(PO_4)_2$ to improve the performance of battery. The $Ni_3(PO_4)_2$-coated $LiNi_{0.8}Co_{0.15}A_{l0.05}O_2$ exhibited increased lithium intercalation stability and rate capability by shielding $LiNi_{0.8}Co_{0.15}A_{l0.05}O_2$ from hydrofluoric acid attack in the electrolyte, thus suppressed the charge transfer resistance (Lee et al., 2011). Although $Ni_3(PO_4)_2$ offer undeniable advantages, there are several issues that need to be addressed. $Ni_3(PO_4)_2$ generally have wide band gap which can alleviate the electronic conductivity. This can affect the rate capability of supercapacitor and can diminish its cycling stability. Hence, synthesizing $Ni_3(PO_4)_2$ with highly conducting matrix is an effective approach to boost its electrical conductivity .

2.3.2.1 Silver phosphate

Numerous studies have reported that the properties of nanomaterials can be boosted by creating composite. In this work, silver phosphate (Ag_3PO_4) has been introduced to $Ni_3(PO_4)_2$ to form $Ni_3(PO_4)_2$-Ag_3PO_4 nanocomposite. For comparison with other metals such as gold, platinum and palladium, Ag is relatively cheaper and non-toxic which make it highly desired as the composite materials. Ag_3PO_4 has been widely applied as an antibacterial agent in the pharmaceutical field. It also has been reported to be an outstanding candidate for water photooxidation mainly due to its high positive valence band position, low-toxicity and excellent photocalaytic ability. From Tauc calculation, Ag_3PO_4 exhibits a low indirect and direct bandgap of 2.36 eV and 2.43 eV, respectively.

Ag_3PO_4 also have other good properties that are beneficial for supercapacitors such as high electrical capacity, good reversibility and large effective surface area. Li and co-workers reported the novel 3D Ag_3PO_4 tetrapods that were synthesized by hydrothermal method. Ag_3PO_4 tetrapods exhibited good electrochemical performance with the maximum specific capacitance of 160 F/g (which is attributed to its high conductivity and the 3D microstructure (Li et al., 2014). Recently, Zheng synthesized Ag_3PO_4 nanospheres via a sonochemical process. The specific capacitance achieved was 832 F/g, which is considerably excellent for supercapacitor. However, Ag_3PO_4 nanospheres exhibited an inferior cycling stability which could be due to the formation of Ag_2O during the cycling process (Zheng et al., 2017).

2.4 The electrochemical behaviour of other common faradaic electode material

2.4.1 Metal oxides/metal hydroxide

Metal oxides are the metallic compound with oxygen in the form of oxide ion (O^{2-}). They have been widely reported for pseudocapacitor electrodes due to the existence of various oxidation states for quick surface redox reaction. RuO_2 is the earliest studied metal oxide for pseudocapacitor and it gives the best pseudocapacitive performance among other metal oxides. Nevertheless, because of the factor of high cost and scarce source of RuO_2, researchers shift their attention to the cheaper metal oxide such as MnO_2.

Like RuO_2, the charge storage of MnO_2 mostly comes from pseudocapacitance with high theoretical specific capacitance of ~1370 F/g. However, such high specific capacitance is not frequently obtained due to its poor electrical conductivity. Generally, MnO_2 have five different crystal structures; i. e. α-, β-, λ-, δ- and γ- correspond to different size of tunnels. For example, λ-MnO_2 has 3D tunnel structure whereas β- and γ-MnO_2 have 1D tunnel structure. These tunnels can determine their electrochemical performance as they allow the intercalation of electrolyte cation. In alkaline electrolyte, $NiO/Ni(OH)_2$ also exhibit high specific capacitance at low current densities but their working potential window are small (about 0 - 0.5 V). Besides NiO, Co_3O_4 is another metal oxide that exhibit high specific capacitance. Unfortunately, it has large volume change during repeated charge-discharge, resulting in poor cyclic stability, but its stability is better than NiO (Lu et al., 2013).

2.4.2 Binary metal oxide compound with spinel structure

Mixed metal oxides or binary metal oxide with formula AB_2O_4 ($A^{2+}B_2^{3+}O_4^{2-}$) is belonging to spinel structure which is believed can improve the properties and performance of monometallic oxides. This compound has a robust crystalline architecture in which A (represents a divalent cation) and B (represents trivalent cation) are occupying the tetrahedral and octahedral sites in a cubic close-packed lattice. Thus, this unique structure is beneficial for supercapacitor as it offers three dimensional diffusion pathways. The charge storage of spinel compound involves the reversible transformation from AB_2O_4 to A and B oxyhydroxide. If A or B is Co, the formed Co oxyhydroxide during the first redox reaction will undergo a second redox reaction. The participation of second redox reaction permits richer redox reaction and could exhibit higher specific capacity than monometallic oxides. The equations of redox process of $NiCo_2O_4$ are expressed as below;

$$ZnCo_2O_4 + OH^- + H_2O \leftrightarrow ZnOOH + 2CoOOH + e^- \quad (2.5)$$

$$CoOOH + OH^- \leftrightarrow CoO_2 + H_2O + e^- \quad (2.6)$$

2.5 Conducting polymers

Conducting polymers (CPs) are organic materials that consist of a high π-orbital system, through which electrons delocalize around the entire polymer chain. For traditional polymers such as polyacethylene, they are electronically insulating due to the valence electrons that are bound in sp3 hybridized covalent bond. However, for CPs, they are governed by sp2 hybridized carbon centers. In general, pristine CPs comprise conjugated single and double bonds. A single bond has strong localized σ bond whereas a double bond has both σ and weaker π bonds. This conjugated system differs the electrical, physical, optical and electrochemical properties of CPs (Figure 2.10). CPs offer several advantages such as low density, chemically and mechanically stable, flexible, and can exist in a variety morphologies. These advantages make them highly demanded for wide range of applications including electronic devices, actuators, photovoltaic cells etc.

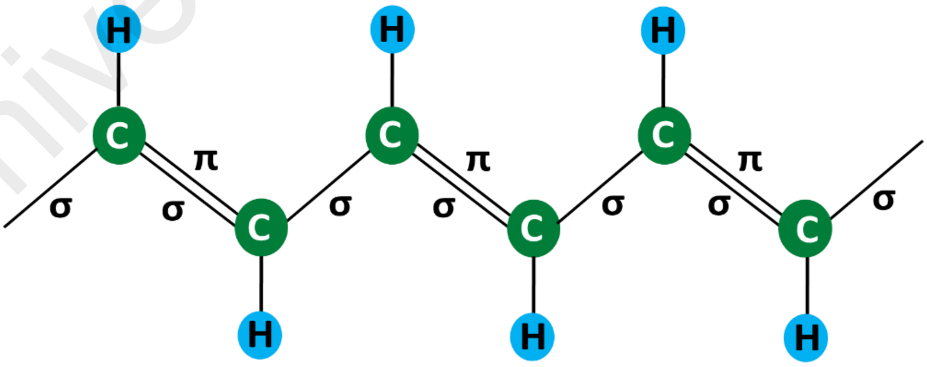

Figure 2.10: Chemical structure of conducting polymers.

2.5.1 Doping process in CPs

Pristine or un-doped polymers can turn into highly conducting state, called intrinsic conducting polymers (ICPs) upon doping. Generally, doping is a process where electron is removed from the outer space of the atom (oxidation reaction), or electron is added to the atom (reduction reaction) and subsequently force the atom to create another orbital. The purpose of the doping process is to modulate the electrical conductivity of material by generating delocalized charge carrier. The study on ICPs was initiated by Shirakawa who observed the formation of silvery films of polyacetylene after mistakenly mixed the chemical compound of polyacetylene. Shirakawa was then collaborated with Heeger nd MacDiarmid on further development of polyacetylene. After went through several processes, they discovered that the conductivity of polyacetylene was significantly increased by 10 million-fold when polyacetylene is oxidized using iodine vapour (Shirakawa et al., 1977).

Oxidation occurs when the electrons are excited from the highest occupied molecular orbital (HOMO) of the valence band while reduction happens when the electrons are transferred to the lowest unoccupied molecular orbital (LUMO) of conduction band. CPs can be doped via n-type doping (insertion of electron) or p-doping (removal of electron), generating delocalized charge carriers in the form of polarons, bipolarons or solitons. As the doping level increases, more charge carriers are generated until their energy bands overlap, forming intermediate band structures. These band structure facilitates electron along the polymer chains and results in the augmentation of electrical conductivity of CPs (Figure 2.11).

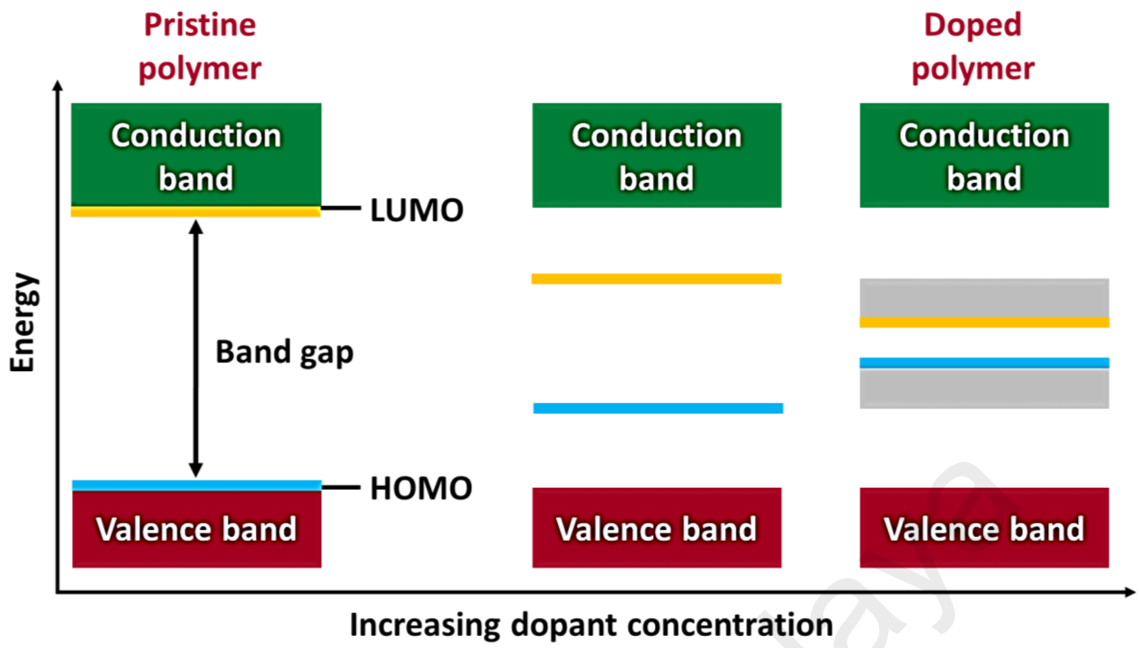

Figure 2.11: Band diagrams of doped polymer showing the formation of charge carrier and intermediate band structure.

The electrical conductivity of the ICPs is varies in the range of 10^{-3} - 10^{3} S/cm, depending on the pH or concentration of incorporated dopant ions. CPs can be classified into degenerates system (possess two identical geometric structures) and non-degenerate system (possess two different structure with different energies) after exchanging the double bond and single bond at the ground state. Polarons and bipolarons exist in both degenerate and non-degenerated system (eg. PPy and PT) whereas solitons formed in degenerate system (e.g. PA).

Other than conductivity, the surface roughness, wettability, bulk structural properties and density of CPs depend on the nature and concentration of dopant as well as doping duration. In regard to the molecular size, dopants can be categorized into small cations/anions (e.g. Cl^{-} and Na^{+}) and large polymeric species (e.g. sodium polystyrenesulfonate and polyvinyl sulfonate). Small dopants can be readily exchanged with other ions that present in the surrounding environment and large dopants can be strongly bound to the polymers. Some of the ICPs shown in Figure 2.12 emerged to the forefront of the various applications such as wires, electromagnetic shielding and electrostatic dissipation.

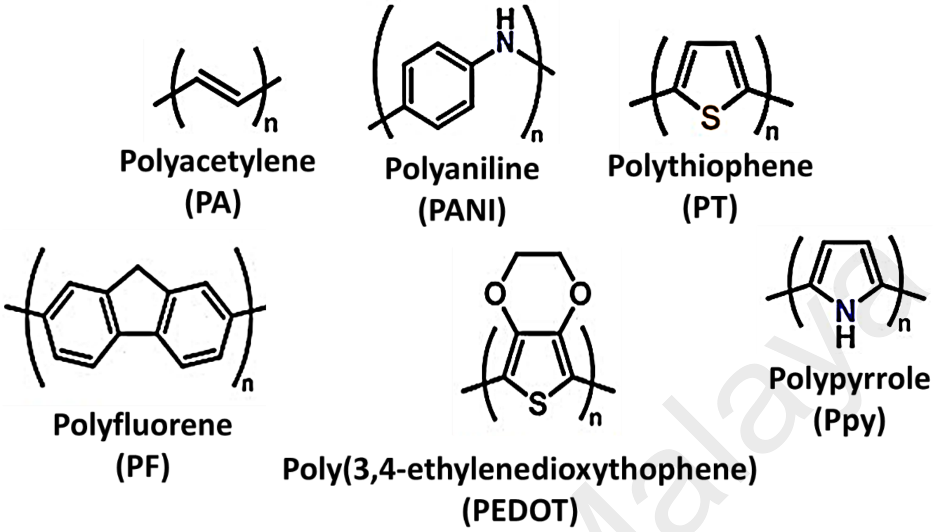

Figure 2.12: Different types of conducting polymers.

2.5.2 Polyaniline

Among the CPs, polyaniline (PANI) (historically called aniline black) is the most investigated mainly because of its low-cost production, thermal stability and unique redox chemistry. PANI can be synthesized nomer or starting material that is manufactured from benzene. PANI consists of a repeating chemical structure by the formula shown in Figure 2.13 where n is molar fractions of peither through chemical or electrochemical oxidation of aniline. Aniline is the inexpensive mohynylenediamine structural unit and m is molar fractions of quinonediimine structural unit.

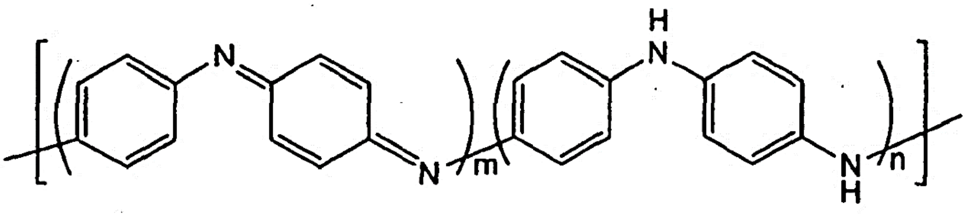

Figure 2.13: Repeated chemical structure of PANI.

2.5.2.1 Oxidation states of PANI

Considering Ppy and PT, they only have two oxidation states. In comparison, PANI has three interchangeable oxidation states known as leucoemeraldine base (LB), emeraldine base (EB) and pernigraniline base (PB). The difference between these oxidation states is determined by the concentration of quinoid and benzoid units in PANI. LB is fully reduced form appeared in pale yellow colour/colourless while PB is fully oxidized with violet in colour. Both of LB and PB are non-stable and insulating in nature even after doped with acid, except for blue colour of EB. EB can be switched into the most stable and electrically conductive state called emeraldine salt (ES) if it is protonated (doped). ES can be reduced back to LB associated with the decrease in conductivity if treated by alkaline (Stejskal et al., 2010). Usually, PANI which is fabricated into electrode has all the three oxidation states, however, only protonated EB can gives the best capacitive performance. The mechanism of transition between different oxidation states of PANI and their molecular structure is displayed in Figure 2.14.

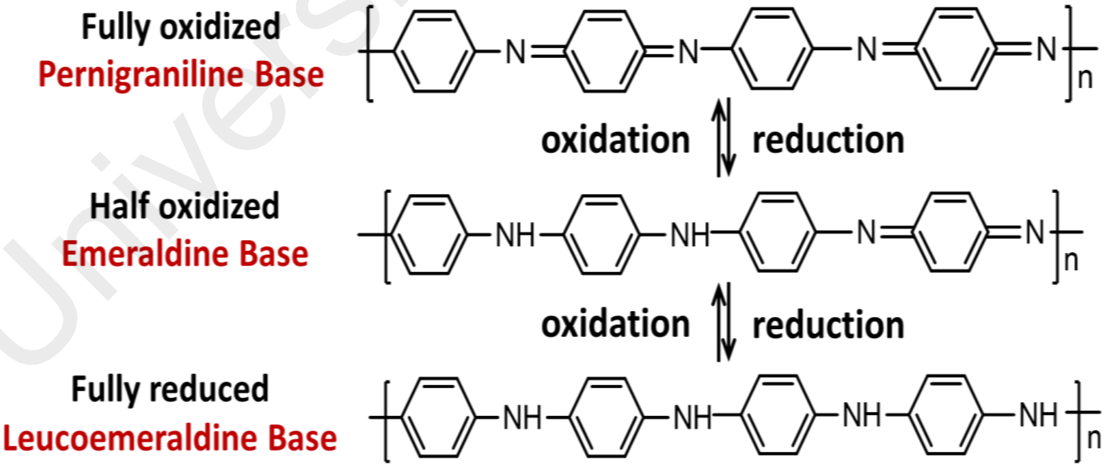

Figure 2.14: The transition between different oxidation states of PANI.

2.5.2.2 Production of PANI

Synthesis of PANI is economical as complicated instrument is require. PANI can only be synthesized in the low pH or acidic media, otherwise, the synthesized PANI consists of low chain oligomeric material. It is commonly synthesized either through chemically or electrochemically oxidative polymerization of aniline. These two routes involve simultaneous occurrence of polymerization and doping process. Chemical polymerization is chosen if large quantity of PANI is needed. On the other hand, electrochemical polymerization is useful if PANI film electrode is requested.

(i) Chemical synthesis

Chemical polymerization requires aniline, an acidic medium and an oxidizing agent. The common acids that have been used are hydrochloric acid (HCl) and sulphuric acid (H_2SO_4). While for oxidant, ammonium persulfate (APS) is the mostly used, with the function of withdrawing proton from an aniline molecule. Other examples are potassium dichromate ($K_2Cr_2O_7$), cerium sulfate ($Ce(SO_4)_2$), potassium iodate (KIO_3) and hydrogen peroxide (H_2O_2). It has been reported that in order to obtain high conductivity and high yield of PANI, the recommended oxidant/aniline molar ratio used should be ≤ 1.15 with the environment temperature between 0 to 5°C. The advantages of using this route are large quantity of PANI can be produced and additional tools such as electrode and power supply is not required.

(ii) Electrochemical synthesis

PANI obtained by electrochemical polymerization is typically adhered on the substrate using acidic aqueous electrolyte. By proper design of experiment condition, the thickness, structure, morphology and conductivity of PANI can be controlled. A three-electrode setup is needed; a working electrode (on which the polymer is coated), a reference electrode and a counter electrode. Three different electrochemical techniques can be used; (i) galvanostatic with a constant applied current, (ii) potentiostatic with a constant potential, and (iii) potentiodynamic with current and potential varies with time. The coated PANI can be separated from the substrate by immersion in an acidic solution. The advantage offered by this route over chemical oxidation is thin PANI film can be obtained directly on the electrode surface without require any binder which can reduce the conductivity. Moreover, the various thickness of PANI can be obtained by monitoring the electrochemical parameter. However, this route forms lower yields of PANI.

2.5.2.3 Polyaniline doping

As mentioned in Section 2.5.2.1, PANI has three different oxidation states; LB, PB and EB. PANI become electrically coducting either by the oxidation of LB or by protonation of EB. A small amount of oxidant able to significantly tune the electronic, optical, magnetic and structural properties of PANI. The imine nitrogen atoms in PANI can be partially or fully protonated producing ES, depending on the pH of aqueous dopant acid. The process of EB doping treated with aqueous acid is given in Figure 2.15.

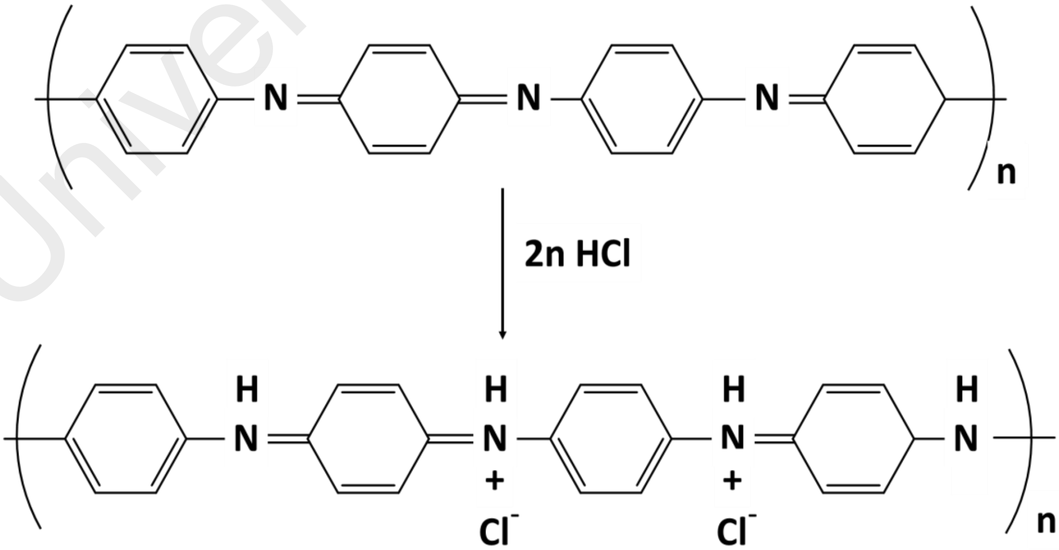

Figure 2.15: Mechanism of PANI doping.

The conductivity of the doped PANI can be increased up to 10 orders of magnitude as compared with the undoped PANI. If the EB is fully doped (i.e. 100 % protonation of imine nitrogen atoms), PANI should formed bipolaron and become diamagnetic in nature.

2.5.3 Factors that control the electrochemical behaviour of PANI as supercapacitor electrode

Utilization of PANI as supercapacitor electrodes was first studied by Kaner and his co-workers. The highest specific capacitance that has been achieved by PANI is 950 F/g, surpassing other CPs that store charge on the surface. PANI has many desirable properties which are beneficial to be deployed in supercapacitors including high electro-activity, exist in different morphologies, flexible, tuneable electrical conductivity (range from 0.1 - 5 Scm^{-1}), easy to produce and is relatively cheap which is competitive with some considerably expensive metals. However, these properties is influenced by the electrochemical redox states, chemical backbone structures, synthesis method as well as pH and type of electrolyte, and all of these can be controlled by several factors;

2.5.3.1 Electrical conductivity

The electrical conductivity of PANI can be studied at CV analysis by deciphering the redox peak currents. During redox (or charging-discharging) process, electrolyte ions are inserted into (doping) and extracted from (de-doping) the PANI backbones. The doping and de-doping reaction is associated with the transition between conducting and insulating phases of PANI. PANI can store charge if it is in electrical conducting form, i.e. in the potential range where fully reduction of PANI is excluded (Peng et al., 2011) .

2.5.3.2 Surface area and morphology

Surface area and morphology of PANI are substantial to obtain fast doping and de-doping process. It has been reported that nanostructured PANI has higher specific capacitance than bulk PANI. This is due to the high surface area that allow high interaction with electrolyte ions. The morphology of PANI can be tuned via adding additive or control the polymerization temperature. Guan et al. found out that longer polymer chain of PANI (synthesized by adding para-phenylenediamine additive during aniline polymerization) enhanced the specific capacity as compared to the shorter chain of PANI (Guan et al., 2010). Kuang et al. prepared different morphologies of PANI (tubular, spherical and granule) by varying the polymerization temperatures (at 0 - 5°C and at room temperature). Tubular PANI decayed to only 75 % after 500 charge-discharge cycle which indicates it is more stable as compared to spherical (35 %) and granule (57 %) (Kuang et al., 2013).

2.5.3.3 Transition of redox states

Multiple redox states of PANI is favourable in supercapattery as it contributes to high specific capacity via providing wide total surface charge potential at CV. PANI typically exhibits two sets of redox peak over potential, signifying two sets of different redox activity. The first redox current peak is concomitant with the transition from leucoemeraldine to emeraldine, while the second redox current peak associated with the transition from emeraldine to pernigraniline. However, some PANI gives three set of redox current peaks due to the presence of the transition between p-benzoquinone and hydroquinone (Song & Choi, 2013).

2.5.4 PANI-based nanocomposites

Despite the good properties mentioned, bulk PANI has inferior stability. The specific capacity of PANI usually begin to decay under less than a thousand cycles due to the repeated intercalation and de-intercalation of ions. This repeated process (swelling, shrinking and cracking) changes the physical structure of PANI and eventually renders to severe mechanical failure of the electrode after prolonged use. Moreover, PANI can be over-oxidized and decomposed at high potentials, affecting its cyclic stability as well as its stable potential window.

Fortunately, PANI can be composited with other materials easily for achieving refined physico-chemical properties as it has high flexibility property. In this aspect, various materials have been mixed with PANI to form PANI-based nanocomposites such as carbonaceous materials, metals, metal oxides, etc. Carbonaceous materials such as graphene and CNT offer functional groups that can induce chemical interaction with PANI chains. As reported by He et al., carboxyl groups of CNT enhances the specific capacity of PANI-CNT composite by 60 % (He et al., 2016). While metals oxides have different oxidation states that can boost redox activity of PANI, contributing to high pseudocapacitance. Interestingly, metal oxide also can act as an oxidizing agent for commencing the polymerization of PANI while at the same time the conducting nature of PANI can elevate the low intrinsic conductivity of metal oxides.

2.6 Synthesis methods

The crystal structure, surface energy, morphology etc. of nanomaterials is highly influenced by the synthesis routes. Various synthesis methods have been used to prepare nanoparticles and their nanocomposites including hydrothermal, co-precipitation, sol-gel, etc. However, this thesis will only focus on the sonochemical, calcination (as the post-heat treatment), hydrothermal and physical blending method.

2.6.1 Sonochemical

Sonication are the most recommended procedure to break down powder or disperse suspension of material into the liquid medium. This method usually being chosen due to its operation and maintenance simplicity, convenient and relatively cheap tool compared to other conventional methods. Ultrasonic waves are induced in a liquid medium either via direct (by immersing a horn into the liquid) or indirect sonication (place the sample container into the sonication bath). Direct sonication yields a higher ultrasound energy over indirect sonication for the purpose of efficiently dispersed solid suspension.

2.6.1.1 Principles of operation

The horn sonicator consists of three main components; generator, converter (transducer) and horn (probe) (Figure 2.16). The generator is used to converts the AC power to 20 kHz signal. The function is to enable the piezoelectric converter to drive a mechanical vibration towards the horn tip. The horn is a metal rod used to transmit the ultrasonic waves from the convertor into the liquid.

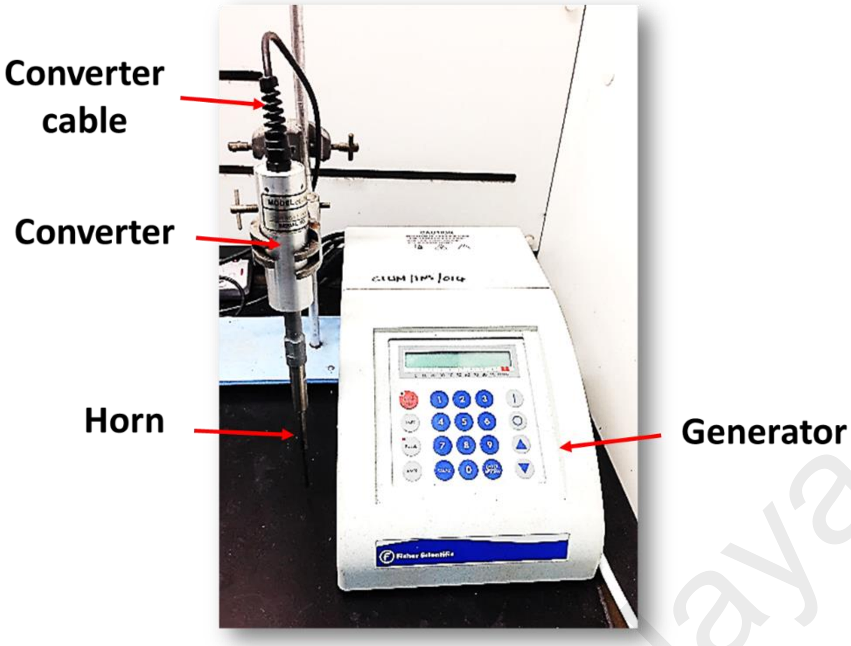

Figure 2.16: Photoimage of horn sonicator.

When the horn is immersed in a liquid medium, it will generate high intensity of ultrasonic wave (illustrated in Figure 2.17). The ultrasonic wave propagate through the liquid in alternating high pressure (compression) and low pressure (rarefaction) cycles. The ultrasonic wave induces acoustic cavitation in which vacuum cavitation (bubble) are created, grow and implosively collapse in the liquid. The acoustic cavitation happens due to the absorption of ultrasonic energy by the bubbles which causes the bubbles to oscillate and grow. The bubbles will grow until they reach their critical size (about 5 - 20 µm), then intensely collapse releasing the stored energy to the liquid. This collapsing bubbles generates a short-lived localized hot-spot that achieve extreme temperature and pressure of 5000 K and 1000 atmosphere, respectively, as well as heating and cooling rates exceed 1010 Ks^{-1}. The high temperature and pressure produced are responsible to the formation of nanoparticles (Xu et al., 2013).

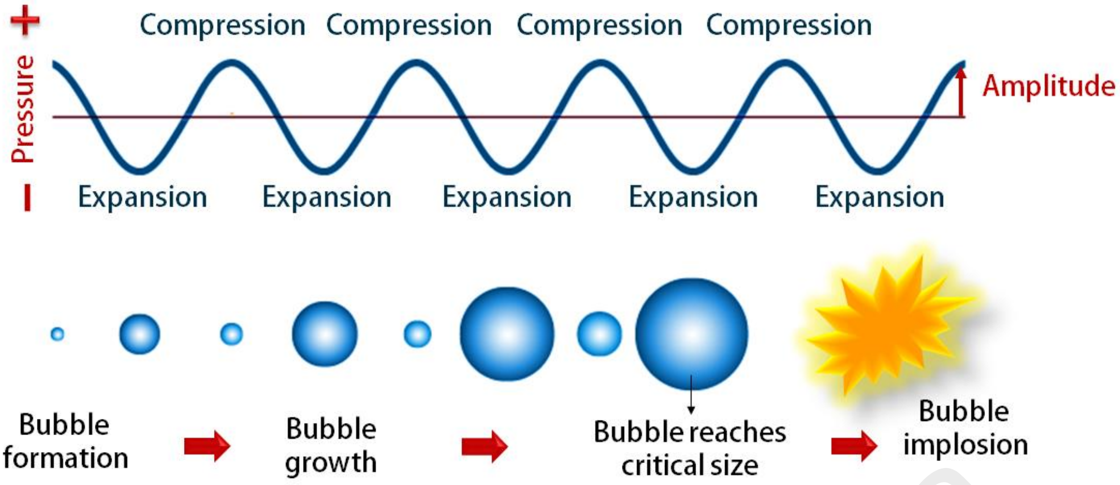

Figure 2.17: Acoustic cavitation process.

During material synthesis, there are several important parameter that need high consideration (Taurozzi et al., 2011);

i) Temperature

During sonication, the acoustic cavitation produce the local heating (25 - 90 °C) which will result in a hot/warm liquid bulk over time. As the temperature increases, the sonication reaction facilitates the nucleation process and enhance the rate of nanoparticle production. The excessive bulk heating may affect the volume of the treated liquid due to liquid evaporation or degrade the medium components.

ii) Sonication time

The total ultrasonic energy delivered to the liquid depends on the applied power and sonication time. Two sets of solution treated at the same power for different sonication duration results in different average particle size and dispersion states. For instance, for solution with the volume of 80 mL, short sonication time (10 - 30 min) able to break particles into primary particles. Whereas, prolong sonication time (more than 60 min) causes to the agglomeration and less uniformity of the nanoparticles. However, in some cases, longer sonication time is beneficial for dispersing high concentration of suspension (e.g. MWCNT in deionized water) and high volume of solution (Mahbubul et al., 2015).

iii) Sample concentration and volume

At constant volume of the solution, high concentration of the suspension increases the frequency of particles collision and subsequently enhance the particles breakage. Nonetheless, if the suspension is too concentrated, it will exert a greater resistance to the oscillating probe. This decreases the number of particles collision and lead to particle agglomeration and aggregation.

iv) Sonication horn and container geometry

The amount of acoustic energy delivered to the suspension is also depends on the shape of the horn taper and its immersion depth in the suspension. Horn taper can magnify the vibration amplitude to deliver high power. Microtip horn vibrate with higher amplitude than flat tip horn. However, microtip is less mechanically robust and its usage is limited to the applied power setting. Besides, different geometry of bottom flasks shows different acoustic energy distribution. The best approach is using small diameter of cylindrical shape container as it maximizes the contact between liquid and probe for the acoustic wave irradiation.

2.6.2.1 Calcination

Nanomaterial synthesis using sonochemical method typically involves subsequent calcination to complete the synthesis process (e.g. solvent, reducing agent, surfactant etc.). Calcination is a thermal treatment process at high temperature conducted in the absence or limited supply of air or oxygen. The purpose of this process is for thermal decomposition, phase transition or removal of a volatile fraction. Calcination is carried out in the muffle furnace (Figure 2.18) and usually takes place at temperature below the melting point of materials.

Figure 2.18: Muffle furnace.

In industrial application, calcination process is commonly used for the production of cement. Calcium carbonate (limestone) is decomposed to calcium oxide (lime) and carbon dioxide through heating process at around 850 °C for the production of cement. Other examples of using calcination are to decompose hydrated minerals (crystalline water/water vapour), decompose volatile substance that usually can be found in raw petroleum coke, to remove ammonium ions in the synthesis of zeolites and as a heat treatment to effect phase transformation. Calcination also has been reported can be used for metal oxidation when J. Rey discovered the weight of lead (Pb) and tin (Sn) increases after being calcinated, presumably because of the incorporation of air in the metal (Satapathy et al., 2014).

2.6.2 Hydrothermal

As a subset of solvothermal technique, hydrothermal has been of considerable interest for a diversity of materials and morphologies due to its simplicity, safe and environmental friendly. This technique utilizes high temperature-pressure condition to conduct chemical reactions by using stainless steel autoclave. In particular, this technique typically carried out under 300 °C for preparing various nanostructure materials, thin films and also growth of single crystals. Hydrothermal process have widely been employed to synthesize different kinds of nanosized semiconductor materials such as metal oxides and other metal compounds. Various sizes and morphologies (e.g. flower-like, nanorod, nanocubic etc.) can be obtained by tuning the experimental conditions such the pH of the solution, reaction temperature and heating duration. However, particle agglomeration is commonly happen without the addition of surfactant agent into the reaction medium (Djurisic et al., 2007).

2.6.3 Physical blending method

Physically blending method is one of the easiest approach to synthesize composite materials. This method has widely been used to prepare polymer blend by mechanically mixing different polymers. However, it is also possible to obtain good quality of polymer nanocomposites through direct mixing polymers with nanofillers if the uniform or pseudo-homogenous mixture is obtained (Thomas & Zaikov, 2008). This method can be done in two ways; melt compounding and solution mixing. Melt compounding approach is when polymers are mixed with nanofillers without the presence of any solvents above the glass transition temperature of polymer. While solution mixing in which polymers are mixed with nanofillers in solvent and the final product is obtained through solvent evaporation (Khan et al., 2017).

2.6.4. Applications

The major energy storage companies like Maxwell, Murata and Tecate Group have commercialized their batteries and supercapacitors (EDLCs) but still need another version of energy storage system than can bridge the advantages and disadvantages of those energy storage devices. Supercapatteries can be applied in various technologies including transportation, power grid, and consumer electronics as explained below;

(i) Regenerative braking system in transportation

Regenerating braking system is a technology that is employed in hybrid electric vehicles and also in fully electric vehicles. This technology helps to recharge the vehicle’s energy storage while also assisting with braking. Typically, in conventional automobiles with conventional brake system, the energy is required to slow down a vehicle through friction is converted to heat in the brakes and is wasted. This can cause to the tyre wear due to the friction between the tyre and the road. With regenerative braking, the kinetic energy is recoup and put to use by converting it to electricity and storing it in energy storage for future use. Supercapatteries’ ability to charge and discharge quickly enable them to efficiently capture the regenerative braking energy and provide instant power for acceleration, thus helping to reduce fuel consumption.

(ii) Grid and renewables

The integration of renewables such as solar and wind power into power grid is one strategy to reduce carbon footprint. However, the output power is unstable because of intermittent nature of those energy sources, which leads to increased costs for the utility and the ratepayer. Therefore, fast responding energy storage is need so that the power output becomes much reliable. Batteries can store high energy but they are not quick enough to respond and can only survive about 1000 repeated cycles of charge-discharge. Conversely, supercapacitors (EDLCs) can quickly store and release energy but they can’t store large amount of energy. The fast-responding and high energy supercapatteries have great potential to support the intermittency behaviour of solar and wind and help during emergencies like power outages, equipment failure or other unforeseen circumstances.

(iii) Consumer electronics

Lithium-ion batteries in laptops and mobile phones can last for hours even days but the slow process of converting chemical energy to electrical energy and vice versa is a slow process which require long time for the gadgets to be fully charged. EDLCs able to deliver performance that batteries currently can’t but unable to store enough energy to power the gadgets that last longer than few minutes. Supercapatteries, however, can be charged and discharged much faster than batteries at the same time able to store higher energy than EDLCs. Supercapatteries have lower internal resistance than that of batteries therefore they do not heat as much.

CHAPTER 3: MATERIALS AND METHODOLOGY

The first section of this chapter presents the chemicals and electrodes used during electrochemical studies. The second section demonstrates the methodologies for the synthesis of electrode material, electrode fabrication and supercapattery assembly. The third section mentions about the characterization techniques used to investigate the physical and electrochemical properties of synthesized samples.

3.1 Materials

Table 3.1: Chemicals used in this thesis.

Category		Chemical name	Source
Battery-type electrode	Synthesis of PANI (active material)	Aniline ($C_6H_5NH_2$)	Sigma-Aldrich, Malaysia
		Ammonium peroxydisulfate ($(NH_4)_2S_2O_8$)	Sigma-Aldrich, Malaysia
		Hydrochloric acid (HCl)	Sigma-Aldrich, Malaysia
	Synthesis of metal phosphate (active material)	Nickel(II) acetate tetrahydrate ($Ni(CH_3CO_2)_2{\cdot}2H_2O$)	Friendemann Schmidt, Malaysia
		Anhydrous disodium hydrogen phosphate (Na_2HPO_4)	Friendemann Schmidt, Malaysia
		Silver nitrate ($AgNO_3$)	Sigma-Aldrich, Malaysia
		Ammonia 28 % (NH_3) solution	Sigma-Aldrich, Malaysia
		Ethylene glycol ($C_2H_4O_6$)	Sigma-Aldrich, Malaysia

Table 3.1, continued.

Battery-type electrode	Synthesis of zinc cobaltite (active material)	Zinc acetate dihydrate, ($Zn(C_2H_3O_2)_2 \bullet 2H_2O$)	Sigma-Aldrich, Malaysia
		Cobalt acetate tetrahydrate ($Co(C_2H_3O_2)_2 \bullet 2H_2O$)	Sigma-Aldrich, Malaysia
		Sodium hydroxide (NaOH)	Sigma-Aldrich, Malaysia
		Urea (CH_4N_2O)	Sigma-Aldrich, Malaysia
Capactive electrode	Active material	Activated carbon (AC)	Sigma-Aldrich, Malaysia
Electrode fabrication	Substrate	Nickel foam (substrate)	Urich Technology, Malaysia
	Binder	Polyvinylidene fluoride (PVDF)	Sigma-Aldrich, Malaysia
	Solvent	N-methyl-2-2pyrrolidone (NMP)	Sigma-Aldrich, Malaysia
	Conductive powder	Acetylene black	Sigma-Aldrich, Malaysia
Electrolyte		Potassium hydroxide pellets (KOH)	Sigma-Aldrich, Malaysia

Table 3.2: Electrolyte and electrodes used in this thesis.

Type of electrode		**Source**
Reference electrode	Silver/Silver chloride (Ag/AgCl)	BASi® Analytical Instrument, USA
Counter electrode	Platinum (Pt) wire	BASi® Analytical Instrument, USA

3.2 Methodology

3.2.1 Synthesis of polyaniline (PANI)

PANI was synthesized through chemical oxidative polymerization of aniline monomer using APS as the oxidizing agent. 0.25 M aniline was added into 20 mL of 1M HCl and stirred for 30 minutes to form anilinium ions. For polymerization of PANI, acidic medium (pH < 3) is required as it can minimize the formation of undesired branched product. Next, 0.1 M APS solution (prepared by dissolving into 30 mL of 1 M HCl) was added drop wise into the anilinium solution and allowed for stirring for overnight. The formed emeraldine green precipitate was washed with 0.2 M HCl and acetone for several times to remove residues. Finally, the precipitates were dried at room temperature. The polymerization of PANI can be recognized by colour change followed by heat release caused by the autoacceleration nature of exothermic reaction.

3.2.1.1 Mechanism of PANI formation

The polymerization of PANI generally follows three fundamental steps (Molapo et al., 2012);

i) *Oxidation of monomer*: The initial step begins with the oxidation of aniline to a radical anilinium cation. Anilinium cation stabilizes itself through various resonating structures (where the radical is localized over entire benzene ring).

ii) *Radical coupling and re-aromatisation*: Head-to-tail reaction between the anilinium radical cation and its resonace form in acidic environment, yielding a dicationic dimer species. The dimers immediately oxidized to form dimerized radical cation.

iii) *Formation of PANI*: The dimers form of radical cations react with anilinium cation or dimer cation radical to generate a trimer of tetramer via electrophilic aromatic substituition. The repeatitions of the above steps eventually leads to the formation of PANI chains.

3.2.2 Synthesis of zinc cobaltite ($ZnCo_2O_4$) and polyaniline-zinc cobaltite nanocomposite (PANI-$ZnCo_2O_4$)

$ZnCo_2O_4$ nanoparticles were initially synthesized by hydrothermal method. $Zn(O_2CCH_3)_2 \cdot 2H_2O$ (15 mmol), $Co(C_2H_3O_2)_2 \cdot (H_2O)_4$ (15 mmol), urea (20 mmol) and 3.4 mL NH_3 were added into a mixture of deionized water-ethanol and stirred for 16 h. The mixture was then transferred into Teflon-lined stainless steel autoclave and heated up to 180 °C for 6 h. Subsequently, the sample was cooled down to room temperature, it was then washed with deionized water and dried at 60 °C. Next, the synthesized $ZnCo_2O_4$ nanoparticles were physically blended with the synthesized PANI with the weight ratio of PANI:$ZnCo_2O_4$=5:1). The blending of PANI and $ZnCo_2O_4$ nanoparticles was done using pestle mortar until homogenous mixture was achieved.

3.2.2.1 Mechanism of $ZnCo_2O_4$ formation

$ZnCo_2O_4$ was synthesized via hydrothermal method. Firstly, $Zn(O_2CCH_3)_2$ and $Co(C_2H_3O_2)_2$ were dissolved in deionized water at room temperature to obtain homogenous mixture solution. Then, urea was added into the solution and was slowly hydrolysed into CO_3^{2-} and OH^- anions. The solution containing Zn^{2+} and Co^{2+} cations reacted with the generated anions to start the process of nucleation and formed a precipitate. The OH^- concentration increased after the addition of ammonia, so due to fast hydrolysis, more crystal nucleus were formed. Finally, upon the hydrothermal treatment, the spherical shape of $ZnCo_2O_4$ nanoparticles were obtained (Garg et al., 2014).

3.2.3 Synthesis of nickel phosphate ($Ni_3(PO_4)_2$)

$Ni_3(PO_4)_2$ was synthesized through sonochemical method followed by calcination at different temperatures. 10 mL ethylene glycol was added drop wise into 15 mM of $Ni(CH_3COO)_2{\cdot}4H_2O$ solution followed by the addition of 15 mM Na_2HPO_4 while the solution was being sonicated for 30 min. The mixture turned from clear solution to light green colloidal precipitates which indicated the formation of $Ni_3(PO_4)_2$. The precipitates were washed several times with deionized water and dried at 60 °C. The dried powder was subsequently calcined at 300 °C in a muffle furnace for 3 h. The whole procedure was repeated for different calcination temperature of 600 and 900 °C (Figure 3.1) and the designation of the products can be referred to Table 3.3.

Table 3.3: Different calcination temperature used to synthesize $Ni_3(PO_4)_2$.

Calcination temperature (°C)	Designation
300	N300
600	N600
900	N900

3.2.3.1 Mechanism of $Ni_3(PO_4)_2$ formation

Formation of $Ni_3(PO_4)_2$ involves three stages. First stage of the mechanism was the reaction between nickel acetate and water at room temperature with stir, generating nickel hydroxide ($Ni(OH)_2$). When ethylene glycol was added into $Ni(OH)_2$, it act as a surfactant to reduce the agglomeration of particles. It is worth to be mentioning that, the surfactant can modulate the available surface energy of the particle so that the surface tension decreases, allowing particles to escape the aggregation process and lowering the mean particle size (Merkus & Meesters, 2013). For second stage, $Ni_3(PO_4)_2$ was already formed after mixed $Ni(OH)_2$ with Na_2HPO_4 (as the phosphate source) during sonochemical process. At the final stage of the synthesis procedure, the adsorbed water and organic molecules were removed during calcination and pure $Ni_3(PO_4)_2$ was obtained. The formation step of $Ni_3(PO_4)_2$ is illustrated in Figure 3.1.

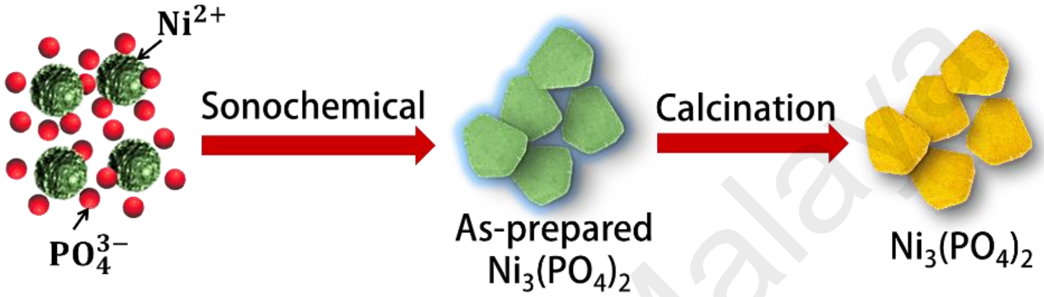

Figure 3.1: Synthesis scheme of $Ni_3(PO_4)_2$.

3.2.4 Synthesis of nickel phosphate-silver phosphate nanocomposite ($Ni_3(PO_4)_2$-Ag_3PO_4)

The synthesis step for $Ni_3(PO_4)_2$-Ag_3PO_4 is the continuous to the steps presented in the previous section. In this system, diamminesilver (I) complex ($Ag(NH_3)_2^+$) solution was firstly prepared using sonochemical process. The reduction of Ag^+ was carried out by the addition of 4.3 mL of NH_3 solution into 50 mM $AgNO_3$ solution under sonication using horn sonicator. The solution turned from dark brown precipitates into clear solution indicated the formation of $Ag(NH_3)_2^+$. The sonication was continued for another 30 min. The $Ag(NH_3)_2^+$ solution was then mixed with 0.05 g of the as-prepared $Ni_3(PO_4)_2$ (i.e. N0) and vigorously stirred for 3 h. The final precipitates were washed with deionized water for several times, dried at 60 °C and subsequently calcined at 300 °C. The whole procedure was repeated using different amount of $Ni_3(PO_4)_2$; 0.1, 0.2 and 0.3 g and the designation can be referred to Table 3.4.

Table 3.4: Weight ratios of $AgNO_3$:N0 used for the preparation of $Ni_3(PO_4)_2$-Ag_3PO_4.

Mass of $AgNO_3$ (mg)	Mass of N0 (mg)	Weight ratio ($AgNO_3$:N0)	Designation
0.377	50	1:0.132	0.05 NAg
0.377	100	1:0.265	0.1 NAg
0.377	200	1:0.530	0.2 NAg
0.377	300	1:0.794	0.3 NAg

3.2.4.1 Mechanism of $Ni_3(PO_4)_2$-Ag_3PO_4 formation

During the synthesis process, N0 suspension (in deionized water) with the attached negatively charge hydrogen phosphate (HPO_4^{2-}) ions was initially formed by sonication as demostrated in Section 3.2.3. Then, during the mixture of positively charge diammine silver complex ($Ag(NH_3)_2^+$) with N0 suspension, the electrostatic interaction was happened which caused the $Ag(NH_3)_2^+$ molecules attracted towards the phosphate groups and self-assembled in the surrounding N0 particles (Kyriakidou et al., 2016). Due to the presence of excess of HPO_4^{2-} in N0, HPO_4^{2-} were also interacted with Ag^+ and subsequently resulted on the formation of binary composite of $Ni_3(PO_4)_2$-Ag_3PO_4. Upon calcination at 300 °C, ammonium cations (NH_4^+) and other residual solvents were removed except the $Ni_3(PO_4)_2$-Ag_3PO_4 (Pinnavaia et al., 2000). The formation of binary composite of $Ni_3(PO_4)_2$-Ag_3PO_4 is potrayed in Figure 3.2.

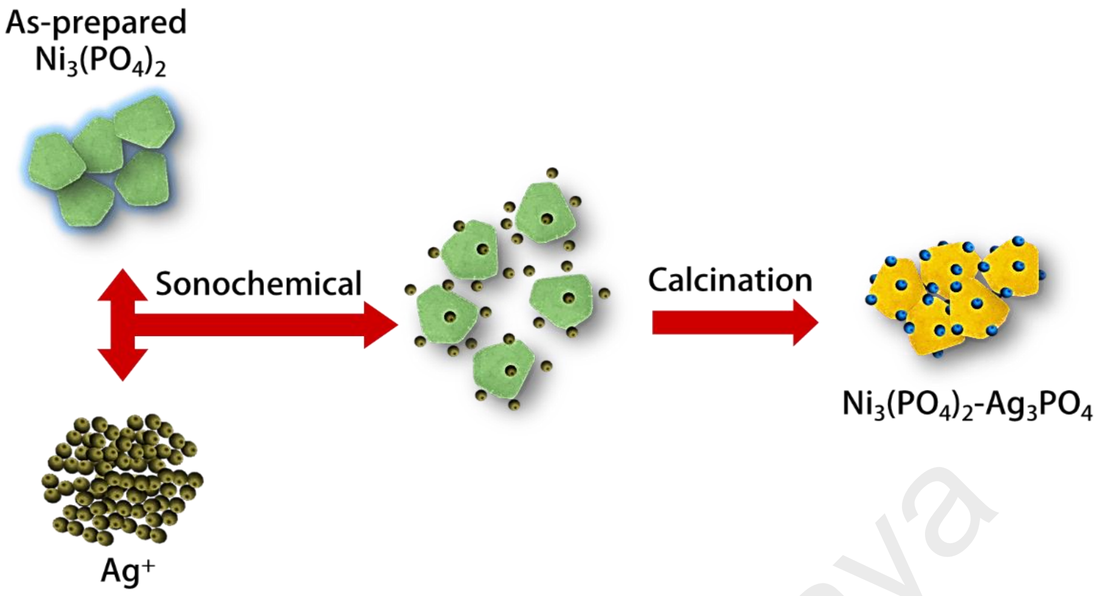

Figure 3.2: Synthesis scheme of $Ni_3(PO_4)_2$-Ag_3PO_4.

3.2.5 Preparation of polyaniline-nickel phosphate-silver phosphate nanocomposite (PANI-$Ni_3(PO_4)_2$-Ag_3PO_4)

Polyaniline-nickel phosphate-silver phosphate nanocomposite (PANI-$Ni_3(PO_4)_2$-Ag_3PO_4) was prepared by blending PANI with NAg nanocomposite using pestle mortar. Firstly, 10 mg of PANI powder was blended with few drops of dionized water until smooth slurry was formed. Then, 10 mg of 0.1 NAg powder was added into PANI slurry and continue blended using mortar until the mixture became homogenous. Next, the slurry was dried under 60 °C for 1 h. The whole process was repeated using different amount of PANI powder and the designation of the nanocomposites can be referred to Table 3.5. The blending process must be properly done so that the particles would not be agglomerated.

Table 3.5: Weight ratios of PANI:0.1 NAg used for the preparation of PANI-$Ni_3(PO_4)_2$-Ag_3PO_4.

Mass of PANI (mg)	Mass of 0.1 NAg (mg)	Weight ratio (PANI:0.1 NAg)	Designation
20	10	2:1	PNAg (2:1)
10	10	1:1	PNAg (1:1)
10	20	1:2	PNAg (1:2)
10	30	1:3	PNAg (1:3)

3.2.5.1 Mechanism of PANI-$Ni_3(PO_4)_2$-Ag_3PO_4 formation

The ternary composite of PANI-$Ni_3(PO_4)_2$-Ag_3PO_4 was synthesized via electrostatic interaction between oppositely charged $Ni_3(PO_4)_2$-Ag_3PO_4 and PANI. The synthesized $Ni_3(PO_4)_2$-Ag_3PO_4 possess negatively charge of PO_4^{3-} groups on the surface, and PANI contain positively charged of $-NH^+$ groups in the backbone. Thus, during blending process, the available $-NH^+$ groups in PANI enabled strong electrostatic interactions with the charged surface of $Ni_3(PO_4)_2$-Ag_3PO_4. The formation of PANI-$Ni_3(PO_4)_2$-Ag_3PO_4 is displayed in Figure 3.3.

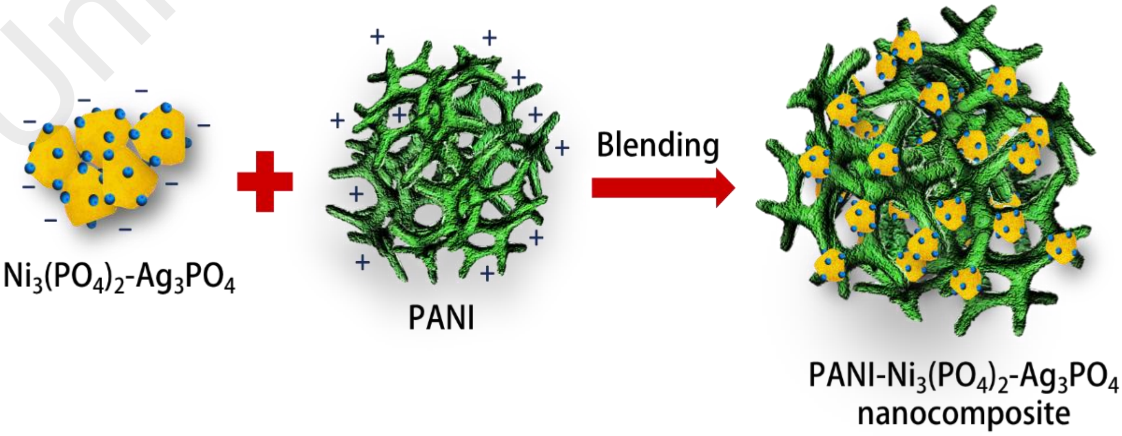

Figure 3.3: Synthesis scheme of PANI-$Ni_3(PO_4)_2$-Ag_3PO_4.

3.2.6 Battery-type electrode and capacitive electrode fabrication

The battery-type electrodes was fabricated by mixing 75 wt. % of the active material (synthesized sample i.e. PANI-$ZnCo_2O_4$, $Ni_3(PO_4)_2$, $Ni_3(PO_4)_2$-Ag_3PO_4 and PANI-$Ni_3(PO_4)_2$-Ag_3PO_4), 15 wt. % of acetylene black (as the conductive powder) and 10 wt. % of PVDF (to act as a binder) in NMP solvent until a homogeneous slurry was obtained. Then, 1x1 cm^2 of cleaned nickel foam (Ni foam) was coated with the prepared slurry and dried in an oven at 90 °C for overnight.

For supercapattery evaluation, capacitive electrode was also prepared to function as the complementary electrode for battery-type electrode in supercapattery. The fabrication of capacitive electrode was prepared by mixing 75 wt. % of commercial AC, 15 wt. % of acetylene black and 10 wt. % of PVDF in NMP solvent until a homogeneous slurry was achieved. Then, 1x1 cm^2 of cleaned nickel foam (Ni foam) was coated with the prepared slurry and dried in an oven at 90 °C for overnight.

The mass loading of the active material on the Ni foam can be calculated by the following steps;

Mass of dried coated Ni foam: x g

Mass of bare Ni foam: y g

Threfore, the mass loading of the active material (g) = $(x - y)\text{g} \times 75\ \%$.

*75 % is referring to the weight percentage of active material.

The measured mass loading of PANI, PANI-$ZnCo_2O_4$, $Ni_3(PO_4)_2$, $Ni_3(PO_4)_2$-Ag_3PO_4, PANI-$Ni_3(PO_4)_2$-Ag_3PO_4 and AC (without acetylene black and PVDF) was approximately 3.8 mg.

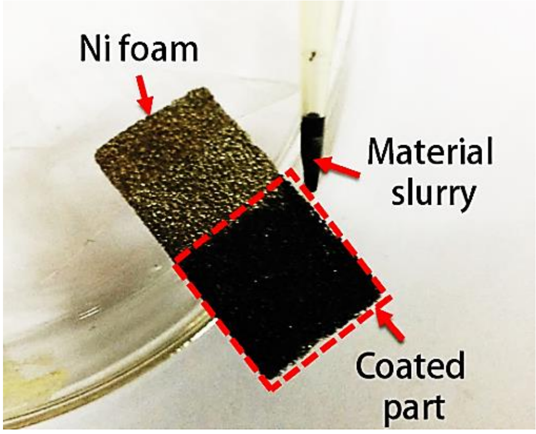

Figure 3.4: Coated Ni foam.

3.2.7 Supercapattery assembly

Supercapattery was designed to evaluate the performance of the synthesized materials as a device. The evaluation can be conducted using two-electrode cell that is connected to the potentiometer. Supercapattery was assembled by combining positive electrode with negative electrode. Commonly in supercapattery, positive electrode uses battery-type material as the active material and negative electrode uses capacitive-type material as the active material. In this work, the synthesized samples and commercialized AC were used as the active materials for positive electrode and negative electrode, respectively. The electrodes were separated by inserting filter paper (acts as separator) in between the electrodes as illustrated in Figure 3.5. The separator is important as it can avoid the positive and negative electrodes from touch each other and create a short-circuit during running the experiment. These combined layers were then soaked in 1 M KOH liquid electrolyte.

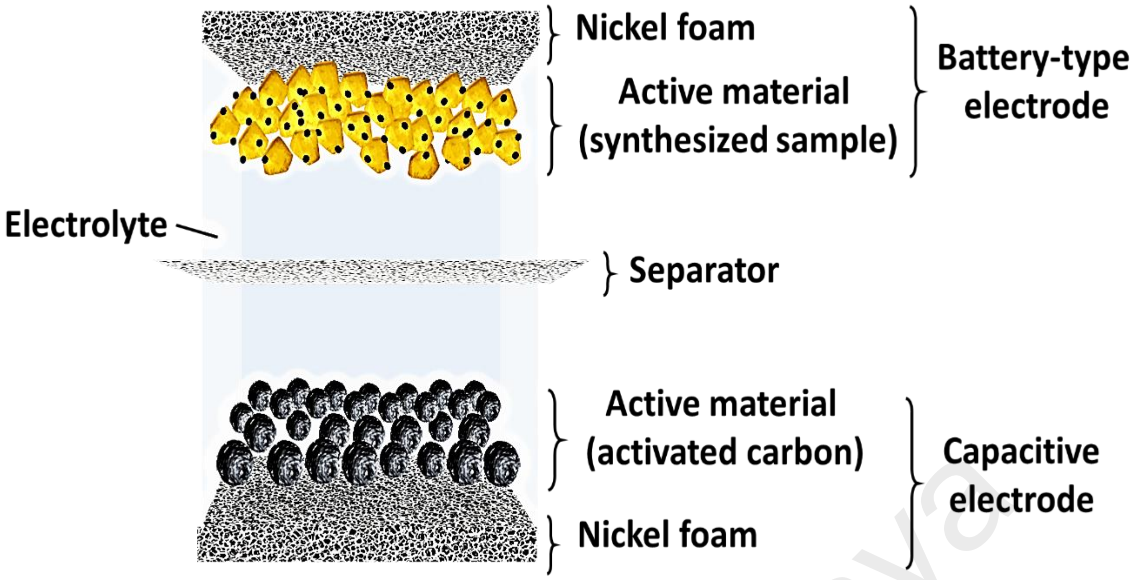

Figure 3.5: Different components in supercapattery.

3.3 Characterization techniques

3.3.1 X-ray diffraction

X-ray diffraction (XRD) is a X-ray based technique which is required to identify the crystallinity of the sample and can supply the information on unit cell dimensions. Running XRD requires the powdered sample to be finely ground (to randomize orientation) and placed into a sample holder. The crystallinity of the samples in this work were studied through X-ray diffraction (XRD; D5000, Siemens), using copper K_a radiation ($\lambda = 1.5418$ °A) at a scan rate of 0.02 s^{-1} with a scanning diffraction angel (2θ) from 10° to 70°. The unit cell was analysed using PANanalytical X'pert Highscore software.

3.3.2 Fourier transform infrared spectroscopy

Fourier transform infrared spectroscopy (FTIR) is used to examine the presence of functional groups in the samples. The analysis was conducted using Thermo Scientific Nicolet ISIO Smart ITR) on which the powdered sample was directly observed. The measurement was scanned from 500 to 4000 cm^{-1} at a resolution of 1 cm^{-1} in transmission mode.

3.3.3 The X-ray photoelectron spectroscopy

The elemental composition, chemical state and electronic state of the element that exist in the sample is determined through X-ray photoelectron spectroscopy (XPS) analysis. The sample was prepared by dispersing the sample powder into ethanol solvent and coated on cleaned silicon wafer. The survey spectra were recorded in the range of 0 - 1000 eV at a pass energy of 200 eV with a resolution of 1 eV, while high-resolution spectra were recorded with a pass energy of 50 eV within a resolution of 0.1 eV. The spectra were fitted into multiple Gaussian curves using Origin Pro 8.1 software.

3.3.4 Electron microscopy

The morphology of the samples were visualized by field emission scanning electron microscopy (FESEM, JEOL JSM-7600F) and high-resolution transmission electron microscopy (HRTEM, JEOL JEM-2100 F). FESEM focusses on the surface morphology of the samples and composition whereas HRTEM focusses on the internal composition and crystallization of the samples. The sample viewed through FESEM was in powder which is pasted on carbon tape, and coated with a thin layer of gold (to prevent charge accumulation on the surface of sample). For HRTEM analysis, a very light amount of sample was first dispersed in ethanol solvent. Then the dispersed sample was dropped on the copper grid and dried at room temperature for at least five days. To justify the presence of different elements in the sample, energy dispersive X-ray (EDX) analysis and elemental mapping were employed.

3.4 Evaluation of electrochemical behaviour

Two types of standard electrode connection was used to measure the electrochemical performance of synthesized materials i.e. three-electrode connection (has three terminals) and two-electrode connection (has two terminals). A three-electrode connection was employed for single electrode measurement. Basically, three different types of electrodes are needed; the coated nickel foam comprises the active material (as working electrode), Ag/AgCl (as reference electrode) and platinum wire (as counter electrode) (Figure 3.6). Working electrode is where the reaction of interest is happening. Ag/AgCl is the electrode which has fixed potential and functions as a point of reference in the electrochemical cell to control the potential of working electrode. Platinum wire is used to complete the current circuit in the electrochemical cell to allow the flow of current. Two-electrode connection does not require any standard electrode and this connection was used for assessing the performance of the assembled supercapattery. One terminal was connected to battery-type electrode and the other terminal was connected to capacitive electrode. When voltagae is applied, battery-type electrode become positively charged and capacitive electrode become negatively charged. For both electrode connections, the measurements were carried out in 1 M KOH electrolyte at room temperature. The electrochemical performance of single electrode and supercapattery was carried out via cyclic voltammetry (CV), galvanostatic charge-discharge (GCD) and electrochemical impedance spectroscopy (EIS) techniques using a Gamry Instrument Interface 1000.

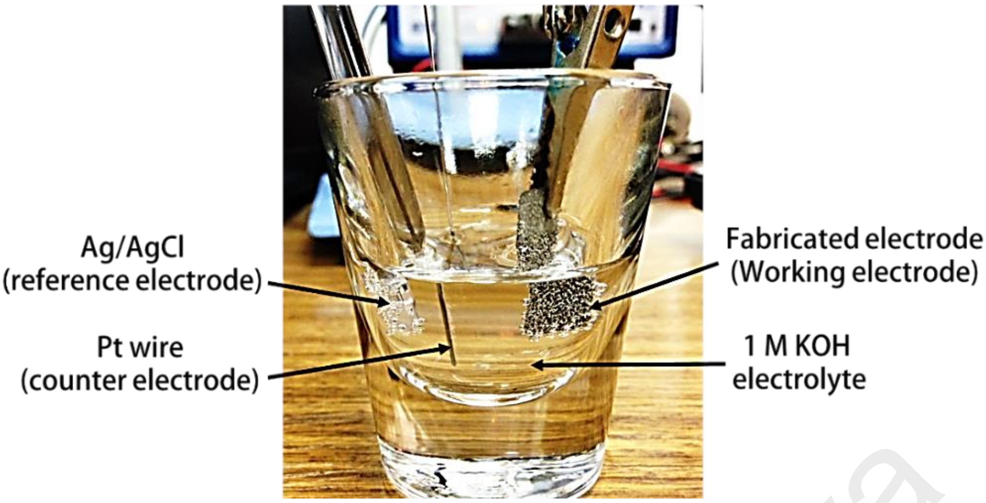

Figure 3.6: Three different types of electrode used in three-electrode cell setup.

3.3.1 Cyclic voltammetry (CV)

CV is the mostly commonly used technique for studying the potential or electrochemical behaviour of the fabricated electrode. This technique measures the output current resulting from the potential scanning between two pre-determined voltages at a constant scan rate (Figure 3.7). In supercapattery, the forward and reverse scan is conducted from a wider range of potential, typically from -1 to 1 V in order to determine the stable potential window. Thus, two parameters can be adjusted; scan rate (mV/s) and potential range (V) to confirm the type of reaction for energy storage and to fix the operating potential window, respectively. In this work, the CV is repeated at different scan rate (5 - 100 mV/s) within the potential of 0 - 0.6 V. The variation in scan rates can give an information on the reversibility of charge storage reaction by studying the shape and are of CV curve. The specific capacity (Q_S) from the CV can be determined using the equation as follows;

$$Q_S = \frac{1}{vm}\int_{Vi}^{Vf} I \times VdV \tag{3.1}$$

Where v: scan rate (mV/s), m: mass of active material (g), V:potential (V). The integral can be calculated using Microsoft Excel.

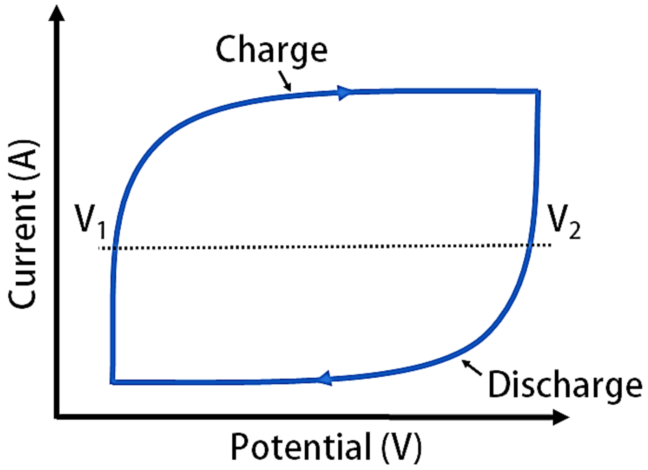

Figure 3.7: Standard CV profile.

3.3.2 Galvanostatic charge-discharge (GCD)

The GCD technique can be regarded as the additional analysis to the CV for calculating the specific capacity of the electrode. This technique can be used to measure the resistance of the electrode or cell, life cycle, energy density and also power density of the fabricated supercapattery. For GCD, two parameters can be tuned; potential range (V) and applied current (A). The range of current density (=applied current (A)/mass of active material on Ni foam (g)) used in this work was varied from 1 A/g (lowest) to 8 A/g (highest) to study the rate capability of the fabricated electrodes (will be explained in the next chpater). Basically in GCD profile, it has two types of curves which are capacitive and resistive as shown in Figure 3.8. The capacitive curve is contributed from the voltage change corresponding to the charge/energy storage. The resistive curve is contributed from the ESR of the cell. The specific capacity (Q_S) from GCD anylisis can be calculated using equation below;

$$Q_S = \frac{I \times \Delta t}{m} \tag{3.2}$$

where I: the current (A), Δt: the discharge time (s) and m: the mass of active material (g).

The calculated Q_S can be used to determine the energy density (E_d) and power density (P_d) of supercapattery using equation 3.3 and equation 3.4. Briefly, E_d is the amount of stored energy and P_d is the rate of charge and discharge.

$$E_d \text{ (Wh/kg)} = \frac{Q\Delta V}{2\times3.6} \tag{3.3}$$

$$P_d \text{ (W/kg)} = \frac{E\times3600}{\Delta t_d} \tag{3.4}$$

Where Q is the specific capacity, ΔV is the potential window and t_d is the discharge time.

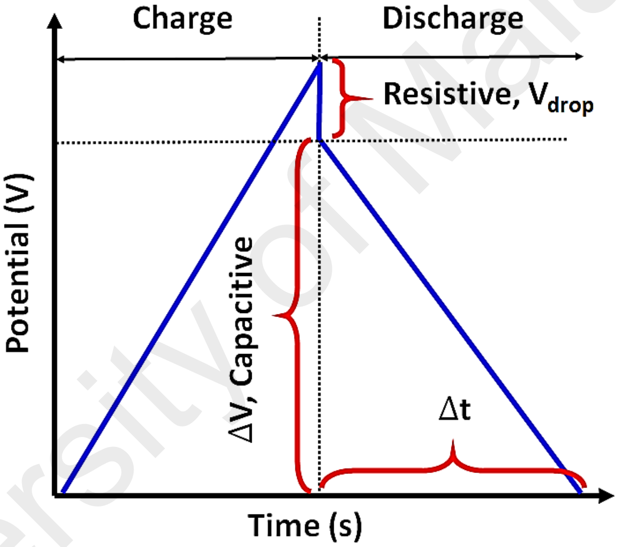

Figure 3.8: Charge-discharge profile.

3.3.3 Electrochemical impedance spectroscopy (EIS)

EIS measurement is important to access the frequency response, equivalent series resistance (ESR) and charge transfer rate of the fabricated electrodes. In supercapacitor, this technique can provide information on the electrochemical reactions that taking place during charging/discharging process. This technique is performed at open circuit potential with a sinusoidal signal of 10 mV (r.m.s), in a frequency from 0.01 Hz to 100 kHz. This techniques is useful for supercapacitor application study to evaluate the potential of new electrode materials. Generally, Nyquist plot is expressed in terms of a real phase (*Z'*) and an imaginary phase (*Z''*) as illustrated in Figure 3.9. The first intercept of the curves (ESR) value at the higher frequency region is contributed from the resistances of the entire system, i.e. electrode and bulk electrolyte (Zhong et al., 2015). The charge transfer resistance (R_{ct}) can be determined from the diameter of semicircle which can estimate the charge transfer resistance at the electrode-electrolyte interface. While the slope of the Warburg impedance (W_d) deduced by the straight line can be related with the capacitive behaviour of electrode material. The steeper the slope of W_d parallel to the imaginary axis indicates good capacitive nature of electrode.

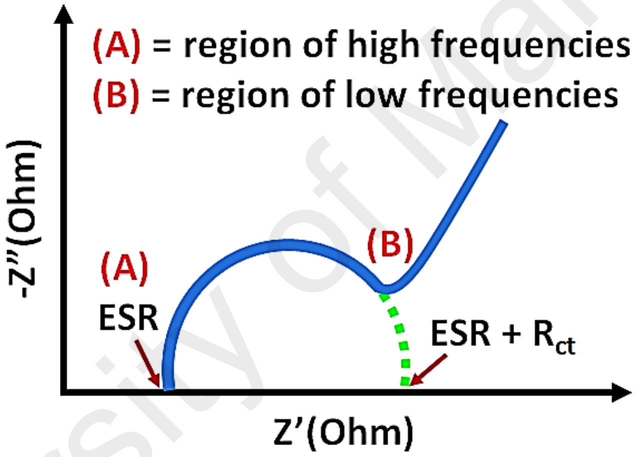

Figure 3.9: Nyquist diagram.

The characterization and electrochemical techniques demonstrated in this chapter have been used in the experimental investigation of all synthesized samples; PANI, PANI-$ZnCo_2O_4$, $Ni_3(PO_4)_2$, $Ni_3(PO_4)_2$-Ag_3PO_4 and PANI-$Ni_3(PO_4)_2$-Ag_3PO_4. Those techniques are important since a better understanding of the structural, morphology and electrochemical properties of all samples can be determined.

CHAPTER 4: RESULTS AND DISCUSSION

This chapter illustrates the results obtained for the PANI-$ZnCo_2O_4$ system and $Ni_3(PO_4)$, $Ni_3(PO_4)$-Ag_3PO_4, and PANI-$Ni_3(PO_4)$-Ag_3PO_4 systems.

4.1 System 1: Polyaniline-zinc cobaltite nanocomposite (PANI-$ZnCo_2O_4$)

4.1.1. XRD

The structural crystallinity of PANI, $ZnCo_2O_4$ and PANI-$ZnCo_2O_4$ was investigated by XRD analysis as shown in Figure 4.1. $ZnCo_2O_4$ exhibited several peaks at 18.9°, 31.2°, 36.8°, 38.4°, 44.7°, 55.7°, 59.2° and 65.1° correspond to the (111), (220), (311), (222), (400), (422), (511) and (440) lattice planes, respectively. These peaks are well indexed to cubic $ZnCo_2O_4$ with a spinel structure (JCPDS card no. 23-1390) and a space group of Fd3m (Wang et al., 2015). The appearance of these peaks signifies that $ZnCo_2O_4$ has crystalline structure. Whereas PANI displayed three peaks at 2θ value of 14.8°, 20.9° and 25.3° which can be assigned to the (011), (020) and (200) lattice planes of polycrystalline PANI chains.

PANI-$ZnCo_2O_4$ displayed the diffraction peaks corresponding to the spinel $ZnCo_2O_4$ as well as a broad peak of PANI, resulting from the effective intercalation between $ZnCo_2O_4$ particles and PANI matrix. No shift in peak position was observed indicating that $ZnCo_2O_4$ nanoparticles are just anchored on the surface of PANI without affecting the chemical composition of PANI and $ZnCo_2O_4$. In addition, the peak of PANI turned broader which might be due to some parts of PANI have been coated with $ZnCo_2O_4$ particles. Thereby, XRD diffractograms established the effective synthesis of PANI-$ZnCo_2O_4$.

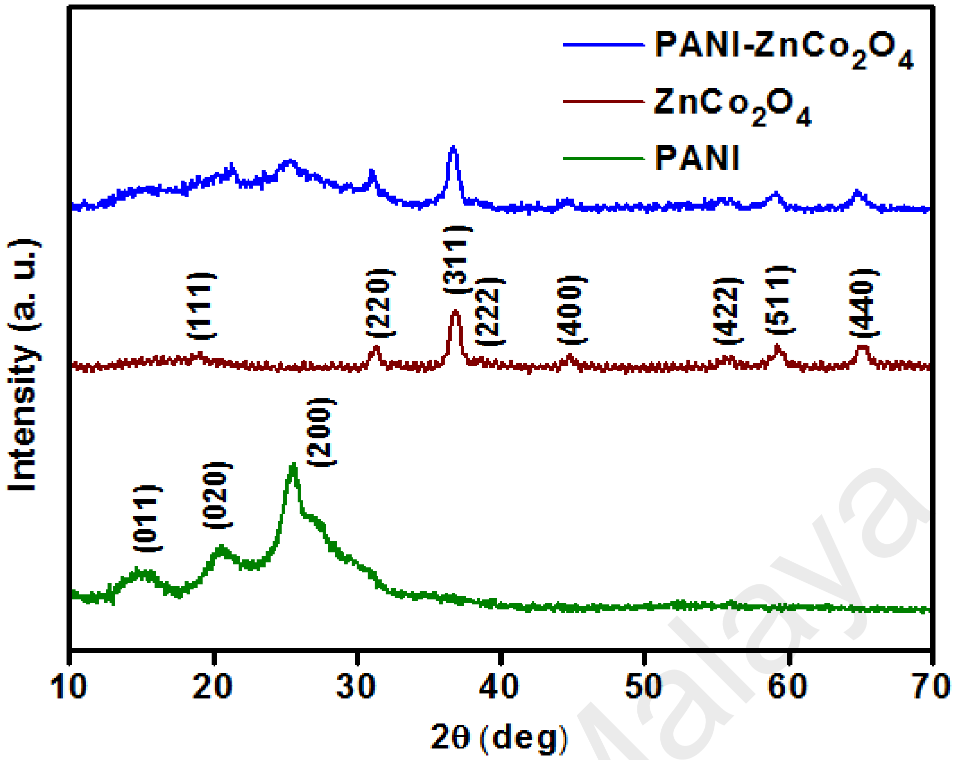

Figure 4.1: XRD diffractogram of PANI, $ZnCo_2O_4$ and PANI-$ZnCo_2O_4$.

4.1.2. FTIR

The purity of PANI, $ZnCo_2O_4$ and PANI-$ZnCo_2O_4$ was further studied by FTIR analysis as depicted in Figure 4.2. Two strong transmittance bands observed at $ZnCo_2O_4$ correspond to the spinel structure of $ZnCo_2O_4$. The band at 565 cm^{-1} corresponds to the M−O stretching vibration of octahedrally coordinated cobalt ions, and the band at 662 cm^{-1} was attributed to the M−O stretching vibration of tetrahedrally coordinated zinc ions (Wei et al., 2007). In case of PANI, the bands around 1470 cm and 1560 cm^{-1} were arising from $-C=C$ stretching vibrations of benzenoid and quinonoid structures. The observed band at 1294 cm^{-1} was assigned to the C−N stretching of secondary aromatic amine. PANI-$ZnCo_2O_4$ exhibited similar bands as shown by $ZnCo_2O_4$ and PANI but all bands were slightly red-shifted. This was an indication that the formation of molecular interaction between $ZnCo_2O_4$ and PANI chain in the nanocomposite. Besides, the intensity of M−O stretching vibration of both octahedrally coordinated cobalt ions and tetrahedrally coordinated zinc ions bands that was observed at PANI-$ZnCo_2O_4$ is relatively weak as compared to that of $ZnCo_2O_4$. This was attributed to the low number of spinel structure of $ZnCo_2O_4$ that intercalated with PANI (Bajaj et al., 2013).

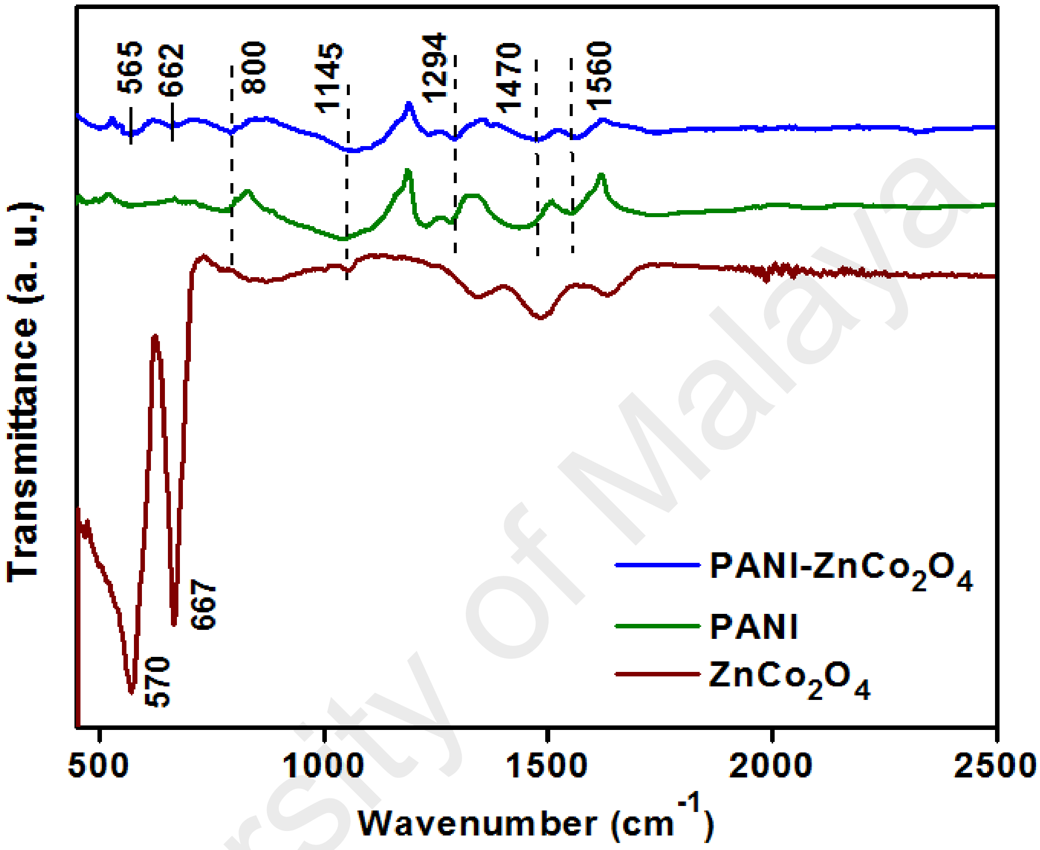

Figure 4.2: FTIR spectra of PANI, $ZnCo_2O_4$ and PANI-$ZnCo_2O_4$.

4.1.3. FESEM

The surface morphology of PANI, $ZnCo_2O_4$ and PANI-$ZnCo_2O_4$ were visualized by FESEM analysis. Figure 4.3 presents the irregular shape of $ZnCo_2O_4$ nanoparticles with an average size of 30 nm. Some agglomerations can be seen which arised from the Van der Waals interaction between the nanoparticles. Figure 4.4 displays the interconnected tubular shape of PANI with a diameter of 110 nm. Such morphology was formed due to the effect of the proton acid doping into PANI which increases the polarity of the molecules. This causes the interaction of the molecular chains and consequently the tubular shape of PANI are connected with each other (Cai et al., 2017). Tubular structure is beneficial for supercapattery application as this structure generally can provide electrical pathway for electron mobility. Figure 4.5 shows the $ZnCo_2O_4$ nanoparticles were decorated along the tubular PANI. High magnification of FESEM image (Figure 4.5 (inset)) shows the anchored $ZnCo_2O_4$ nanoparticles along the PANI chain which proved the effective blending method to incorporate $ZnCo_2O_4$ with PANI. The agglomeration of $ZnCo_2O_4$ nanoparticles that anchored on PANI deemed to be less as compared to pure $ZnCo_2O_4$. This would augment the liquid-solid interfacial area and hence promising an improved electrochemical performance.

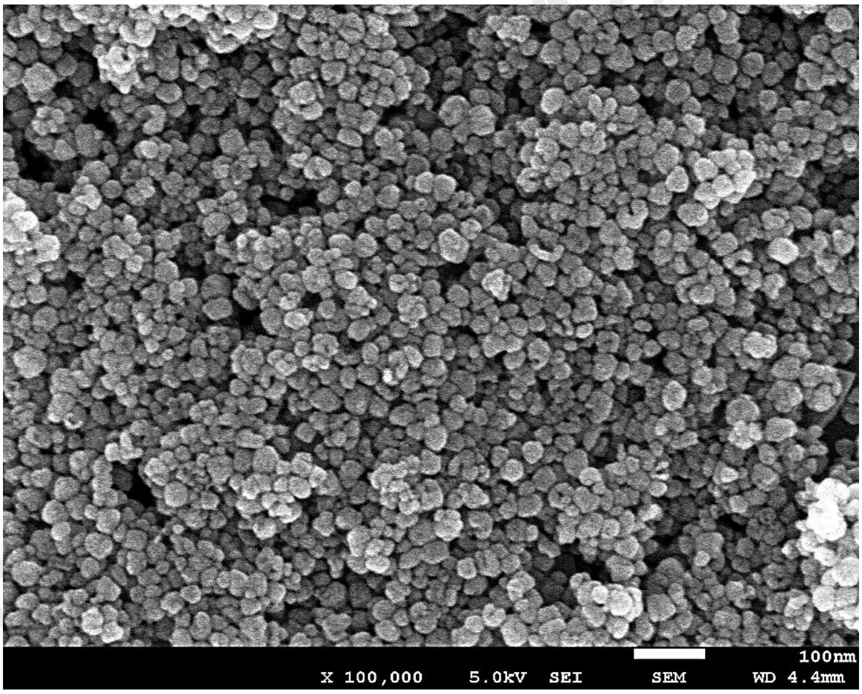

Figure 4.3: FESEM image of $ZnCo_2O_4$.

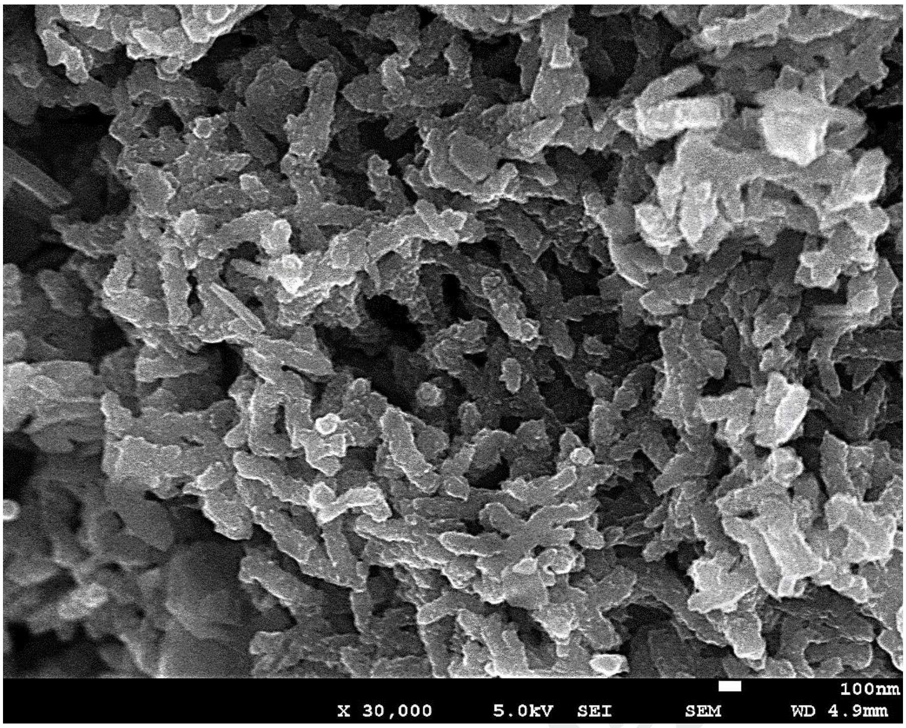

Figure 4.4: FESEM image of PANI.

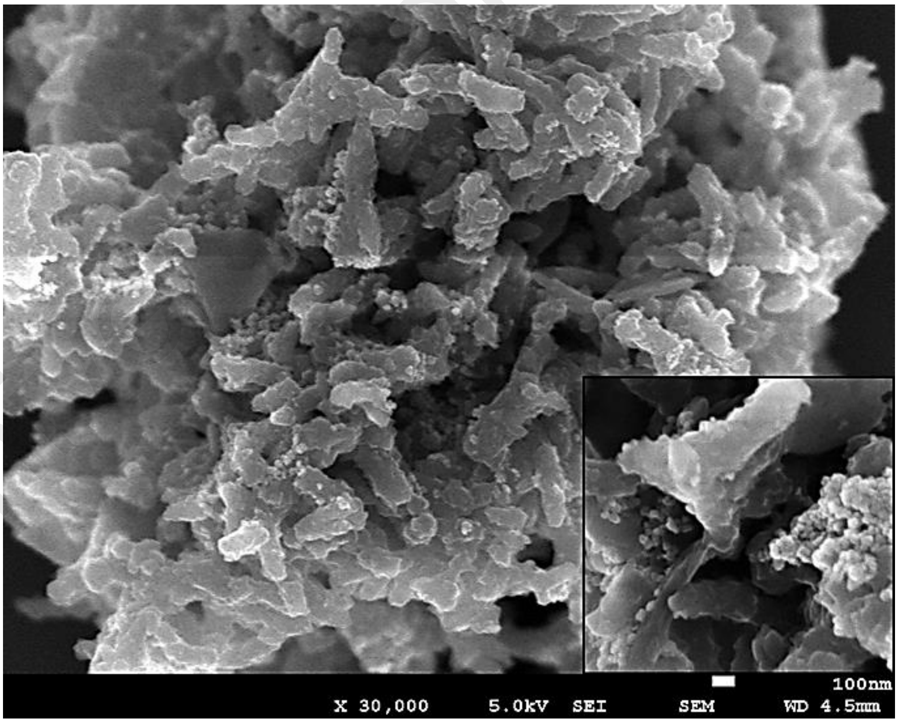

Figure 4.5: FESEM image of PANI-$ZnCo_2O_4$.

4.1.4 Electrochemical studies (Three-electrode cell)

4.1.4.1 CV

The electrochemical performance of $ZnCo_2O_4$ nanoparticles after the incorporated of PANI was first studied using three-electrode cell system with a potential range of 0–0.5 V (versus Ag/AgCl) in 2 M KOH electrolyte. Figure 4.6(a-c) present the CV curves of the $ZnCo_2O_4$, PANI and PANI-$ZnCo_2O_4$ electrodes at a scan rate of 30 mV/s, respectively. All CV curves exhibited redox peaks, elucidating the electrodes stored charges via faradaic reaction which are the characteristic of battery-type electrodes (Brousse & Daniel, 2015). Furthermore, the shape of the CV curves was not significantly influenced by increasing scan rates, demonstrating that all electrodes have good rate capability (Jiang et al., 2015). Moreover, it was observed from these figures that the peak currents increase with increasing scan rates and the anodic and cathodic peaks shifted to higher and lower potentials, respectively. This can be related with the electric polarization and irreversible redox reactions occurring at the electrode surface (Umeshbabu et al., 2015).

Figure 4(d) shows the comparison in CV curves between $ZnCo_2O_4$, PANI and PANI-$ZnCo_2O_4$ at a scan rate of 30 mV/s. It should be mentioning that the specific capacity of the electrode is proportional to the area under the CV curves. Apparently, PANI-$ZnCo_2O_4$ showed a significantly larger enclosed area than that of unitary $ZnCo_2O_4$ and PANI, indicating that the higher electrochemical activity was obtained in PANI-$ZnCo_2O_4$. The calculated specific capacity values for pure $ZnCo_2O_4$ nanoparticles, PANI and PANI-$ZnCo_2O_4$ nanocomposite were found to be 109, 189 and 398 C/g, respectively, at a scan rate of 5 mV/s.

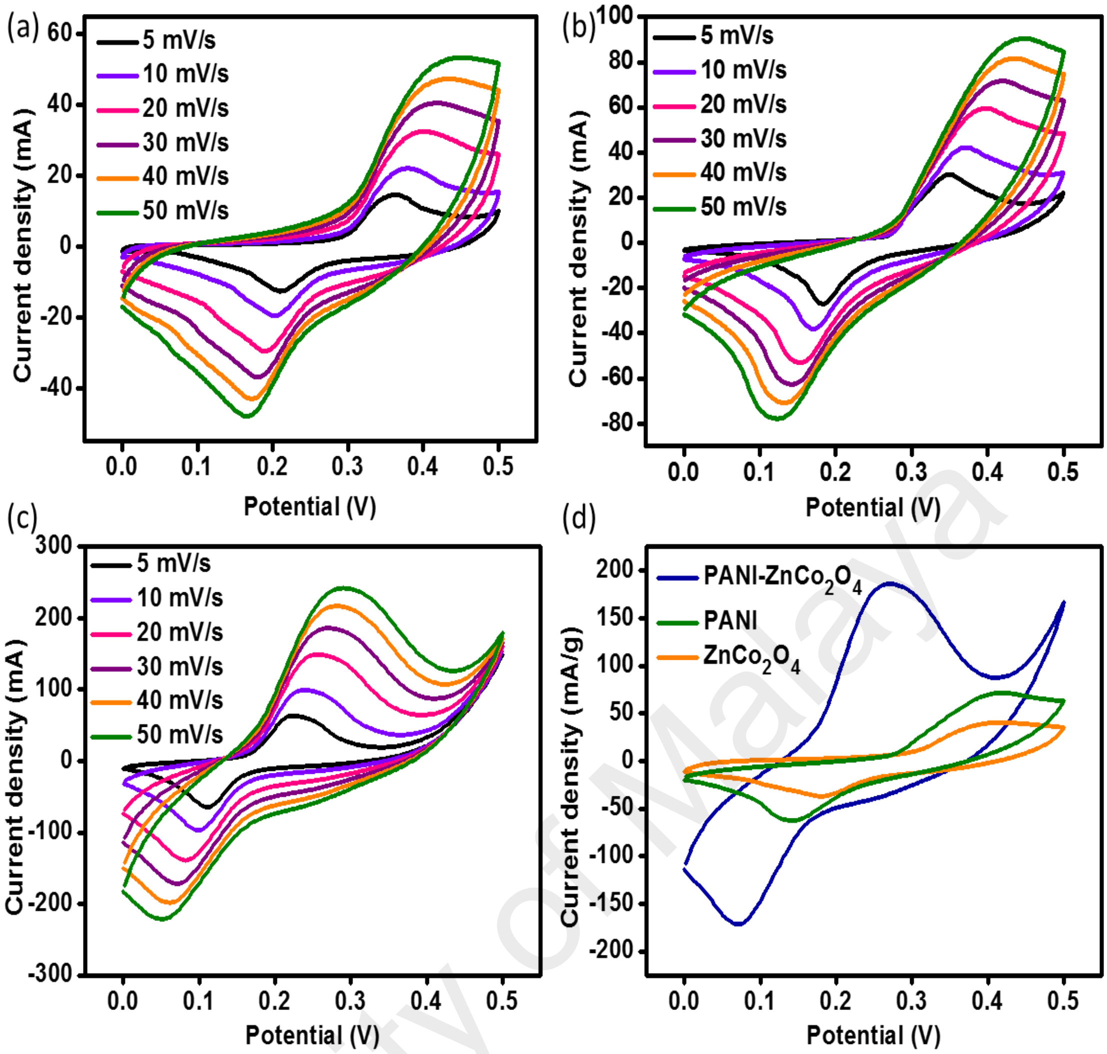

Figure 4.6: CV curves of (a) $ZnCo_2O_4$, (b) PANI and (c) PANI-$ZnCo_2O_4$ at different scan rates, (d) CV of $ZnCo_2O_4$, PANI and PANI-$ZnCo_2O_4$ at 30 mV/s.

4.1.4.2 GCD

The capability of the fabricated electrodes to store charge was also assessed using GCD technique with a potential range of 0 - 0.38 V. Figure 4.7(a-c) display the discharge time curves of $ZnCo_2O_4$, PANI and PANI-$ZnCo_2O_4$ electrodes decrease with increasing current density indicates lower specific capacity was achieved at higher current densities. This is due to the inadequate time for OH^- to diffuse deep into the electrode material during the electrochemical reaction at high scan rates. Whereas at lower scan rate, both inner and outer surface of the materials can be fully accessed by OH^- (Jahromi et al., 2015). All electrodes showed the nonlinear discharge curves at different current densities from 1 to 8 A/g due to the occurring of redox reaction between PANI-$ZnCo_2O_4$ and electrolyte ions during charging and discharging. The non-linear GCD curve is the typical shape of battery-type material characteristic. The maximum specific capacity of PANI-$ZnCo_2O_4$ was found to be 398 C/g, which is higher than PANI (380 C/g) and $ZnCo_2O_4$ (138 C/g) at 1 A/g, respectively. Figure 4.7(d) shows the plot of the calculated specific capacity value of PANI-$ZnCo_2O_4$ at different current densities. When the current density was increased up to 8 A/g, PANI-$ZnCo_2O_4$ achieved an enhanced specific capacity of 224 C/g (57 % retention), which is significantly higher than that of $ZnCo_2O_4$ and PANI. Whereas $ZnCo_2O_4$ and PANI has a specific capacity of 70 C/g (35 % retention) and 59 C/g (15 % retention), respectively. The highest specific capacity retention shown by PANI-$ZnCo_2O_4$ indicated its highest rate capability, suggesting the formation of higher electronic transfer network in PANI-$ZnCo_2O_4$. To further clarify the enhancement in charge transfer between the electrode material and electrolyte, the electrodes were analysed through EIS technique.

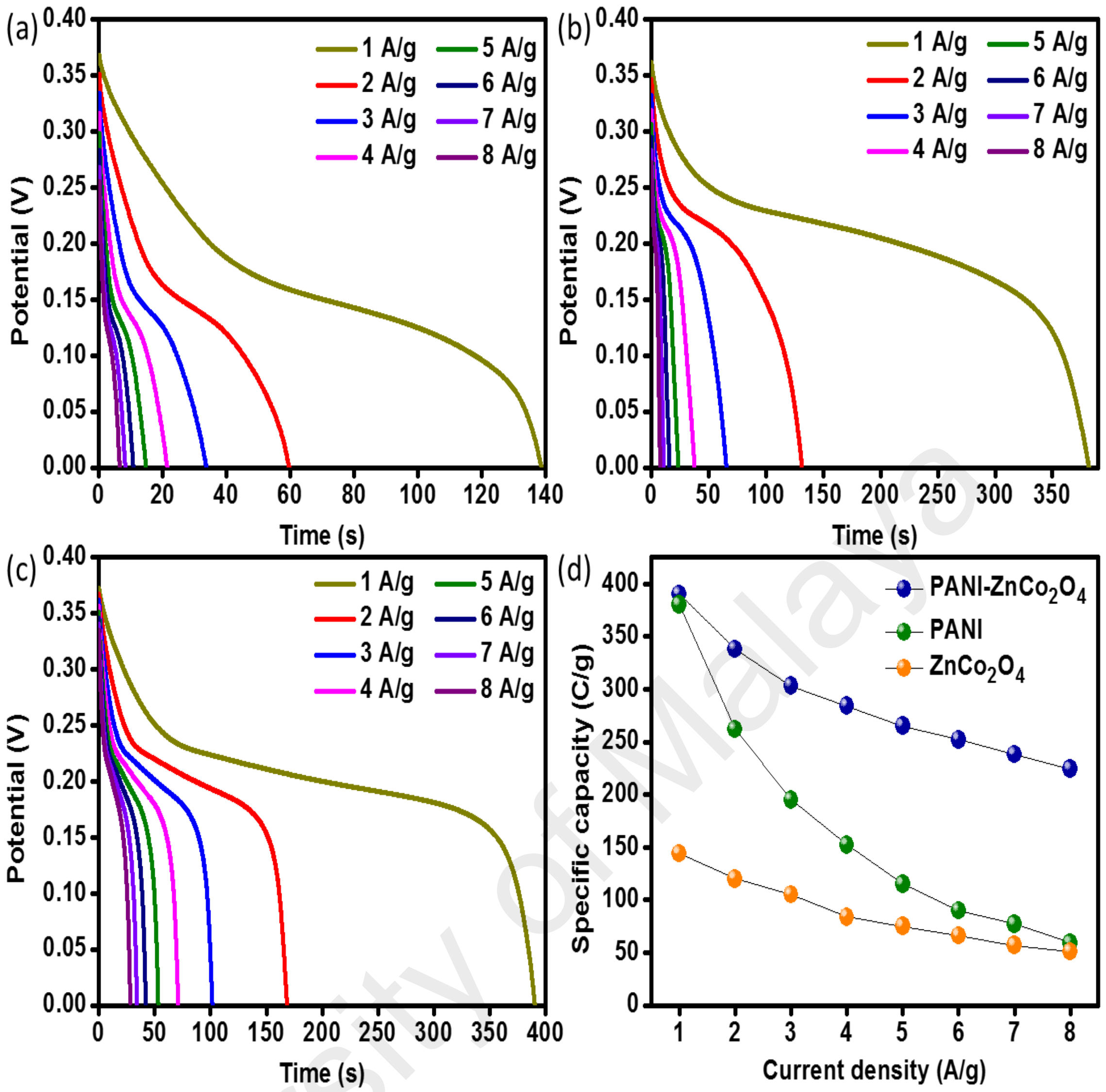

Figure 4.7: Discharge curve of (a) $ZnCo_2O_4$, (b) PANI and (c) PANI-$ZnCo_2O_4$ at the scan rate of 30 mV/s; (d) Specific capacity of $ZnCo_2O_4$, PANI and PANI-$ZnCo_2O_4$ at different current densities.

4.1.4.3 EIS

EIS measurements were recorded in a frequency of 10 mHz - 100 kHz, to further study the intrinsic mechanism occurred at the electrodes. Figure 4.8 depicts the Nyquist plots of the EIS spectra for $ZnCo_2O_4$, PANI and PANI-$ZnCo_2O_4$. A semicircle and a straight line can be seen at high-frequency and low-frequency region, respectively. The first intercept (ESR) of the semicircle typifies the resistance of electrolyte, the resistance of the active materials and the contact resistance between the electrolyte, current collector and the active materials. The ESR values were determined to be 0.9, 1.1 and 1.2 Ω for PANI-$ZnCo_2O_4$, PANI and $ZnCo_2O_4$, respectively, signifying PANI-$ZnCo_2O_4$ has enhanced electrical conductivity of $ZnCo_2O_4$ and PANI. The diameter of semicircle of $ZnCo_2O_4$ is larger than that of PANI and PANI-$ZnCo_2O_4$ which is attributed to the higher charge transfer resistance (R_{ct}) possessed by $ZnCo_2O_4$. The W_d deduced by the straight line is originated from the OH^- diffusion within the electrode material. PANI-$ZnCo_2O_4$ exhibited the most vertical line parallel to the imaginary axis which indicated its high capacitive behavior (Chen et al., 2016).

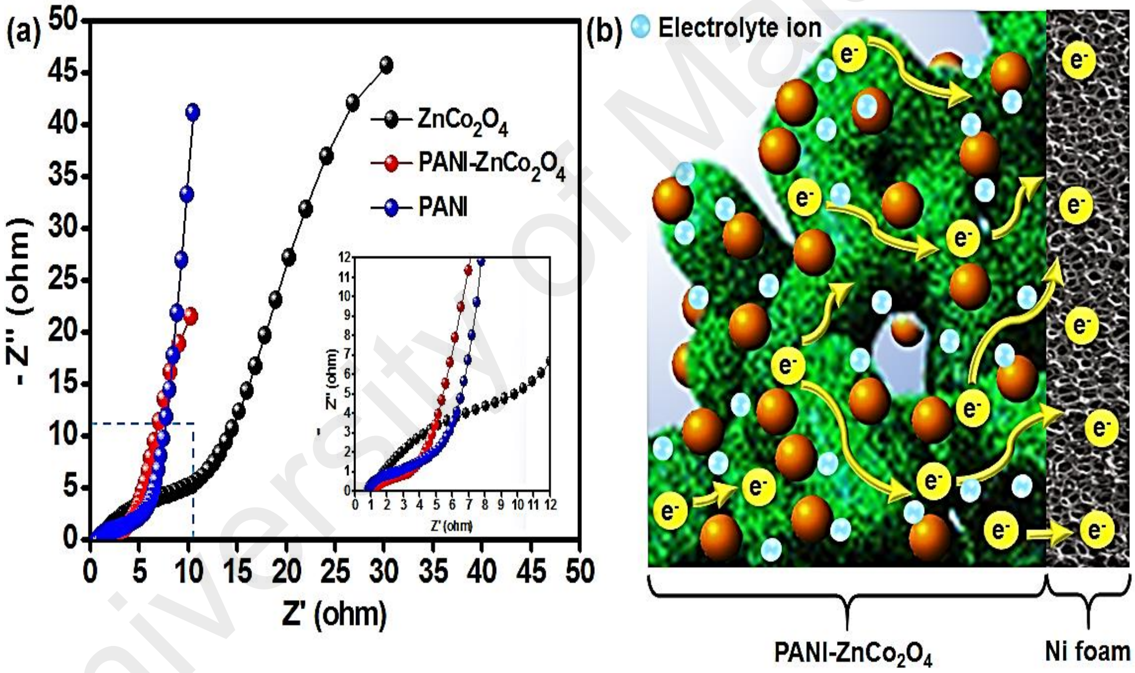

Figure 4.8: (a) Nyquist plots of $ZnCo_2O_4$, PANI and PANI-$ZnCo_2O_4$. Inset is the enlarged EIS spectra of $ZnCo_2O_4$, PANI and PANI-$ZnCo_2O_4$; (b) schematic illustration of surface reaction at PANI-$ZnCo_2O_4$ electrode.

The high specific capacity, low ESR value as well as small R_{ct} exhibited by PANI-$ZnCo_2O_4$ as compared to its counterparts can be proposed by the following aspects (illustrated in Figure 4.8(b));

(i) PANI achieved high specific capacity at lower current densities contributed from its semicrystalline (partially amorphous) structure which typically consists of many channels for the diffusion of electrolyte ions (Uchaker et al., 2014). However, some interior surfaces of PANI could not be accessed by the electrolyte ions at high current densities and renders to poor capacity retention (Gao et al., 2015). On the other hand, highly agglomeration of $ZnCo_2O_4$ nanoparticles reduced the effective surface area for the interaction with elecrolyte which causes to low specific capacity. When PANI is blended with $ZnCo_2O_4$, PANI augmented the effective surface area by preventing the agglomeration of $ZnCo_2O_4$ nanoparticles. Thus, more electron transfer can happen in PANI-$ZnCo_2O_4$. Moreover, the presence of $ZnCo_2O_4$ nanoparticles provided additional redox sites to the non-accessed surface area of PANI, retaining high specific capacity even at greater current densities (Omar et al., 2017).

(ii) $ZnCo_2O_4$ has low intrinsic electrical conductivity which impeded electron to migrate from one $ZnCo_2O_4$ particle to another particle quickly (Xu et al., 2016). Herein, the tubular shape of conductive PANI that support $ZnCo_2O_4$ nanoparticles provided the interconnected paths to facilitate the electron mobility continuously towards the current collector (Ni foam) and reduced the internal resistance of PANI-$ZnCo_2O_4$ (Maiti & Khatua, 2013); (iii) both pure PANI and $ZnCo_2O_4$ nanoparticles were simultaneously active in alkaline electrolyte. The redox reaction of $ZnCo_2O_4$ nanoparticles associated with alkaline electrolyte was corresponds to the reversible reaction of Zn^{2+}/Zn^{3+} and Co^{3+}/Co^{4+} transitions as shown at the following equations (Zhu et al., 2014):

$$ZnCo_2O_4 + OH^{-} + H_2O \leftrightarrow ZnOOH + 2CoOOH + e^{-} \qquad (4.1)$$

$$CoOOH + OH^{-} \leftrightarrow CoO_2 + H_2O + e^{-} \qquad (4.2)$$

While, the redox transitions of PANI corresponds to the transition between leucoemeraldine and emeraldine state of PANI (Liu et al., 2013). Thus, the physical blending of PANI and $ZnCo_2O_4$ nanoparticles give rise to a synergistic effect, thereby boosting the electrode performance (Chen et al., 2013).

4.2 System 2: Nickel phosphate ($Ni_3(PO_4)_2$)

In the first part of this project, $ZnCo_2O_4$ has been studied as a pristine and blended with PANI to form composite as electrode material. From the electrochemical studies, it is understood that the $ZnCo_2O_4$ based materials did not show promising results in terms of small potential window and low specific capacity. So, there is a need to replace more active material for electrochemical application. From the literature it is found that $Ni_3(PO_4)_2$ would be suitable candidate for this purpose. In this part and the following parts, the performance of $Ni_3(PO_4)_2$ has been evaluated by varying calcination temperature and incorporating $Ni_3(PO_4)_2$ with Ag_3PO_4 and PANI.

4.2.1 XRD

Figure 4.9 shows a progressive crystallization of as-prepared $Ni_3(PO_4)_2$ (N0) with the increase of the calcination temperature. Explicitly, N0, N300 and N600 showed broad peak between 28° and 40°, indicating that their amorphous structure persist up to 600 °C (Figure 4.9a). Two broad humps at 2θ value of 28° and 37° as observed at N0 is probably arised from the presence of organic units of ethylene glycol (Pramanik et al., 2016). This implies the incomplete reaction between ethylene glycol, disodium hydrogen phosphate and nickel acetate tetrahydrate at room temperature (Guo et al., 2013). N600 shows a relatively intensified peak as compared to N300, hinting that some crystalline phase in formed.

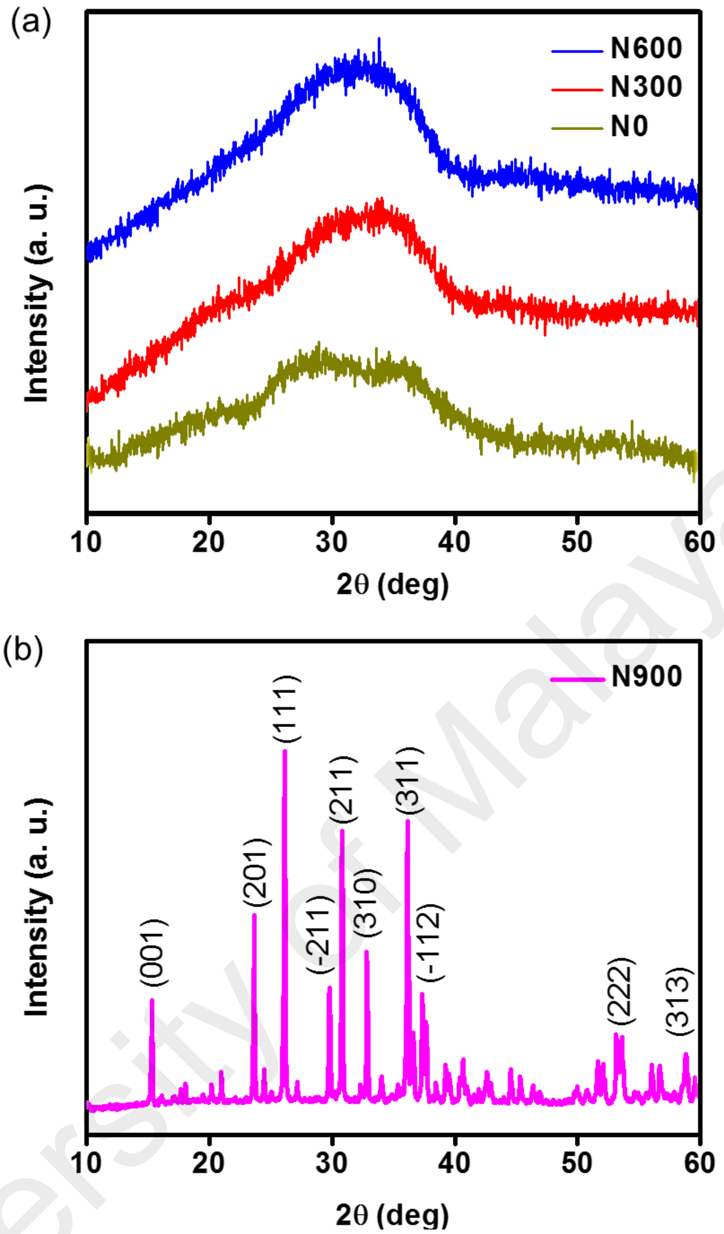

Figure 4.9: XRD diffractogram of (a) N0, N300, N600 and (b) N900.

The complete transformation from amorphous to crystalline was clearly observed after calcination at 900 °C, where N900 exhibited sharp diffraction peaks, revealing its highly crystalline structure (Figure 4.9b). The peaks at 2θ value of 15.2, 23.6°, 26.2°, 29.8°, 30.8°, 32.8° , 36.2°, 37.3°, 53.4°, and 58.8° as shown by N900 can be well indexed to the (001), (201), (111), (211), (211), (310), (311), (112), (222) and (313) planes of the monoclinic structure of nickel phosphate (JCPDS card no. 038-1473 with a space group of P21/1), respectively. This result signifies that the crystalline phase of $Ni_3(PO_4)_2$ can be obtained after calcined at high temperature.

4.2.2 FTIR

The FTIR spectra of N0, N300, N600 and N900 are shown in Figure 4.10. The PO_4 group, which can be seen in the spectrum of N900, can be split into three vibrational bands: triply degenerate asymmetrical bending mode of the O−P−O bond (ν_4 PO_4^{3-}) in the range of 520-640 cm^{-1}, triply degenerate asymmetrical stretching mode of the P−O bond (ν_3 PO_4^{3-}) in the range of 850-960 cm^{-1} and symmetric stretching modes of PO_4^{3-} ion around 1068 cm^{-1}. However, these bands became broader and could not be distinguished in the spectrum of N0, N300 and N600. This is due to the relative disorder of the molecules in the amorphous structure which results in a wider distribution of bond lengths and energies with respect to the crystalline structure as displayed by N900 (Combes & Rey, 2010). A weak band at 765 cm^{-1} was assigned to the stretching of P−O−P linkages (Julien, 2004). On the other hand, the band around 1635 cm^{-1} and 3000-3700 cm^{-1} belong to $\nu_1(A_1)H_2O$ and $\nu_2(A_1)H_2O$, respectively (Cimdina & Borodajenko, 2012). The intensity of these bands were weakened with the increase of calcination temperature, signifying the adsorbed water molecules are gradually reduced after being subjected to increased calcination temperatures. The water contain is favourable in supercapacitor as it can alter the ionic mobility pathways that is coming from electrolyte. Thus, the obtained XRD and FTIR results adequate to confirm that the increasing in calcination temperature leads to the transition from amorphorcity to crystallinity structure of particles, particle aggregation and the removal water molecules.

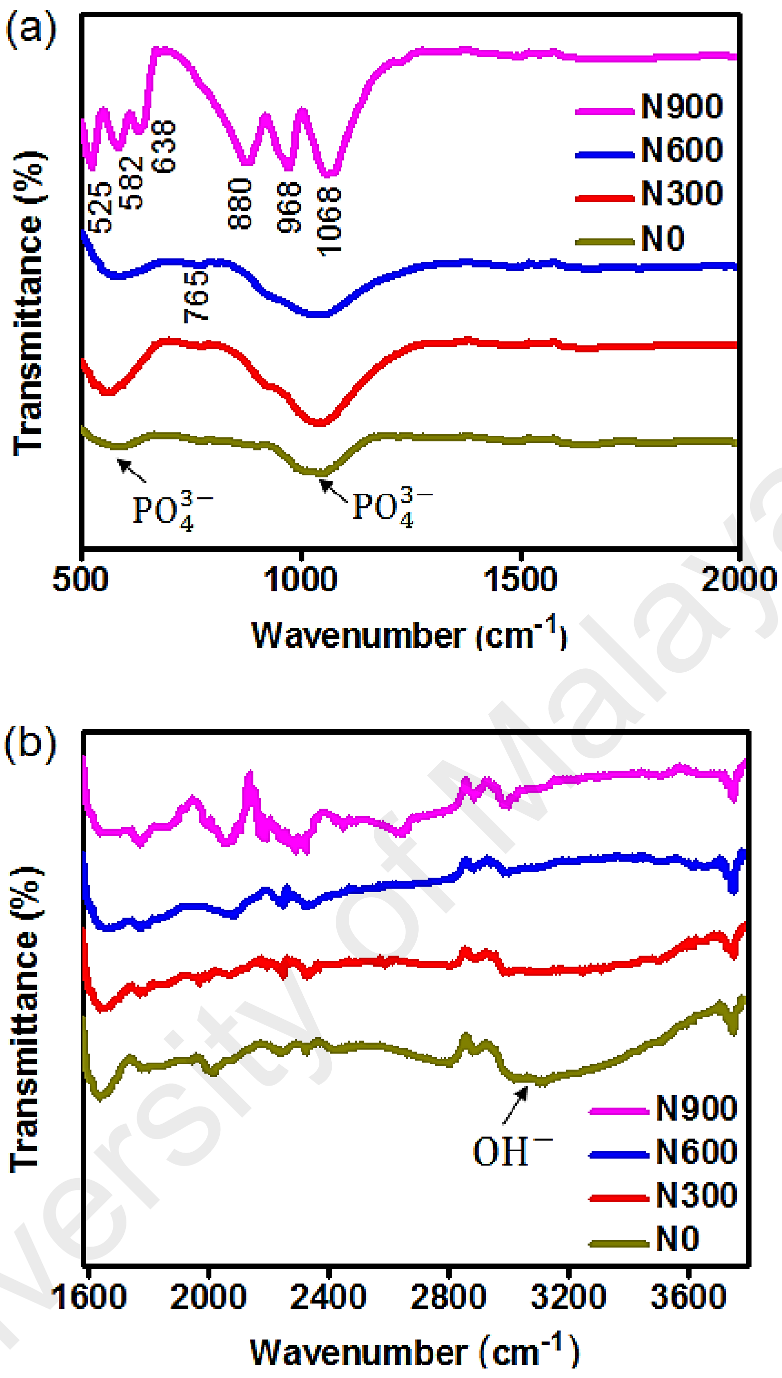

Figure 4.10: FTIR pattern of N0, N300, N600 and N900 at the wavenumber range of (a) 500-2000 cm^{-1} and (b) 1580-4000 cm^{-1}.

4.2.3 FESEM

FESEM images shown in Figure 4.11, Figure 4.12, Figure 4.13 and Figure 4.14 revealed that after calcination, the particle size increases with elevating calcination temperature. Before calcination (referring to N0), the particles were not well separated with high degree of agglomeration caused by the dominant effect of weak Van der Waal forces (Valsylkiv, 2010). By considering to the XRD diffractogram obtained for N0, the formation of N0 particle agglomeration can also be ascribed to the incomplete reaction between ethylene glycol, disodium hydrogen phosphate and nickel acetate tetrahydrate. After calcination at 300 °C (referring to N300), the particles were less agglomerated with an average size of particles of 110 nm (which is slightly smaller than the size of N0 particles). The slight reduction of particle size is due to the removal of some of the adsorbed ethylene glycol and water content after heated at 300 °C (Poncelet et al., 1995). As the calcination temperature was increased to 600 °C (N600), the particles began to interact with each other. The occurrence of inter-particle necking was observed and the particle size became larger than N300 with an average size of 150 nm (Figure 4.13 (inset)). Further raise in calcination temperature (900 °C) subsequently led to the particle aggregation. The particles grew dramatically with an average size of 3 µm (Figure 4.14 (inset)) and were tightly combined forming large non-porous, solid particles.

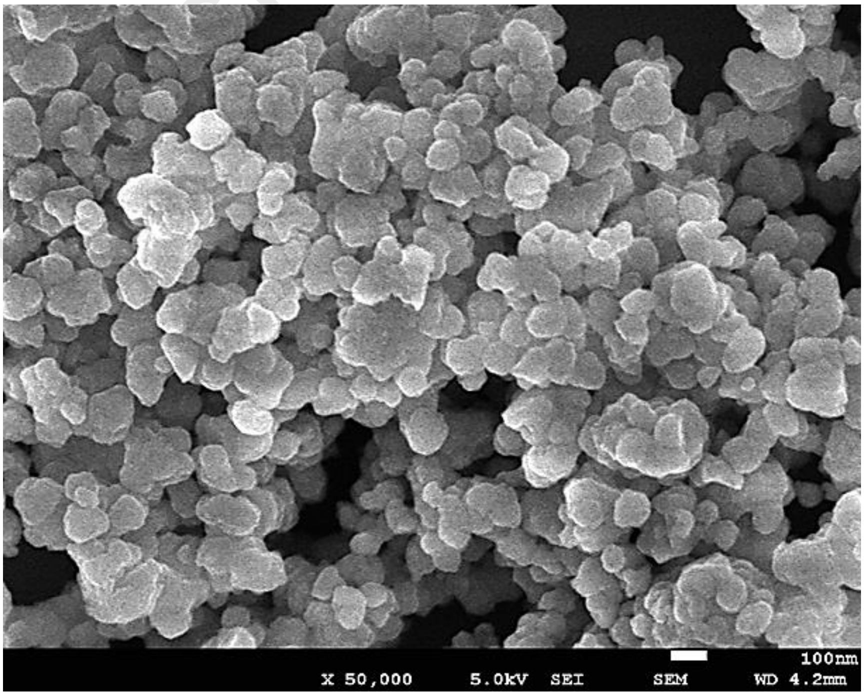

Figure 4.11: FESEM image of N0.

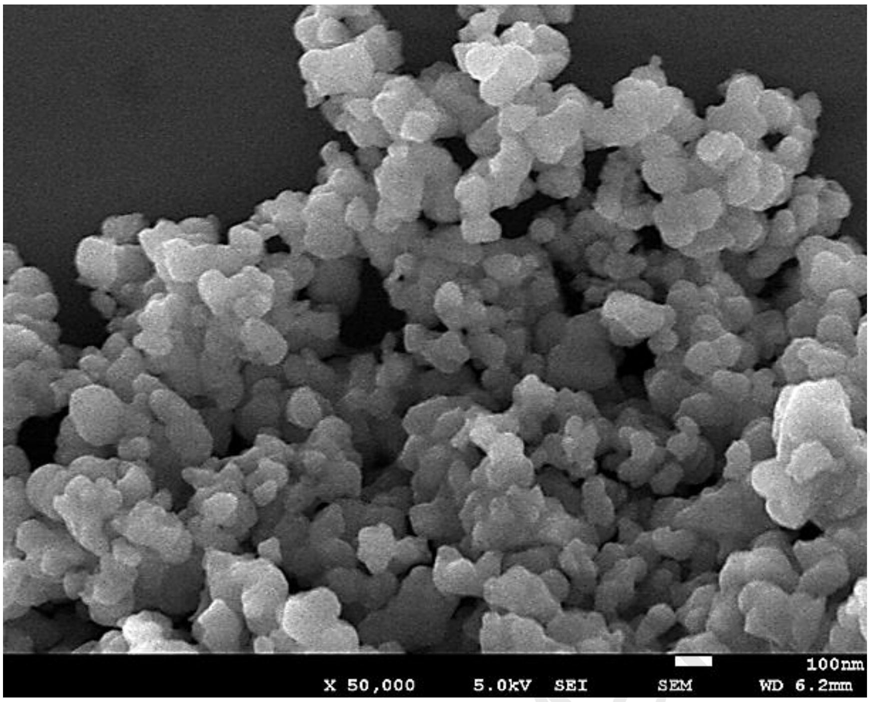

Figure 4.12: FESEM image of N300.

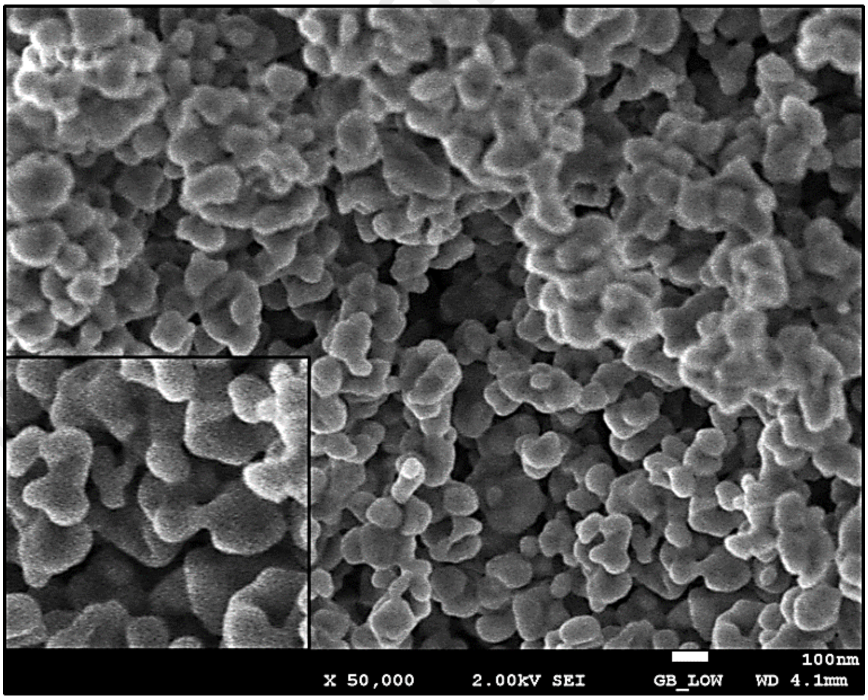

Figure 4.13: FESEM image of N600.

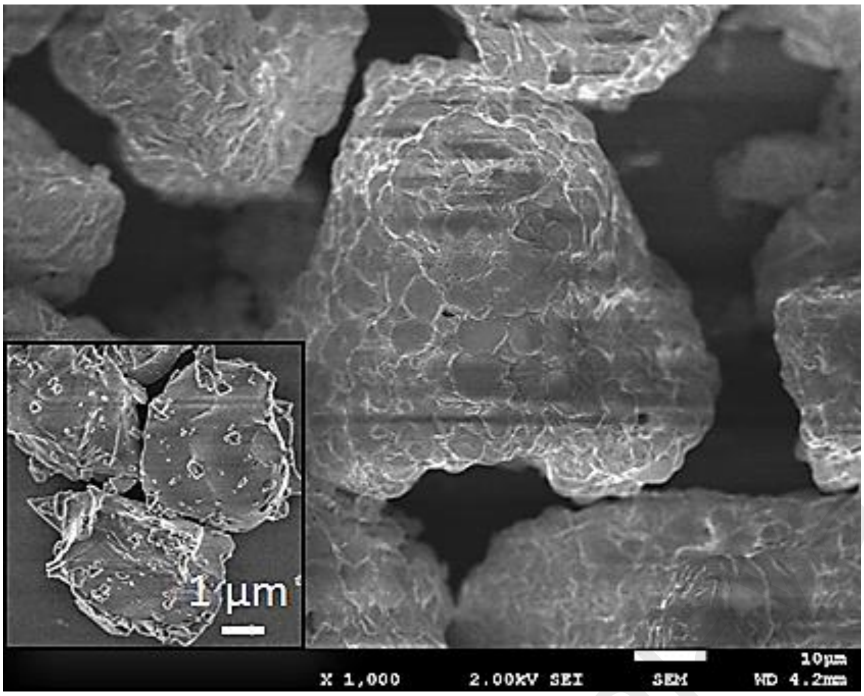

Figure 4.14: FESEM image of N900.

The slow transition from amorphous to crystalline phase in the early stage of calcination is related to the presence of water molecules (which is confirmed by FTIR results) that prevent rapid growth of crystals. The formation of particle aggregation shown by N900 can be ascribed to the rapid increase in crystal growth with increasing in calcination temperature. Evidently, the high calcination temperature promotes enlargement of grain boundaries and particle size. The mechanism of particle growth was illustrated in Figure 4.15.

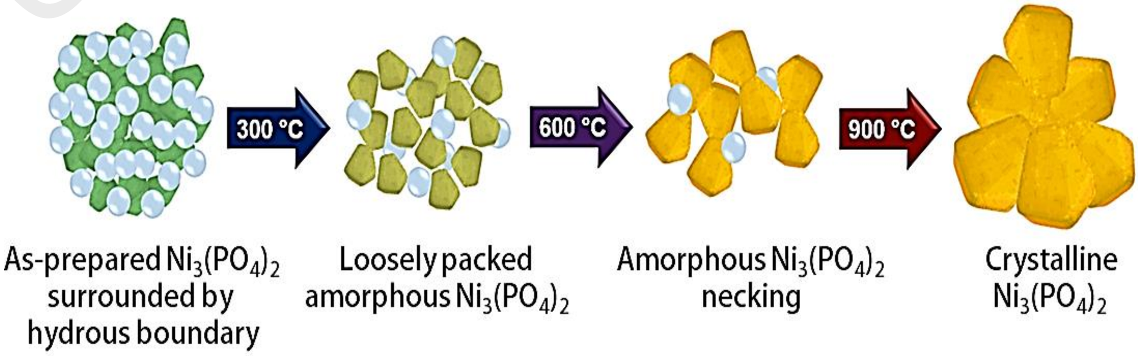

Figure 4.15: Illustration of the growth of N0, N300, N600 and N900.

4.2.4 Electrochemical studies (Three-electrode cell)

4.2.4.1 CV

The electrochemical performance of N300, N600 and N900 electrodes was firstly analysed using CV in a potential range of 0.0 - 0.5 V in 1 M KOH. Figure 4.16a-c showed the CV curves of all electrodes with various scan rates (1 - 100 mV/s). A pair of strong anodic (oxidation) and cathodic (reduction) peaks can be seen at all scan rates for N300, N600 and N900 electrodes indicates that the interaction between OH^- ion and electrode materials was not only happened at the surface, but also within the electrode materials. This ion diffusion mechanism is the characteristic of battery-type materials (Brousse & Daniel, 2015). The possible faradaic reaction for $Ni_3(PO_4)_2$ in 1 M KOH medium is based on the equation 4.3.

$$Ni_3(PO_4)_2 + OH^- \leftrightarrow Ni_3(OH)(PO_4)_2 + e^- \qquad (4.3)$$

During oxidation process, $Ni_3(PO_4)_2$ was transformed to $Ni_3(OH)(PO_4)_2$ by releasing electron. The maximum electron released in the electrochemical cell can be correlated with the maximum point of anodic peak which can be observed in the CV graph. During reduction process (reverse scan), $Ni_3(OH)(PO_4)_2$ transformed back to its original form (i.e. $Ni_3(PO_4)_2$) by accepting the electrons. The maximum point of cathodic peak indicates the highest number of $Ni_3(OH)(PO_4)_2$ being reduced (Duraisamy et al., 2015). The decayed cathodic curve back to the initial point of CV curve means all $Ni_3(OH)(PO_4)_2$ molecules have been depleted at the electrode surface (i.e. Ni foam substrate) due to all molecules have been reduced to $Ni_3(PO_4)_2$.

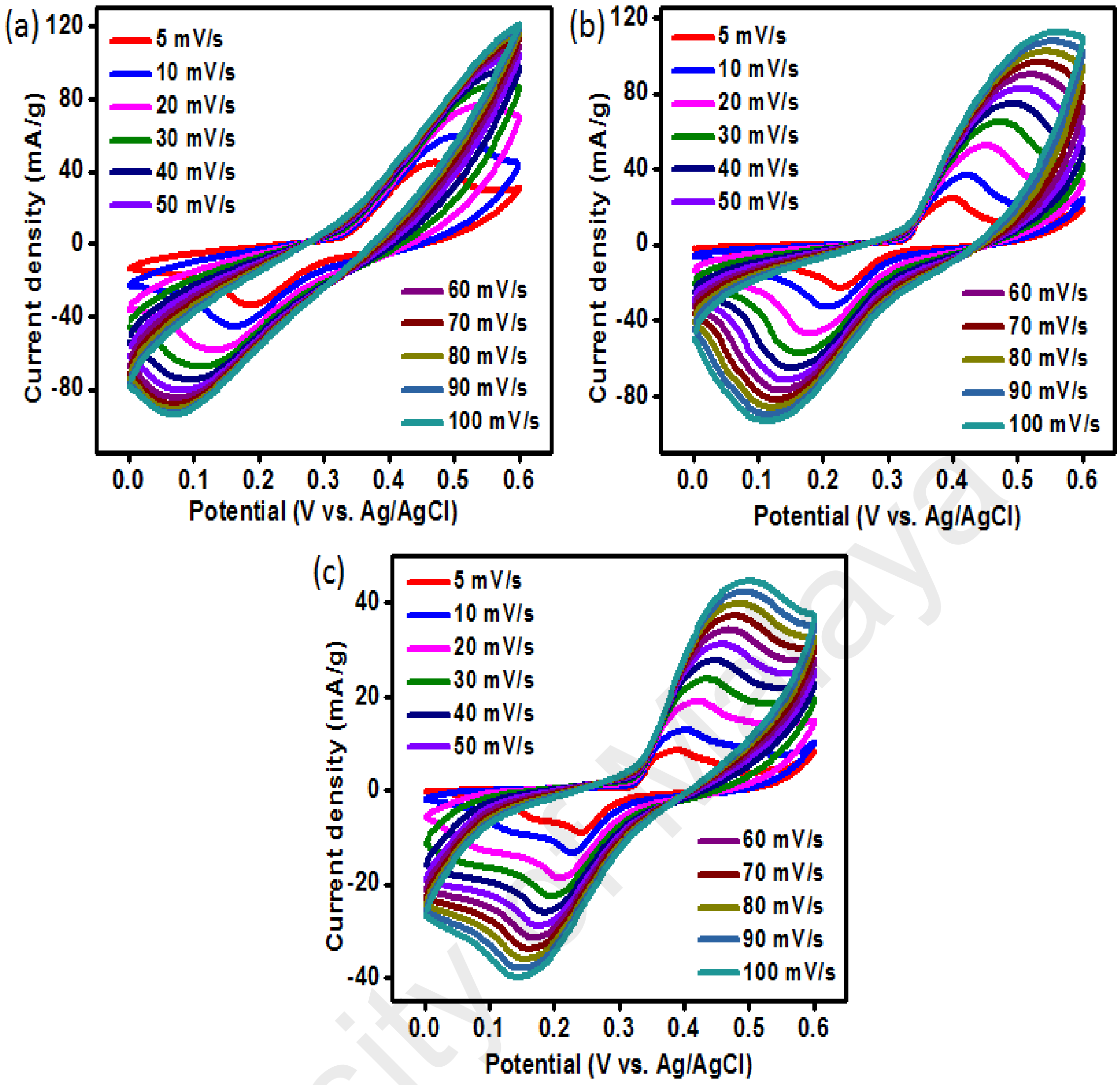

Figure 4.16: CV curves of (a) N300, (b) N600 (c) N900 at the scan rates of 5 - 100 mV/s.

It was observed that the voltammetric currents were augmented with scan rates and the anodic and cathodic peaks shifted towards higher and lower potentials, respectively. This corresponds to the kinetic irreversibility of electrolyte ions within the electrode materials that typically occurs with an augmenting in scan rates (Umeshbabu et al., 2015). Figure 4.17 compares the CV curves between N300, N600 and N900 electrodes at a fixed scan rate of 5 mV/s. Among the three electrodes, N300 exhibited the largest integrated area, suggesting that it has the highest charge storage capacity (Hu et al., 2016). The calculated specific capacity of N300, N600 and N900 at the scan rate of 5 mV/s was 627.5, 337.0 and 134.2 C/g, respectively.

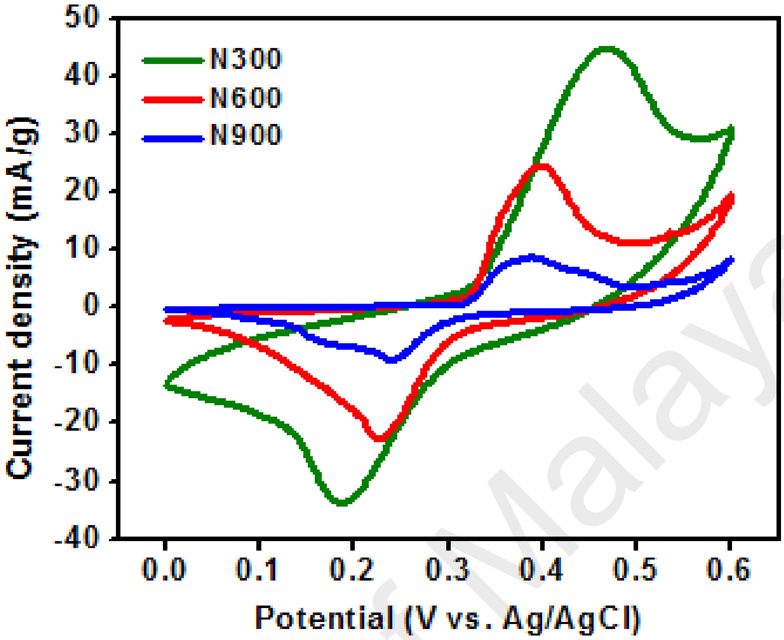

Figure 4.17: CV of N300, N600 and N900 at the scan rate of 5 mV/s.

4.2.4.2 GCD

The electrochemical performance of the N300, N600 and N900 electrodes were further assessed via GCD technique. Figure 4.18 represents the charge-discharge curves of the electrodes at the current density of 1 - 8 A/g in the potential range of 0 - 4.6 V. An obvious plateau pattern was observed in every curves associated to the faradaic behaviour of all electrodes as in agreement with the CV results (Gu et al., 2015). With increasing the current density, the discharge time was decreased due to the fact that the specific capacity value was inversely proportional to the current densities. This can be explained by the time constraints for OH^- diffusion through the electrode material at high current density. While at low current density, the OH^- have enough time to access the electrode material and able to interact with whole electroactive sites of the material. The results showed that N300 had a longer discharge time than the other electrodes at all current densities, indicating its highest specific capacity (Jahromi et al., 2015).

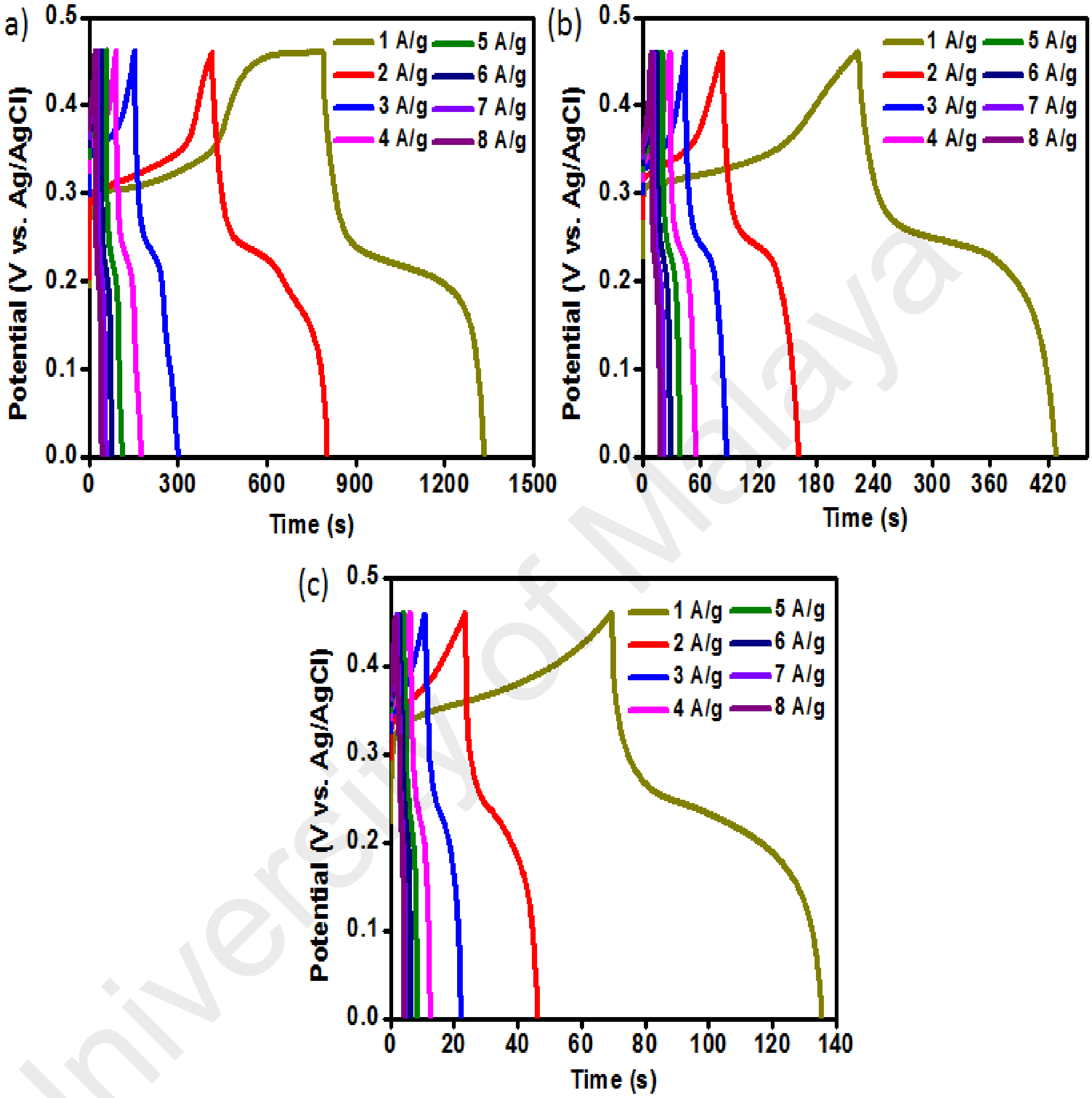

Figure 4.18: GCD curves of (a) N300, (b) N600 and c) N900.

The calculated specific capacity for all electrodes based on GCD results were plotted in Figure 4.19. The maximum specific capacity for N300, N600 and N900 was determined to be 539, 202.5 and 66 C/g. The specific capacities of N300 were higher than those of N600 and N900 at all current densities which is attributed to the smaller size of particles. Small size of particles can provide more redox sites for the interaction with electrolyte ions as compared to the larger size of particles. Whereas N900 exhibited the lowest specific capacities as compared to other electrodes due to its significant large particle size which greatly limit the interfacial contact area between the electrode material and electrolyte. Thus, the number of redox reaction happened at N900 was far reduced as compared to its counterparts.

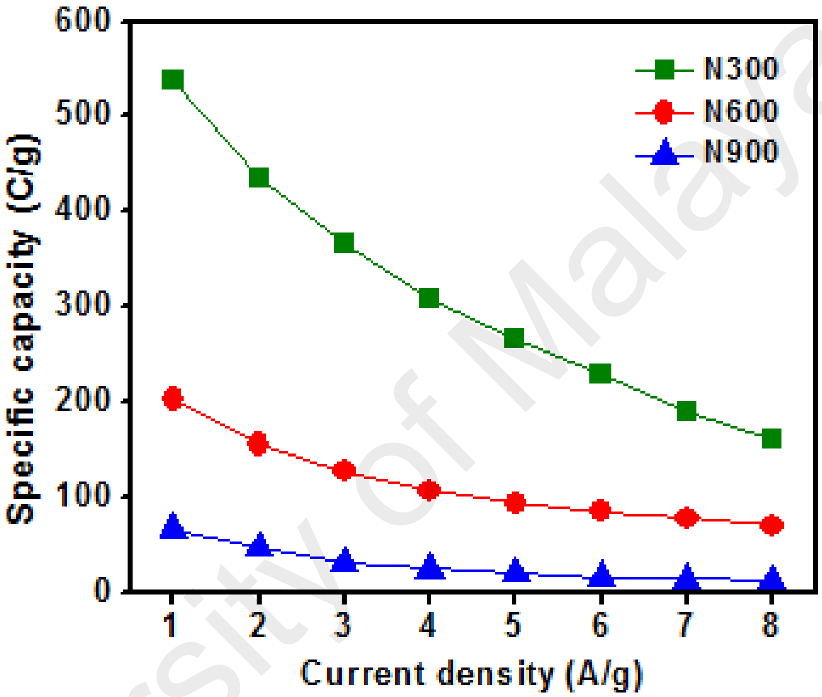

Figure 4.19: Specific capacity of N300, N600 and N900 electrodes at the current density of 1 - 8 A/g.

4.2.4.3 EIS

The EIS analysis is important to understand the charge and ion transport behaviour of the N300, N600 and N900 electrodes (Figure 4.20). The ESR value of N300, N600 and N900 was 1.17, 1.76 and 2.09 Ω, respectively, as shown in the Figure 4.20 (inset). The smallest ESR value of N300 indicates its highest electrical conductivity as in agreement with high specific capacity obtained from CV and GCD results. In addition, the diameter of semicircle (R_{ct}) of N300 is smaller than that of N600 and N900, typifying its lower charge transfer resistance. As compared to N600 and N900, the Warburg impedance (W_d) deduced by the straight line of N300 is the most vertical parallel to the imaginary axis which insinuated its low ion diffusion resistance and highest capacitive behaviour.

Therefore, by considering the results obtained from XRD, FTIR, FESEM and electrochemical studies (CV, GCD and EIS), the distinct in specific capacity values achieved by N300, N600 and N900 are attributed to several factors;

(i) N300 has smaller particle size than N600 and N900. Thus, N300 has larger effective surface area which leads to the augmentation of electroactive sites for OH^- interaction to initiate the redox process. While the lower values in specific capacity shown by N600 and N900 is because of the reduced in redox sites caused by the growth of particle size (Liu et al., 2015). As the particle size increases with calcination temperature, the surface to volume ratio decreases and consequently the specific capacity decreased.

(ii) the amorphous structure of N300 brings more transportation channels for OH^- diffusion than crystalline structure due to its high structural disorder. Generally, disordered structure of amorphous materials form abundance active channels for effective electrolyte ions penetration. Whereas, for crystalline structure, some of the electrolyte ions was incapable to penetrate into the lattice. The ions were mostly interacted with the outermost surface layer of the particle, hence, limited the contact between the electrode material and electrolyte.

(iii) the presence of adsorbed water in the amorphous structure material may also be the driving difference in electrochemical performance. The presence of water molecules tuned the ionic transport pathways by expanding the inter-particle distance, thus delivering enhanced specific capacity (Halliburton et al., 2005; Uchaker et al., 2014).

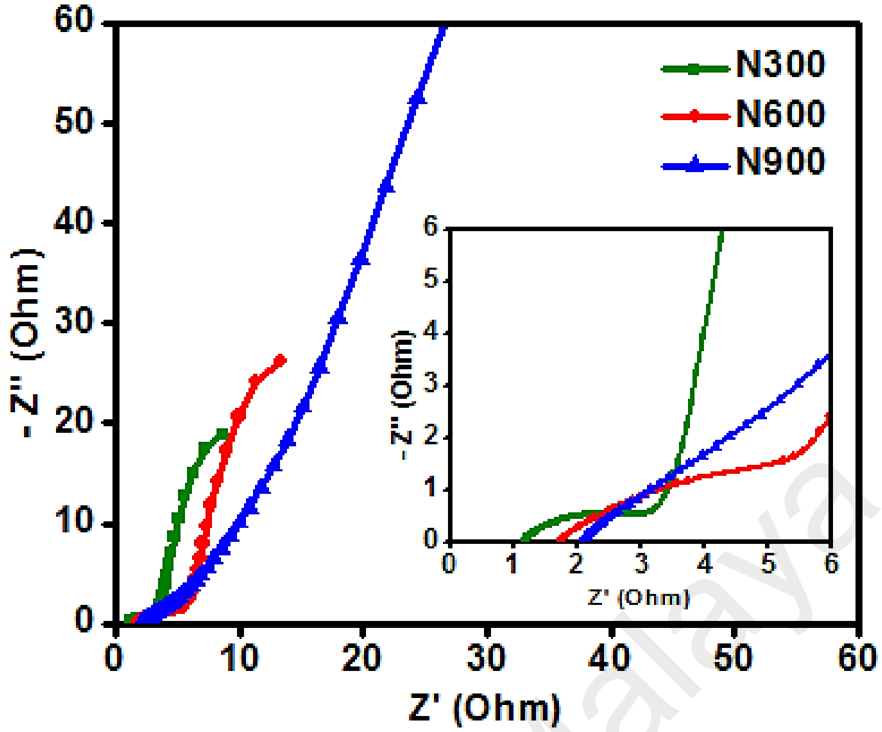

Figure 4.20: Nyquist plot of N300, N600 and N900.

4.2.5 Electrochemical studies (Two-electrode cell)

For supercapattery evaluation, N300 was chosen as the positive electrode (due to its highest specific capacity at all current densities calculated from three-electrode studies) and activated carbon (AC) as the negative electrode. The electrodes were immersed in 1 M KOH electrolyte and the cell is denoted as N300//AC. Prior to the fabrication of supercapattery, CVs of the single electrodes (i.e. AC and N300) were recorded to estimate the maximum working potential window of the supercapattery (Figure 4.21(a)). The CV for AC electrode was scanned from 0 to -1V and for N300 electrode from 0 to 0.6 V. As expected, the stable potential window of the supercapattery can be extended to 1.6 V as shown in Figure 4.21(b). No anodic or cathodic peak was observed from 0.0 to 0.4 V, signifying the capacity was contributed from capacitive-behavior of AC. When the potential is extended to 0.8 V, redox peaks appeared which manifests the capacity was contributed from the faradaic reaction of N300. From 0.0 to 1.6 V, the supercapattery exhibited almost rectangular shape with the additional of broad peaks attributed to the involvement of the capacitive reaction of AC and faradaic reaction of N300 electrode during energy storage process.

Figure 4.21(c) displayed the CV curves of N300//AC at different scan rates. The shape of the CV curves was well maintained from lower scan rate of 5 mV/s to higher scan rate of 100 mV/s which demonstrates that the device exhibited capacitive behaviour within this range of scan rate. The GCD curves of N300//AC at different current densities are presented in Figure 4.21(d). The measurement was taken in the same range of potential window (0 - 1.6 V) under the current density of 1 - 8 A/g. The non-linear of GCD curves was due to the influence of faradaic reaction of the N300 during energy storage process, which is different from the sharply triangular GCD curve of EDLC. The device did not show any plateau curve as observed in single electrode measurement as presented in Section 4.2.4.2 because of the presence of capacitive behaviour of AC electrode in the device. This means that the energy storage through electrostatic and faradaic mechanism were took place simultaneously at both capacitive and battery-type electrodes (Boruah & Misra, 2016). The resulted GCD pattern shown in the figure demonstrates that the energy storage mechanism of supercapattery is not the same with typical EDLCs (linear curve) and batteries (plateau curve).

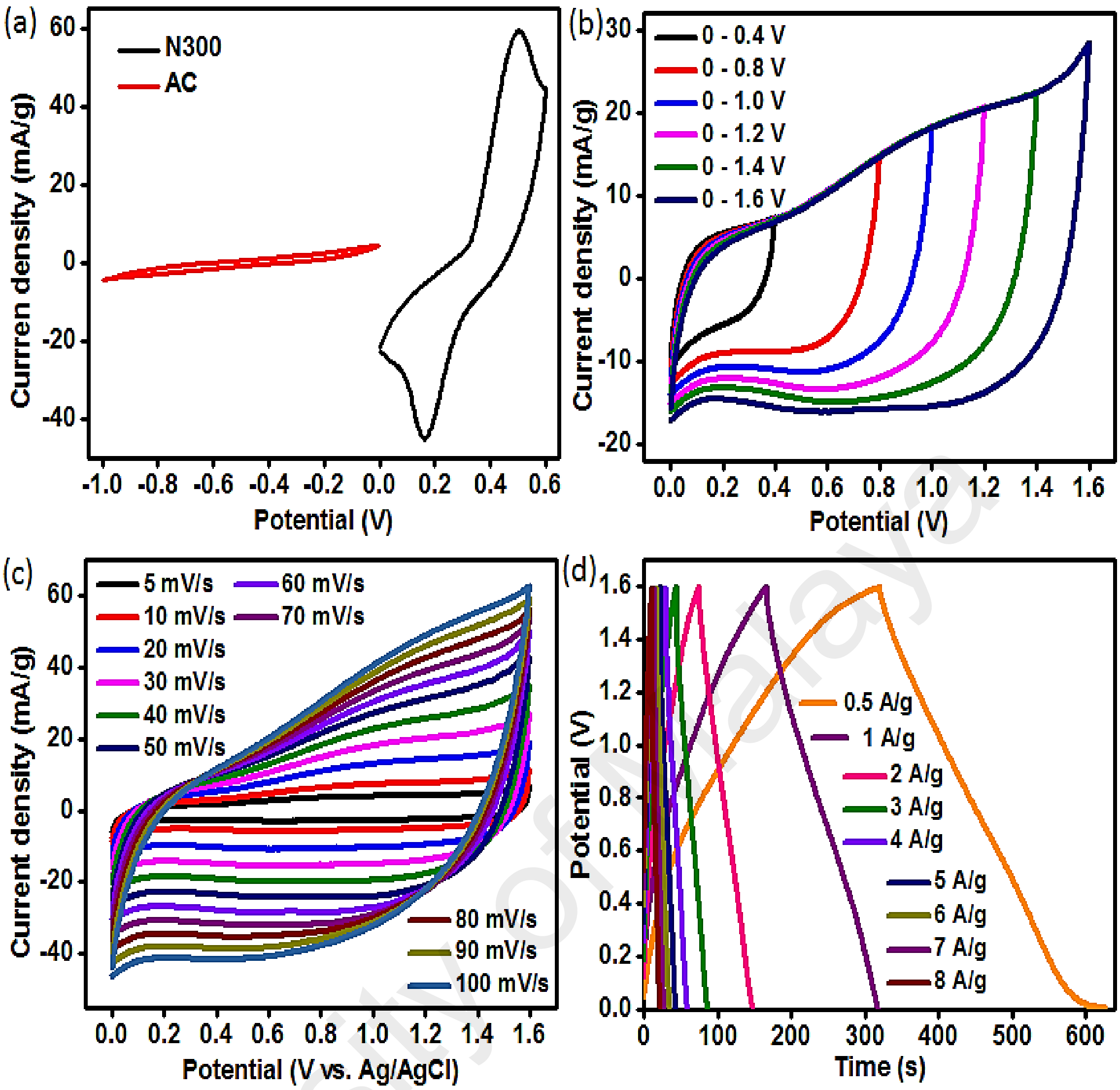

Figure 4.21: (a) Comparative CV curves of N300 (positive electrode) and AC (negative electrode) at a scan rate of 10 mV/s in a three-electrode cell; (b) N300//AC at different potential windows with the scan rate of 30 mV/s; (c) CV curves of N300//AC measured at different scan rates; (d) GCD curves of N300//AC at different current densities.

The calculated specific capacity based on GCD as shown in Figure 4.22(a) was 150 C/g at 0.5 A/g. The specific capacity retained to 37 % when the current density increased from 0.5 to 8 A/g. Since the cyclic stability is another substantial parameter to evaluate the efficiency of supercapattery for practical application, N300//AC was subjected to 3000 continuous cycles of charge and discharge at 1 A/g. The capacity retention of N300//AC as a function of cycle number was exhibited in Figure 4.22(b). Noticeably, the specific capacity was increased up to 108 % for the first 400 cycles, which was due to the progressive activation process of the cell. Then, the capacity retention was slowly decreased until 2000th cycle which indicated that it reached its stability. Finally, the capacity retention was gradually degraded to 75 % at 3000th cycle. The decay in capacity retention is attributed to the occurring of repeated structural expansion and contraction of the electrode materials during charge and discharge cycles. This commonly lead to aggregation of particles and as consequence, the electrode materials were detached from the electrode substrate and mixed with bulk electrolyte.

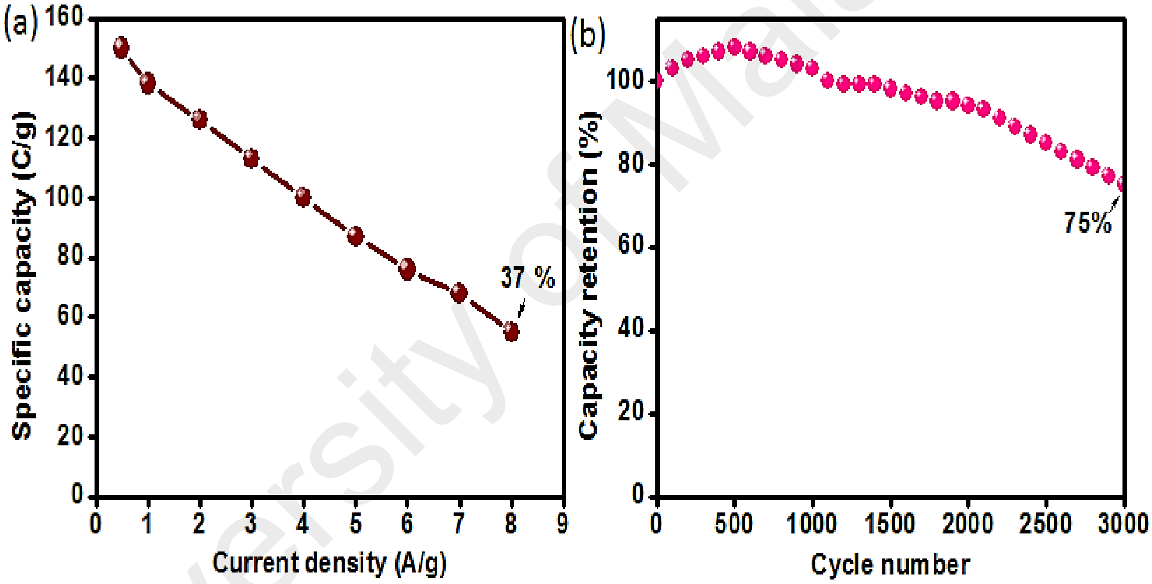

Figure 4.22: Specific capacity of N300//AC versus current densities; (b) cycling stability of N300//AC.

In overall, N300 exhibited high specific capacity due to its plenty channels which can shorten the length of electrolyte ion diffusion. Nonetheless, its capability to store energy is dropped significantly with increasing current densities mainly due to its low electrical conductivity. Thus, we decided to mix N300 with other metal ions (Ag^+) to boost the properties of N300 and the improvement in the electrochemical performance was demonstrated in System 3.

4.3 System 3: Nickel phosphate-silver phosphate nanocomposite ($Ni_3(PO_4)_2$-Ag_3PO_4)

4.3.1 XRD

The crystallinity of N300, 0.05 NAg, 0.1 NAg, 0.2 NAg and 0.3 NAg were determined by XRD as shown in Figure 4.23. As comparison with N300 which was showing one broad peak attributable to its amorphous nature, a series of diffraction peaks can be seen for 0.05 NAg, 0.1 NAg and 0.2 NAg. The peaks at 2θ of 29.1°, 33.3°, 36.6°, 47.5°, 52.1°, 55.0° and 57.5° correspond to the (200), (210), (211), (310), (222), (320) and (321) reflections of the body-centered cubic-phase of Ag_3PO_4 (JCPDS, 06-0505) with a space group of P4-3n24.

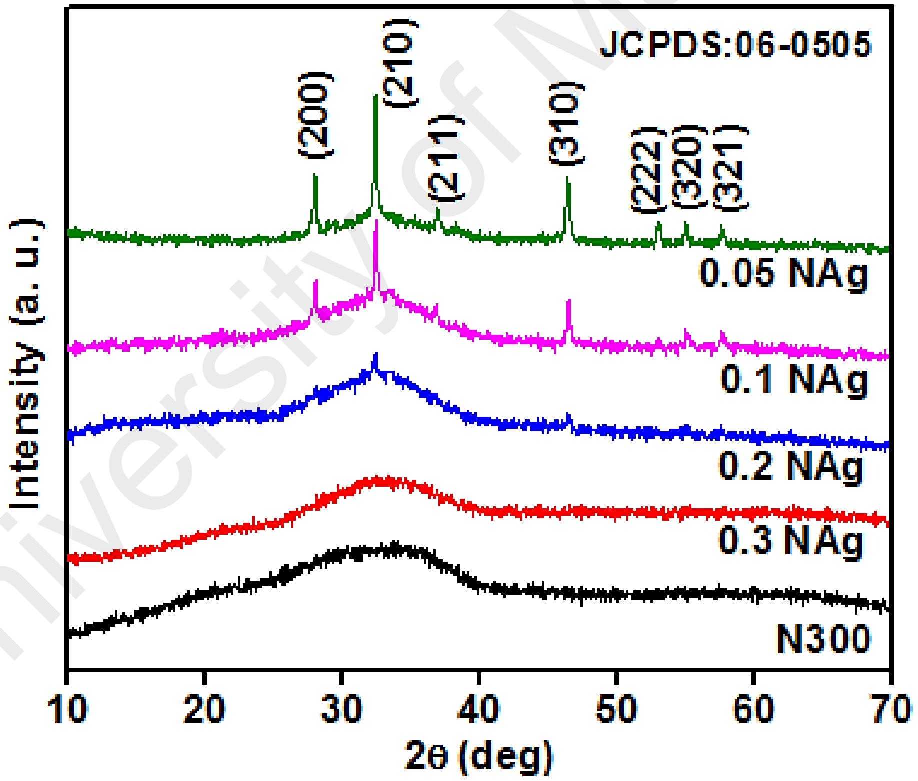

Figure 4.23: XRD diffractogram of 0.05 NAg, 0.1 NAg, 0.2 NAg and 0.3 NAg.

For all nanocoposites, the intensity of Ag_3PO_4 reflections increased with the decreasing amount of N300, indicating that Ag_3PO_4 particles are dominant in the nanocomposites. However, the cyrstalline reflections of Ag_3PO_4 at 0.3 NAg is difficult to be detected which might be due to the amount of Ag_3PO_4 is too low in this nanocomposite. No positional change of Ag_3PO_4 peaks was observed which suggesting that Ag_3PO_4 particles were not incorporated into the lattice of N300, but rather deposited on its surface (Michael et al., 2014).

4.3.2 FTIR

FTIR spectroscopy of N300, 0.05 NAg, 0.1 NAg, 0.2 NAg and 0.3 NAg are drawn in Figure 4.24(a) and Figure 4.24(b) to investigate the functional groups of the materials. For all samples, the transmittance band at 563 and 1036 cm^{-1} correspond to the presence of phosphate ($PO_4{}^3$) group as explained in the previous system. As compared to N300, those bands were shifted to lower wavenumber which inferred to the interaction at the molecular level is created between $Ni_3(PO_4)_2$ and Ag_3PO_4 (Benedek et al., 2017). During the mixing of N0 and $\mathrm{Ag(NH_3)_2^+}$ through sonochemical process, the positively charged $\mathrm{Ag(NH_3)_2^+}$ was attracted towards the negatively charged N0 particles through electrostatic interaction and were placed in the surrounding N0 (the synthesis mechanism was demostrated in Chapter 3). While the band around 1642 cm^{-1} and 3000-3700 cm^{-1} belong to $\nu_1(A_1)H_2O$ and $\nu_2(A_1)H_2O$, respectively. The intensity of all bands was increased after the incorporation of Ag_3PO_4 (0.05 NAg, 0.1 NAg, 0.2 NAg and 0.3 NAg), manisfesting that more phosphate groups and water crystals were chemisorbed on the surface of the $Ni_3(PO_4)_2$-Ag_3PO_4 (Yaning et al., 2016). As mentioned in the prevous system, the presence of adsorbed water may help to improve the electrochemical performance by expanding the interparticle distance, which correspondingly could tune the ionic transport pathways (Uchaker et al., 2014; Zheng et al., 2002). These results confirmed the effective combination of Ag_3PO_4 nanoparticles with amorphous $Ni_3(PO_4)_2$ which is in consistent with the XRD results.

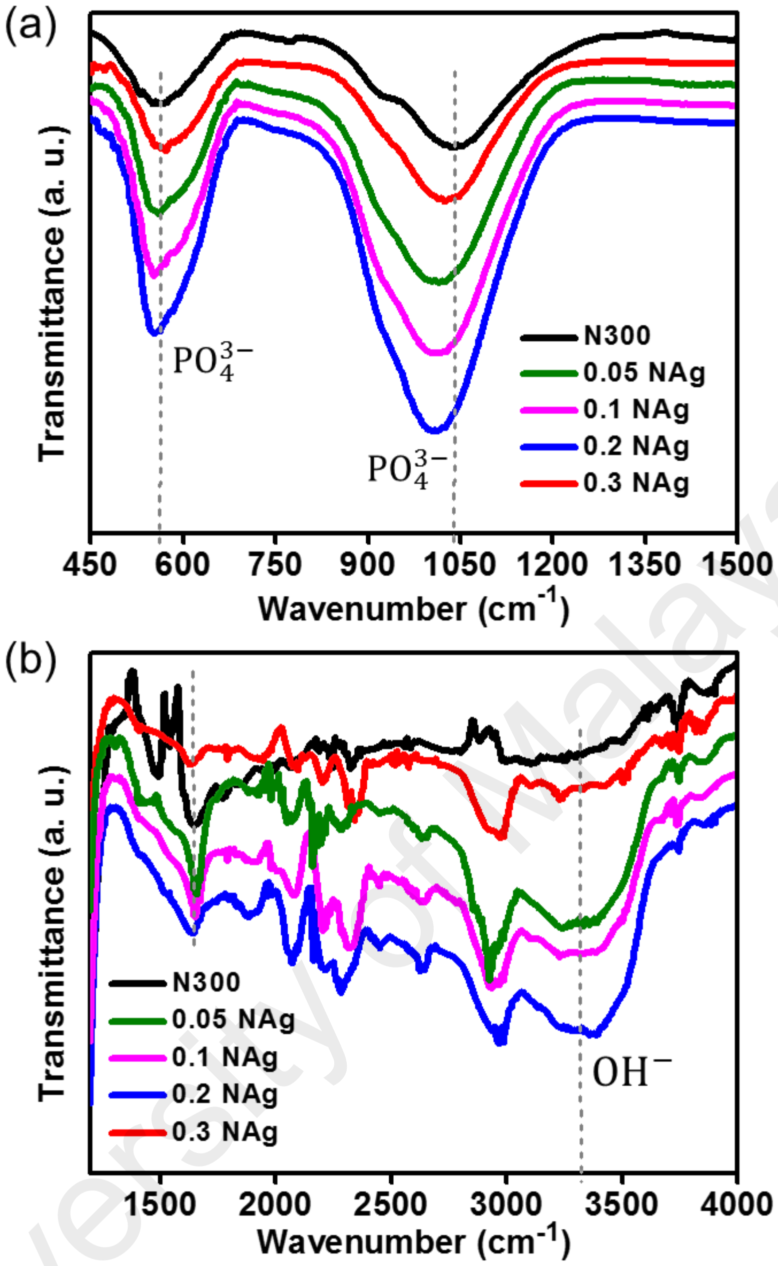

Figure 4.24: FTIR patterns of 0.05 NAg, 0.1 NAg, 0.2 NAg and 0.3 NAg at (a) 450 - 1500 cm^{-1} (b) 1200 - 4000 cm^{-1}.

4.3.3 XPS

The surface elemental composition and chemical bonding of N300 (from System 2) and 0.1 NAg are analysed and compared by XPS (Figure 4.25). (0.1 NAg was selected for XPS due to its best electrochemical performance among all $Ni_3(PO_4)_2$-Ag_3PO_4 (NAg) nanocomposites (will be discussed later)). The survey XPS spectra of both N300 and 0.1

NAg displayed several sharp peaks which autheticated the existence of Ni, O, P and Ag (for 0.1 NAg) (Figure 4.25(a)). 0.1 NAg exhibits the existence of the spin-orbit components that are separated by 6 eV; Ag 3d$_{5/2}$ (368.3 eV) and Ag 3d$_{3/2}$ (374.3 eV), corresponding to Ag^{+} of Ag_3PO_4 in 0.1 NAg (Figure 4.25(b)) (Kumar et al., 2016). Figure 4.25(c) displays the deconvoluted spectrum of Ni 2p which involves two peaks contributed from the spin-orbital splitting (with the gap of 17.9 eV) of Ni 2p$_{3/2}$ and Ni 2p$_{1/2}$, respectively. The two shakeup stellite peaks of nickel (denoted as Sat. 1 and Sat. 2) is caused by the ejection of core electron by a photoionization. The peak centered at ~857.1 eV for Ni 2p$_{3/2}$ can be assigned to Ni^{2+} interacting possibly with phosphate ion. Moreover, as compared to N300, the intensity of the Ni 2p for 0.1 NAg was weakened. This corraborates that the reduction of $Ni_3(PO_4)_2$ content after to the presence of Ag_3PO_4. While for the P 2p profiles presented in Figure 4.25(d) can be fitted into P 2p$_{1/2}$ (132.7 eV) and P 2p$_{3/2}$ (133.4 eV). The main deconvoluted peak of P 2p$_{3/2}$ constitutes 80-85 % of total area P 2p signal for both $Ni_3(PO_4)_2$ and 0.1 NAg. This can be imputed to metal phosphate species attributed to the oxidation of the $Ni_3(PO_4)_2$ (Yun et al., 2017). Apparently, after the incorporation of Ag, the Ni 2p and P 2p peaks were shifted to the higher E_B (~1.3 eV), demostrating the electronic structure of $Ni_3(PO_4)_2$ was affected by the electron transfer from $Ni_3(PO_4)_2$ to Ag_3PO_4 (Dutta & Datta, 2014).

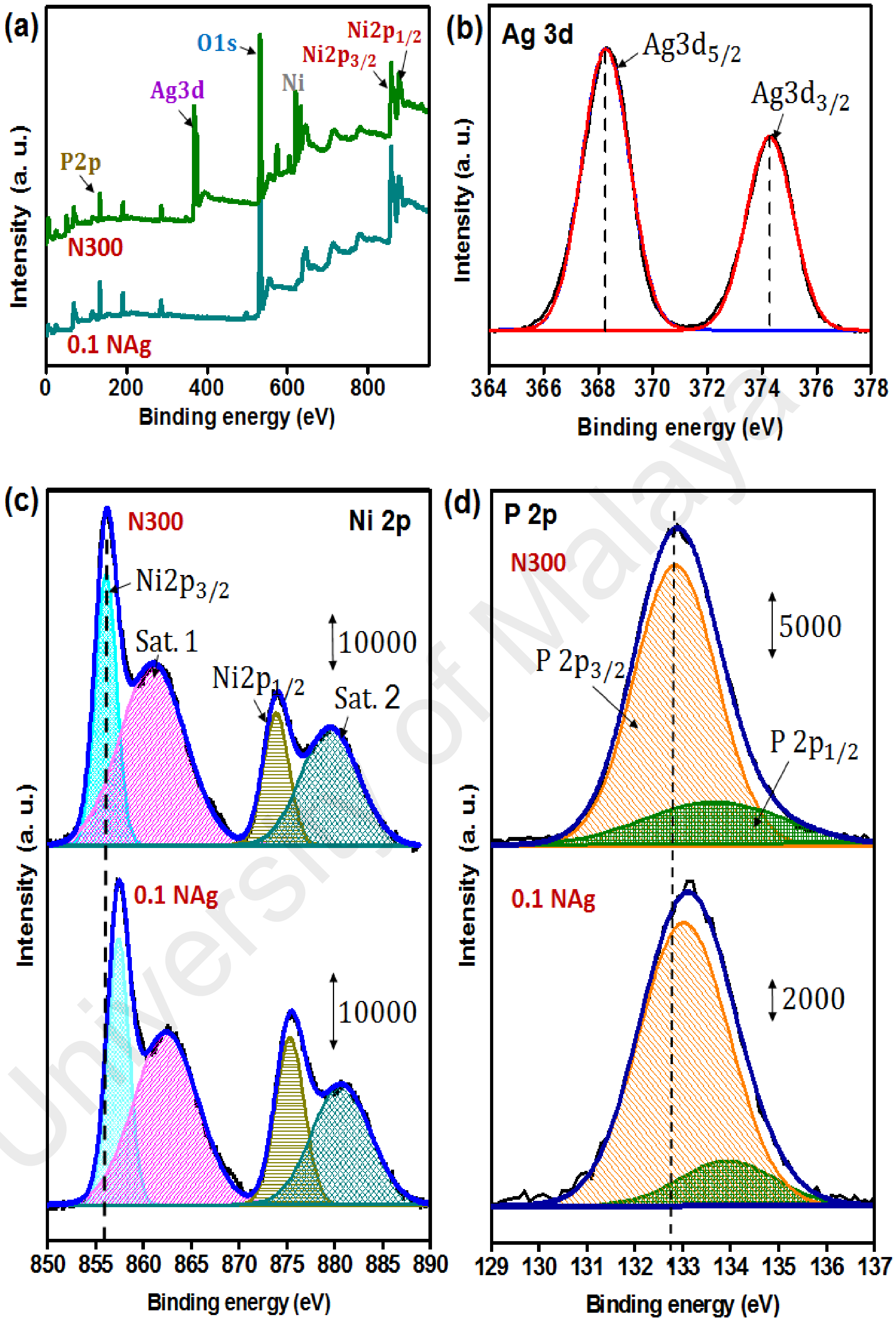

Figure 4.25: (a) XPS survey spectra of N300 and 0.1 NAg; deconvoluted spectra of (b) Ag 3d (c) Ni 2p (d) P 2p.

4.3.4 FESEM

The surface morphologies of 0.05 NAg, 0.1 NAg, 0.2 NAg and 0.3 NAg were visualized by FESEM analysis. Figure 4.26 shows that with gradual decrease in N300 contents present in the nanocomposite, the higher number of Ag_3PO_4 nanoparticles were deposited on the surface of N300 as marked by the yellow arrow. Unfortunately, some of Ag_3PO_4 nanoparticles were too small to be recognized via FESEM as shown by Figure 4.26(c) (inset). For 0.05 NAg, high degree of particle agglomeration was perceived, which led to mitigate in the electrochemical surface area. This might be due to the excess formation of Ag_3PO_4 nanoparticles that hindered the free movement of N300 particles (Amarnath et al., 2016). Figure 4.26(d) displays the higher magnification FESEM image of 0.05 NAg where Ag_3PO_4 nanoparticles with an approximate size of 8 nm were decorated on the surface of N300 particles. For all NAg nanocomposites, the variations in the content of the as-prepared $Ni_3(PO_4)_2$ did not affect the shape and size of N300 particles. The FESEM results indicated that the low concentration of the as-prepared $Ni_3(PO_4)_2$ during the synthesis process with $Ag(NH_3)_2^+$ led to the increase in the number of Ag_3PO_4 nanoparticles that deposited on the surface of N300. Nonetheless, contradict effect can be obtained if the content of N300 is too low as in 0.05 NAg in which particles are agglomerated, resulting in reduce of electroactive surface area.

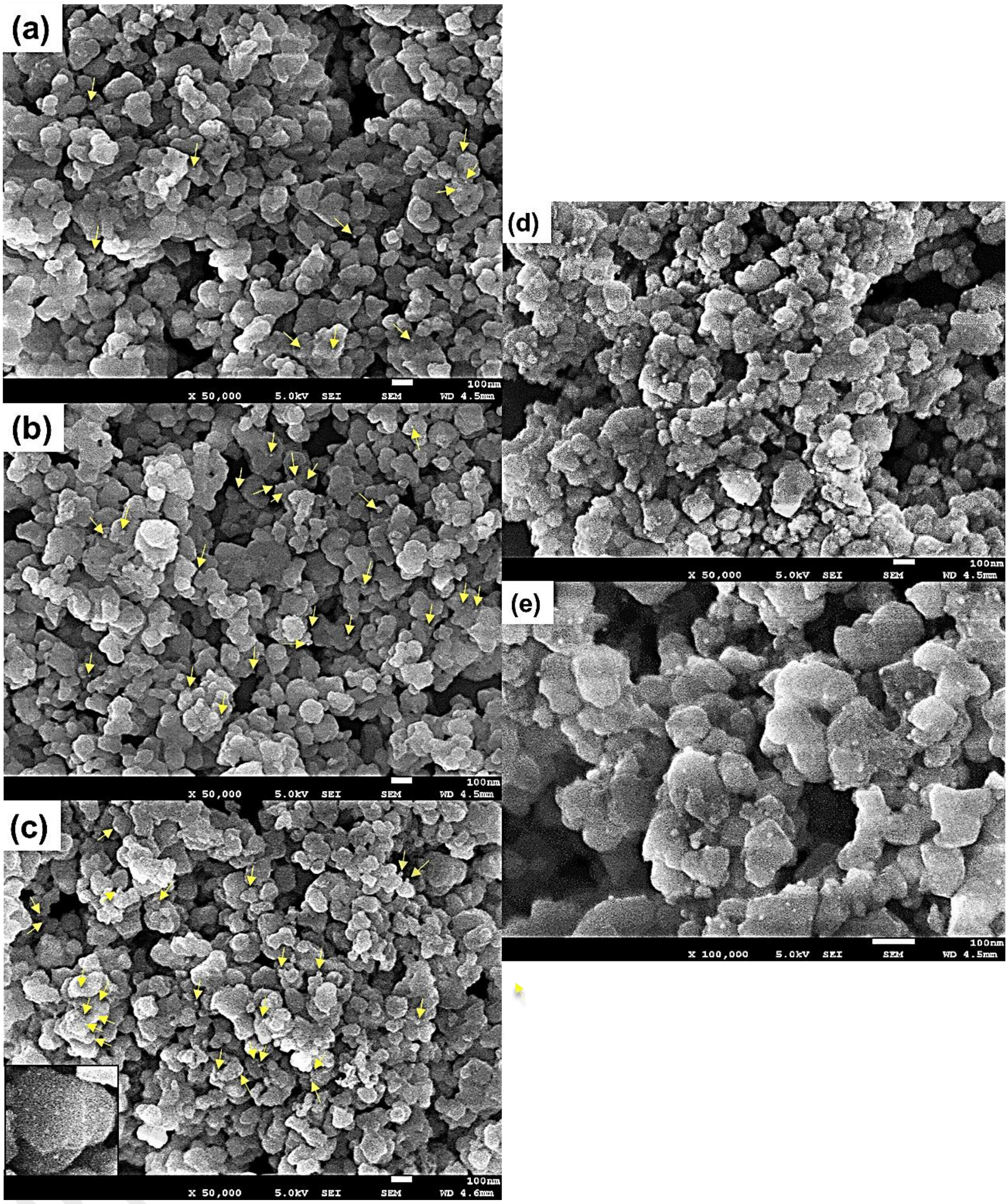

Figure 4.26: FESEM image of (a) 0.3 NAg, (b) 0.2 NAg and (c) 0.1 NAg; FESEM image of 0.05 NAg at (d) low and (e) high magnification.

4.3.5 HRTEM

In order to further explore the morphology of 0.05 NAg in detail, HRTEM was conducted and the results are shown in Figure 4.27. It clearly shows the cyrstalline structure of Ag_3PO_4 nanoparticles are decorated on the surface of N300. Surprisingly, N300 has high porous structure which could not be seen via FESEM images. This porous structure is greatly advantageous for supercapattery as this kind of structure supplies more rooms for the penetration of electrolyte ions during charging and discharging. This results is the main reason on why N300 electrode outperformed N600 and N900 electrodes as discussed in the previous system.

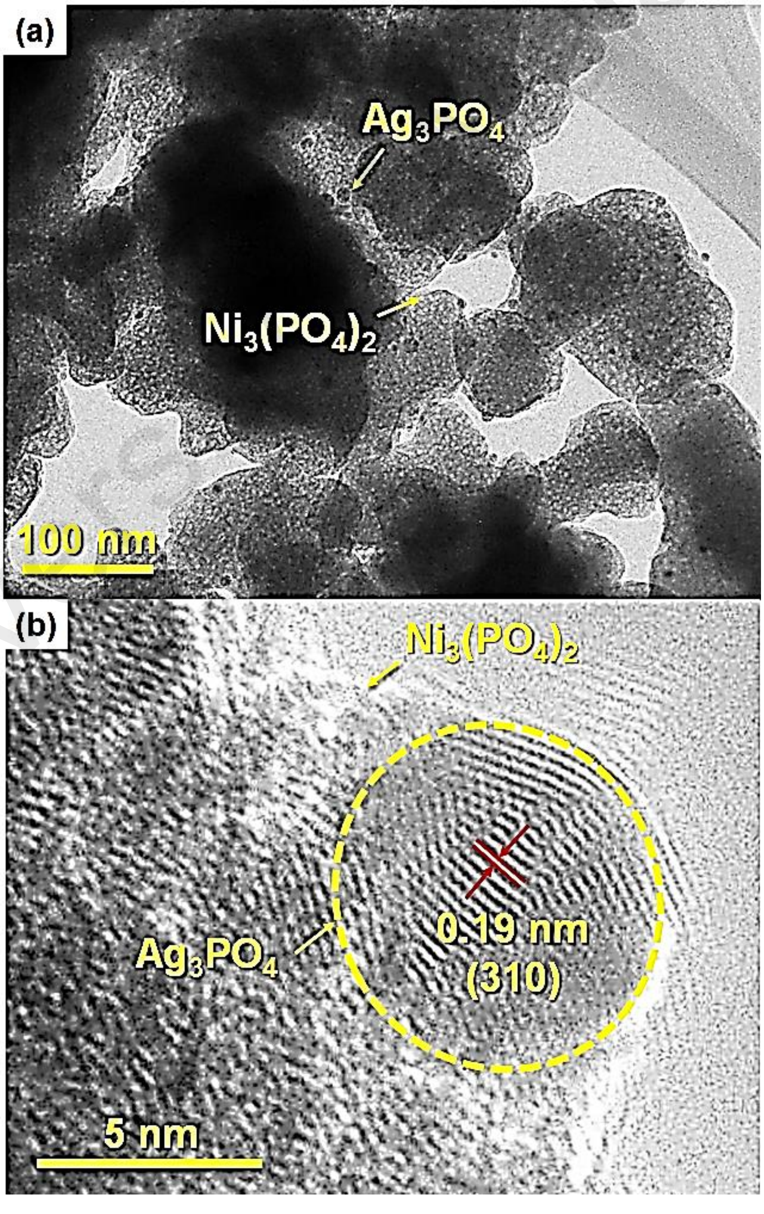

Figure 4.27: HRTEM image 0.05 NAg at (a) low and (b) high magnification.

The lattice resolved HRTEM image of 0.05 NAg revealed a lattice spacing of 0.19 nm, which matches with the characteristic distance between (310) planes of Ag_3PO_4 (Figure 4.27(b)). This confirmed that black dots seen in the HRTEM image were Ag_3PO_4 nanoaparticles. N300 does not show any lattice pattern which is the apparent for amorphous structure.

4.3.6 Electrochemical studies (Three-electrode cell)

4.3.6.1 CV

The CV curves of 0.05 NAg, 0.1 NAg, 0.2 NAg and 0.3 NAg measured at the scan rate of 5 mV/s in the potential window between 0 to 0.6 V are depicted in Figure 4.28. A pair of redox peak was observed for all samples indicates that all NAg nanocomposites are battery-type materials. This is linked to the diffusion of electrolyte ions through the NAg nanocomposites which leads to the redox reaction of the functional groups that were present on the surface of materials (Duraisamy et al., 2016). Notice that the redox peak potentials of each nanocomposite are different. This can be explained by the different electronic transmission path and electrolyte ions diffusion kinetics as the effect from the various mass ratio of $Ni_3(PO_4)$ and Ag_3PO_4 used for all nanocomposites. Therefore, this observation suggests that the electron and ion mobility is influenced by the amount of phosphate functional groups as well as the number of metal ions present in the nanocomposite (Chen et al., 2016).

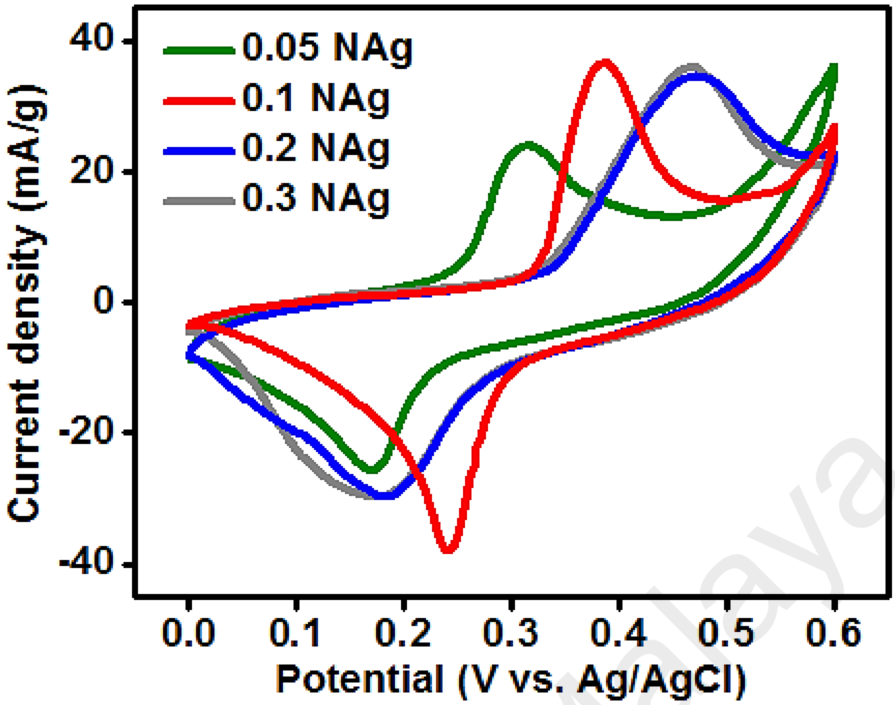

Figure 4.28: CV curves of 0.05 NAg, 0.1 NAg, 0.2 NAg and 0.3 NAg at scan rate of 5 mV/s.

Figure 4.29 displays the redox peak currents of 0.05 NAg, 0.1 NAg, 0.2 NAg and 0.3 NAg were augmented progressively with increasing scan rates from 5 mV/s to 100 mV/s. it is well-accepted that the redox peaks observed for all samples can be expressed by the following chemical equations;

$$Ni_3(PO_4)_2 + OH^- \rightleftharpoons Ni_3(OH)(PO_4)_2 + e^- \tag{4.4}$$

$$Ag_3PO_4 + OH^- \rightleftharpoons Ag_3(OH)PO_4 + e^- \tag{4.5}$$

According to the equations, the anodic peaks are contributed to the oxidation of $Ni_3(PO_4)_2$ (and Ag_3PO_4) to $Ni_3(OH)(PO_4)_2$ (and Ag_3PO_4) while the cathodic peaks are attributed to the reverse reduction process. These equations showing that the anodic and cathodic peaks observed at the CV curves are contributed from the two redox reactions. Noticeably, the oxidation and reduction peaks shifted to higher and lower potentials, respectively, with increasing scan rates. This is related to the increase in internal diffusion resistance within the electrode materials which hindered to the fast electron flows from the electrode materials to the Ni foam (Pang et al., 2015). In addition, the CV area for 0.3 NAg almost diminished at high scan rates (from 30 - 100 mV/s) because of the content of non-conductive N300 in 0.3 NAg is dominant. Thus, the electron flow is slower and consequently, at high range of scan rates, some of the electroactive sites of N300 did not participated during oxidation nd reduction process.

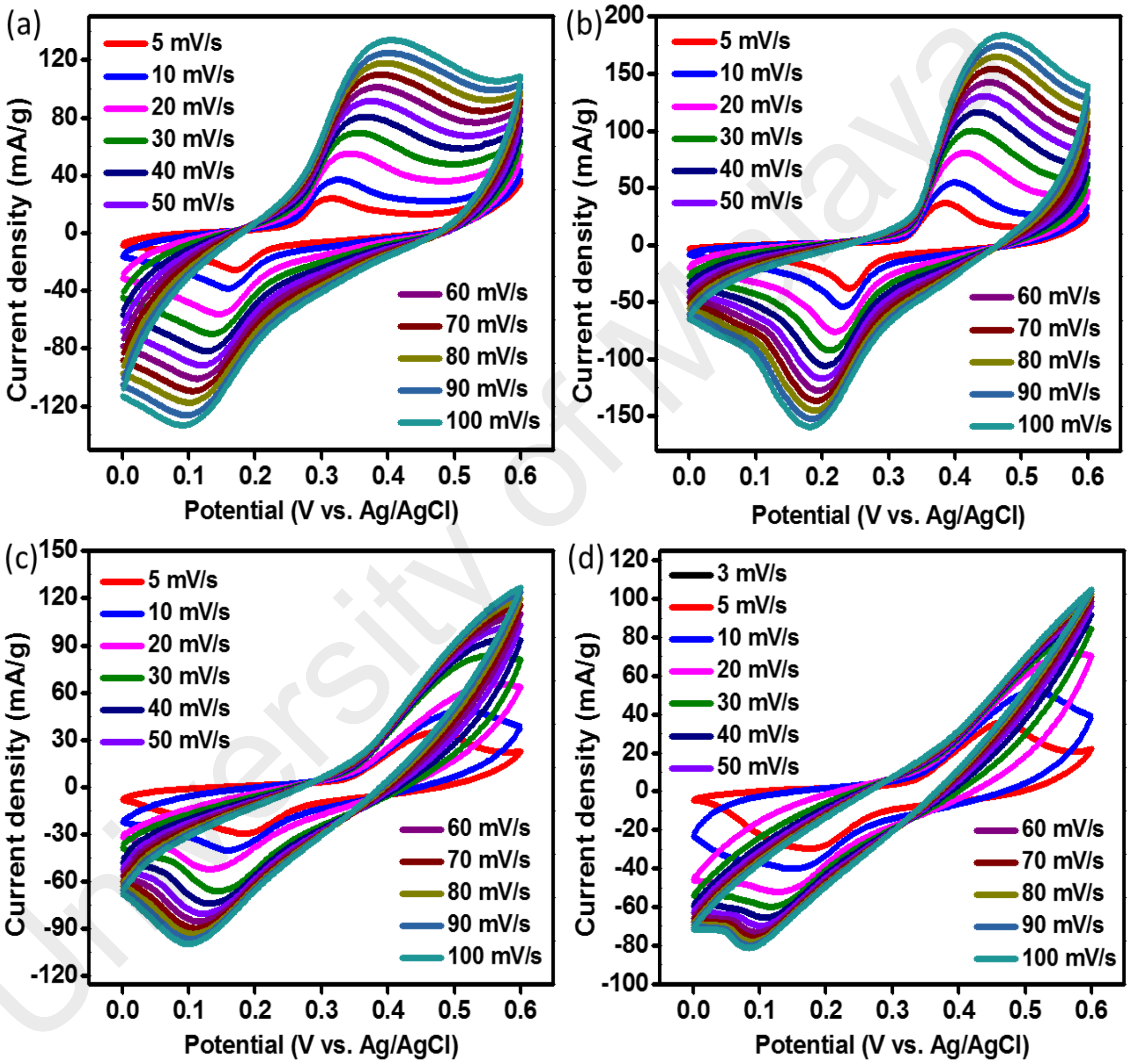

Figure 4.29: CV curves of (a) 0.05 NAg, (b) 0.1 NAg, (c) 0.2 NAg and (c) 0.3 NAg at the scan rate of 5 - 100 mV/s.

4.3.6.2 GCD

Figure 4.30 shows the GCD curves of 0.05 NAg, 0.1 NAg, 0.2 NAg and 0.3 NAg, respectively. The non-linear shape of discharge curves with a slow decay of potential shown by all electrodes is due to the charge storage that was governed by faradaic reaction of battery-type electrode. At low range of current densities, the charging and discharing curve are longer compared to higher current densities. This is attributed to the slow rate of current that is applied to the electrodes which contributed to the fully accessibility of OH^- troughout the electrode materials. At high curent densities, the OH^- did not have sufficient time to access the electrode material, thus the charge stored during oxidation and reduction is limited.

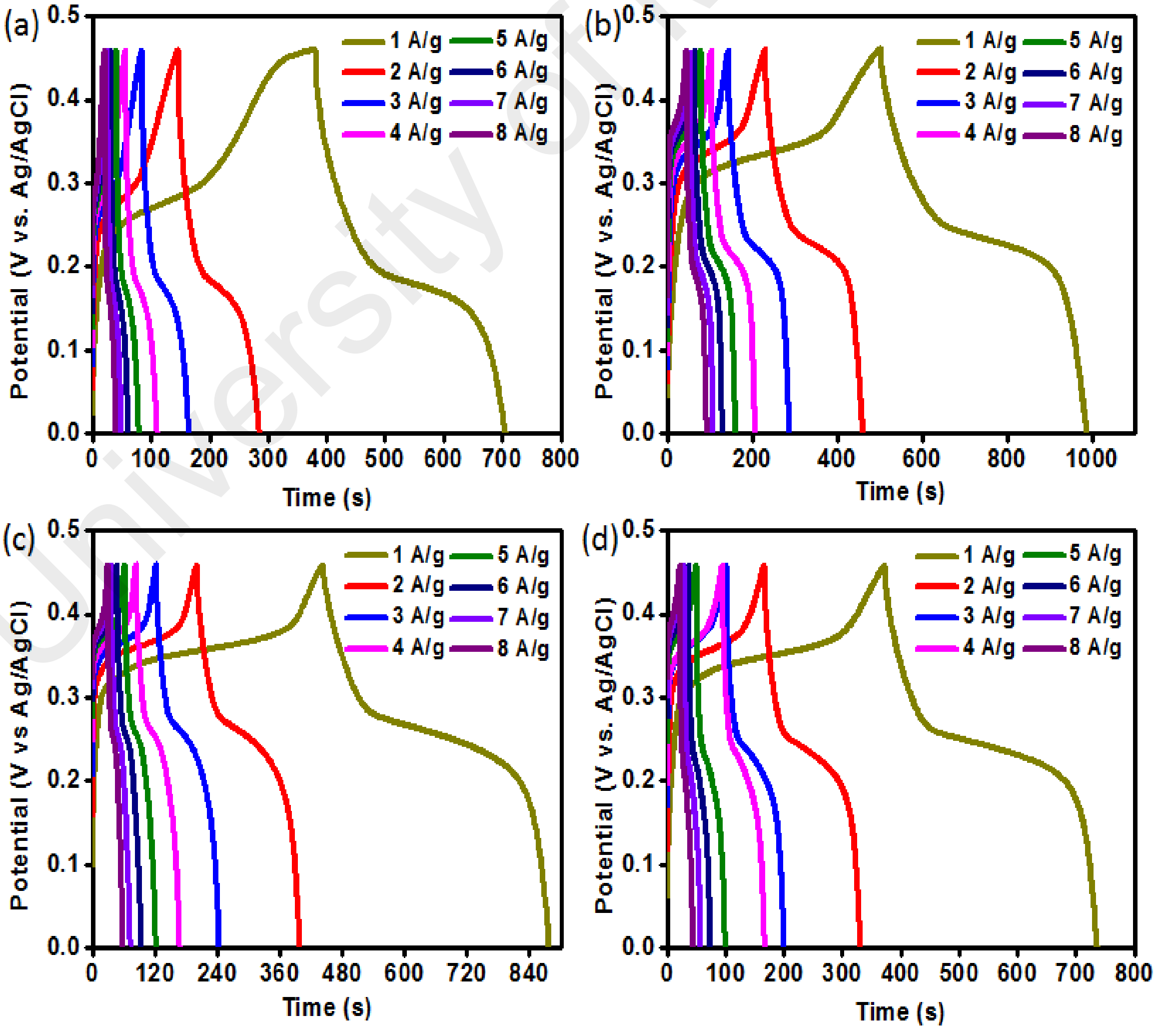

Figure 4.30: GCD curves of (a) 0.05 NAg, (b) 0.1 NAg, (c) 0.2 NAg and (d) 0.3 NAg at the current density of 1 - 8 A/g.

Figure 4.31 plots the specific capacity versus current density for all electrodes calculated from the obtained discharge time. It can be seen that 0.1 NAg exhibited a significant improvement in rate capability from 29 % (for N300 from System 2) to 78 %, where 0.05 NAg, 0.2 NAg and 0.3 NAg retained their specific capacity to 51, 48 and 47 % respectively, at the current density of 8 A/g. Rate capability of the electrode can be correlated with the electronic conductivity of the material. Thus, it is undoubtly to say that the improvement in rate capability achieved by all NAg nanocomposite as compared to N300 is because of the presence of Ag_3PO_4. As Ag_3PO_4 is naturally electrical conductive, it has reduced the internal resistance of the host N300 and thus boosted charge transfer kinematics (Li et al., 2016). Among the NAg nanocomposites, 0.1 NAg exhibited superior specific capacity at all applied currents followed by 0.2 NAg, 0.3 NAg and 0.05 NAg, manifesting that the conductivity of NAg nanocomposites was enhanced with the increasing amount of Ag_3PO_4 relative to N300.

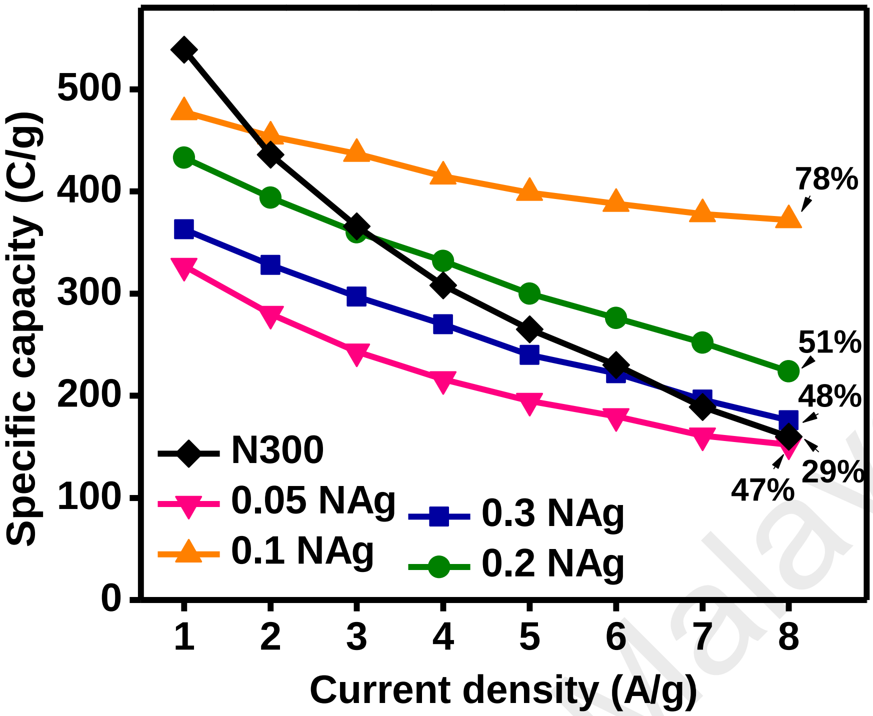

Figure 4.31: Specific capacity of 0.05 NAg, 0.1 NAg, 0.2 NAg and 0.3 NAg at different current densities.

However, the excessive of Ag_3PO_4 nanoparticles deteriorated the performance of 0.05 NAg electrode. This can be ascribed to the formation of particle agglomeration, which in turn reduced the contact area between electrode material and electrolyte, and consequently limit the driving force of redox reaction. Another reason is due to the insufficient amount of N300 that present in the nanocomposite, as N300 is highly responsible for electroactive sites for the occurrence of redox reaction (Ma et al., 2014).

4.3.6.3 EIS

Figure 4.32 shows the Nyquist plots of 0.05 NAg, 0.1 NAg, 0.2 NAg and 0.3 NAg. The ESR value of 0.76, 0.71, 0.89 and 0.99 Ω have been determined for 0.05 NAg, 0.1 NAg, 0.2 NAg and 0.3 NAg respectively, as illustrated in the Figure 4.32(a)(inset). Among NAg nanocomposites, 0.1 NAg displayed the smallest diameter, implying the lowest internal resistance. Moreover, the W_d deduced by the straight line in the Nyquist plot of 0.1 NAg in low frequency region is the steepest, indicating its low ion diffusion resistance. The CV, GCD and EIS results obtained for System 2 could be interpreted by the following reasons and the scheme is provided in Figure 4.32(b);

(i) Crystalline structure of Ag_3PO_4 nanoparticles exhibits different electron transfer rate than N300. The high number of pores offered by N300 enhanced the number of electrolyte ions penetration to the catalytically active interior surfaces. In this case, most the surfaces of N300 could be involved in the redox reactions. However, some inner surfaces of N300 could not be accessed by the electrolyte at a high current rate and renders low specific capacity (Gao et al., 2015). In contrast, for crystalline structure of Ag_3PO_4, the electrolyte ions only react to the outermost surface layer, not involving interior surfaces of the material. Thus, the nano-sized of crystalline Ag_3PO_4 provides additional effective surface area to the unutilized surfaces of N300 and maintain the high number of redox reaction at high current density (Vadivel et al., 2016).

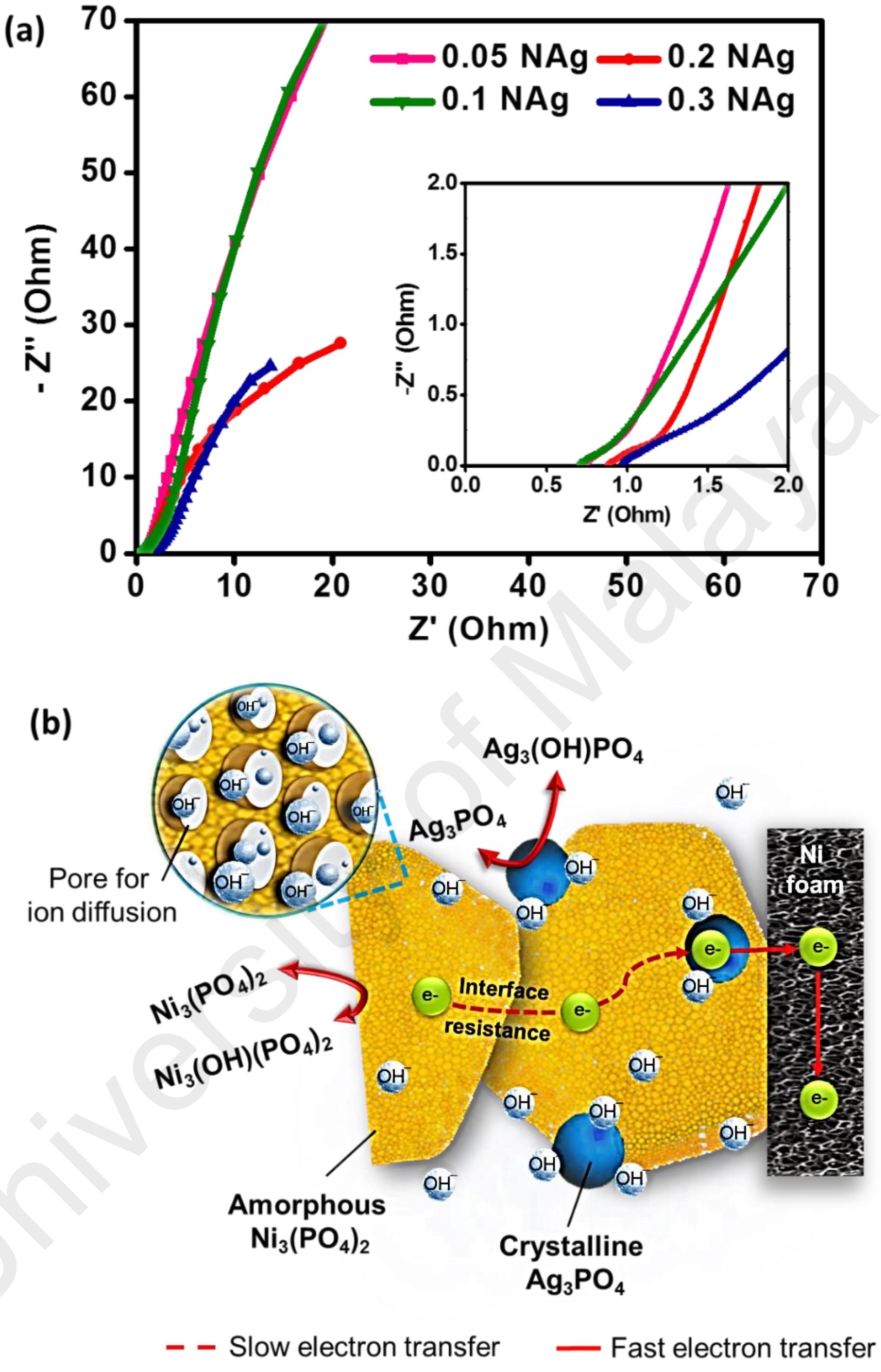

Figure 4.32: Nyquist plot of 0.05 NAg, 0.1 NAg, 0.2 NAg and 0.3 NAg; (b) Schematic illustration of surface reaction at NAg nanocomposite electrode.

(ii) even though the amorphous structure of N300 provides porous network for the accessibility of electrolyte ions, it has low electrical conductivity which impede electrons from transferring from one N300 particle to another particle easily (Xu et al., 2016). Herein, high electrical conductivity of Ag_3PO_4 nanoparticles that anchored on the poor conductivity of N300 act as a bridge shuttling electron continuously to the nickel foam and reduces the internal resistance of the nanocomposite. Moreover, the Ag_3PO_4 nanoparticles minimize the transport pathways distance for electrons movement towards the current collector, leading to high specific capacity even at high current density (Patil et al., 2013).

4.3.7 Electrochemical studies (Two-electrode cell)

Similar like what have been discussed in two-electrode cell fabrication for System 2 and System 3, the same supercapattery fabrication and analysis techniques were performed for 0.1 NAg. Because of 0.1 NAg exhibited the highest specific capacity among other NAg nanocomposites, 0.1 NAg was chosen to be fabricated as the positive electrode, and AC as the negative electrode. The results for fabricated supercapattery for System 2 are shown in Figure 4.33. Figure 4.33(a) exhibits the CV curve with stable shape with high current density from 5 mV/s to of 100 mV/s, and Figure 4.33(b) shows the almost symmetric charge and discharge curves from 0.5 to 8 A/g. These patterns insinuate the fast electron transfer between 0.1 NAg and electrolyte at the positive electrode in addition to the efficient electrolyte ion adsorption on the surface of AC at the negative electrode (Ma et al., 2016).

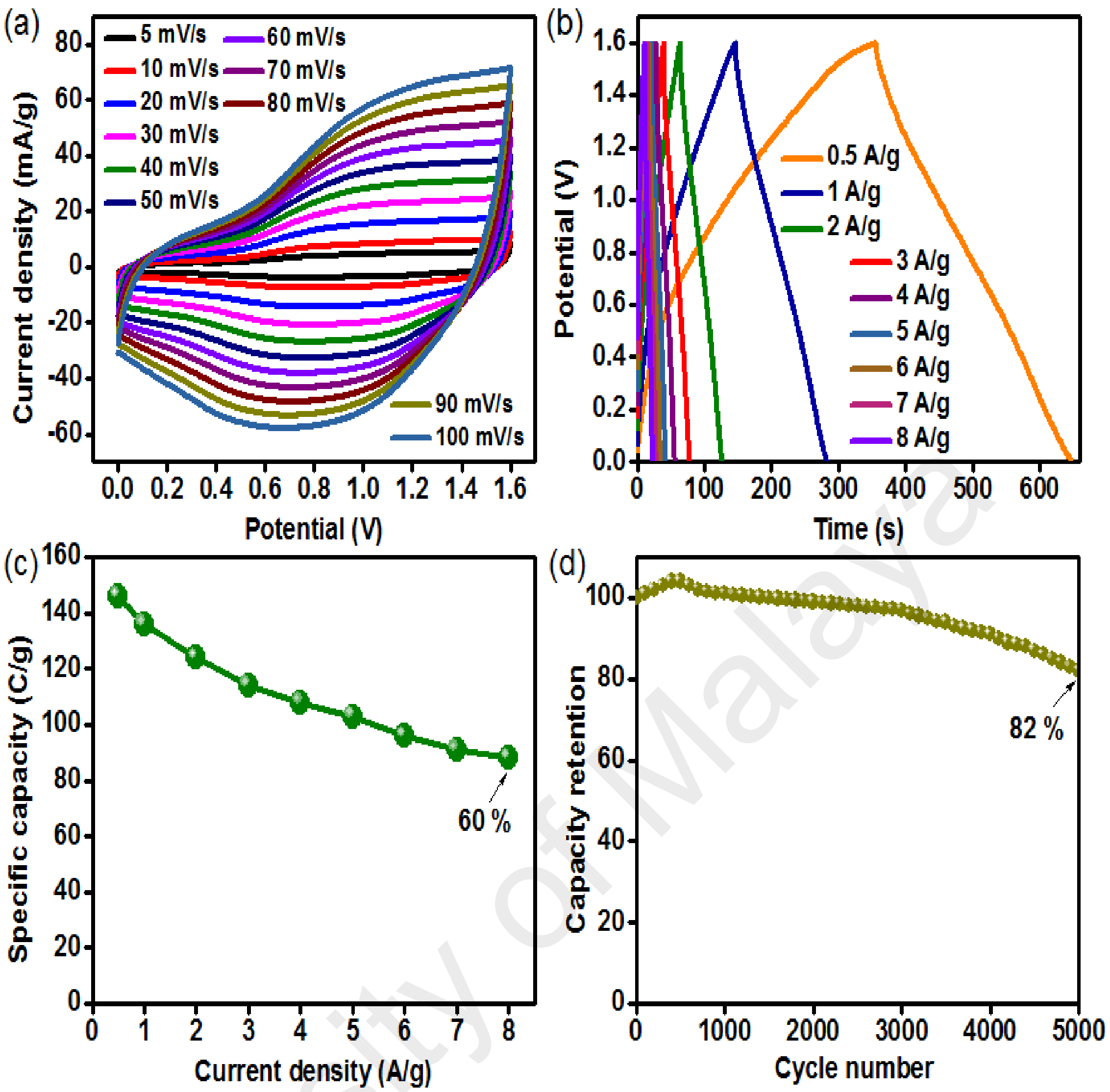

Figure 4.33: (a) CV curves of 0.1 NAg//AC measured at different scan rates; (b) GCD curves of 0.1 NAg//AC at different current densities; (c) the calculated specific capacity versus current density; (d) the cylic stability over 5000 cycles.

The specific capacity from the GCD curves was calculated and plotted in Figure 4.33(c). The specific capacity of 0.1 NAg//AC was 146 C/g at a current density of 0.5 A/g and retained to 60 % when the current density was increased from 0.5 A/g to 8 A/g. This capacity retention value is improve significantly as compared the the capacity retention of N300//AC as presented in the System 2. Figure 4.33(d) shows the stability of 0.1 NAg//AC after 5000 cycles of charge and discharge. The calculated capacity retention of 0.1 NAg//AC was 82 % at 5000th cycle, which is better than N300//AC. The improved in stability indicated that the presence of conductive Ag_3PO_4 has fasten the flow of electrons by facilitating the electrons transfer and enhancing the number of redox reaction during charging and discharging process.

4.4 System 4: Polyaniline-nickel phosphate-silver phosphate nanocomposite

4.4.1 XRD

The XRD results for PANI, PNAg (2:1), PNAg (1:1), PNAg (1:2) and PNAg (1:3) are given in Figure 4.34. PANI displayed several broad peaks at 2θ value of 14.8°, 20.9° and 25.3° which can be assigned to the (011), (020) and (200) lattice planes of semi-crystalline PANI chains. For all PNAg nanocomposites, a series of sharp diffraction peaks can be seen, indicating the presence of crystalline Ag_3PO_4 (contributed from 0.1 NAg). However, as the amount of PANI in the PNAg nancomposite increased, the intensity of the PANI peaks was dissappear gradually. This is possibly due to the increase in inter-space distance of PANI affected from the intercalation of 0.1 NAg nanocomposite (Han et al., 2014; Philip et al., 2005). While the peaks at 2θ value of 28.1°, 32.3°, 36.6°, 46.5°, 52.1°, 55.0° and 57.5° resulted from the (200), (210), (211), (310), (222), (320) and (321) planes of the body-centered cubic-phase of Ag_3PO_4 (JCPDS, 06-0505) with a space group of P4-3n, respectively. By comparing the XRD patterns of all PNAg nanocomposites with 0.1 NAg nanocomposite from System 3, there is no alteration in the peak positions of 0.1 NAg, indicating that the mixing of PANI does not affect the composition of 0.1 NAg. However, several additional peaks (marked as O) were observed at PNAg (2:1) and PNAg (1:1). The peaks which are positioned at 38.4°, 44.4° and 64.4° can be readily indexed as the (022), (032) and (221) planes of the monoclinic phase of silver oxide (Ag_3O_4) (JCPDS, 84-1261) with a space group of P21/c, respectively.

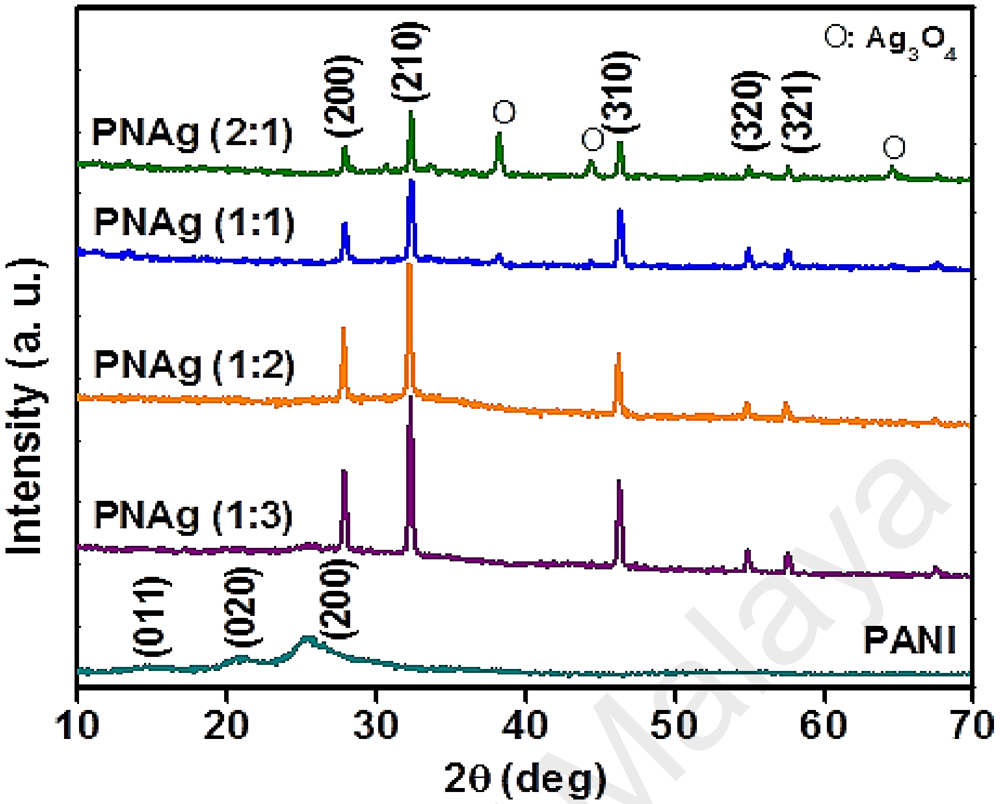

Figure 4.34: XRD diffractogram of PANI, PNAg (2:1), PNAg (1:1), PNAg (1:2) and PNAg (1:3).

The intensity of the peaks from Ag_3O_4 gradually increased with the further increase of the PANI loading. This demonstrates that the synthesized PANI has oxidized Ag^+ due to the fact that PANI in this work contains APS as the strong oxidant. Eventhough PANI has been washed several times, certain amount of APS molecules might still sticked together with PANI. Thus, in this case, APS not only oxidized aniline, but also oxidized Ag^+ to Ag^{2+}, forming Ag_3O_4 (Aguilar et al., 2016). In the case of PNAg (1:3) and PNAg (1:2), the reflection peaks of Ag_3O_4 was not detected due to APS molecules may not be sufficient to oxidize Ag^+, attributed to the low amount of PANI. Another possible reason is because of the interaction between Ag^+ and the air. Ag^+ was initially reacted with Cl^- (Cl^- came from HCl which was used as a dopant during PANI synthesis) and formed AgCl. Nonetheless, due to the weak interaction between Ag^+ and Cl^-, Ag^+ was easily dissociated from Cl^- and subsequently interacted with the surrounding air and form oxidized Ag.

4.4.2 FTIR

FTIR of PANI, PNAg (2:1), PNAg (1:1), PNAg (1:2) and PNAg (1:3) are shown in Figure 4.35. For Figure 4.35a, the bands at 1451 and 1560 cm^{-1} observed at PANI spectrum correspond to C = C and C = N stretching vibrations in benzenoid and quinoid rings. The band at 1293 cm^{-1} was assigned to the C−N stretching of secondary aromatic amine, a characteristic of PANI in the bipolaron emeraldine salt form. Those peaks for all the nanocomposites are right-shifted, hinting that the blending of 0.1 NAg into PANI enhanced the conjugated effect for PANI (Ding et al., 2015). Likewise as shown in Figure 4.35b, the bands at 563 and 1036 cm^{-1} (assigned to triply degenerate bending mode of the O−P−O bond (ν_4 PO_4^{3-}) and triply degenerate asymmetric stretching mode of the P−O bond (ν_3 PO_4^{3-})) are right-shifted to 565 and 1045 cm^{-1}, respectively. In the case of the broadened band between 2840 until 3480 appreared due to the interaction between the N−H and −OH groups of PANI and 0.1 NAg. These results confirmed the effective composition between PANI and 0.1 NAg which is in good agreement with the XRD results.

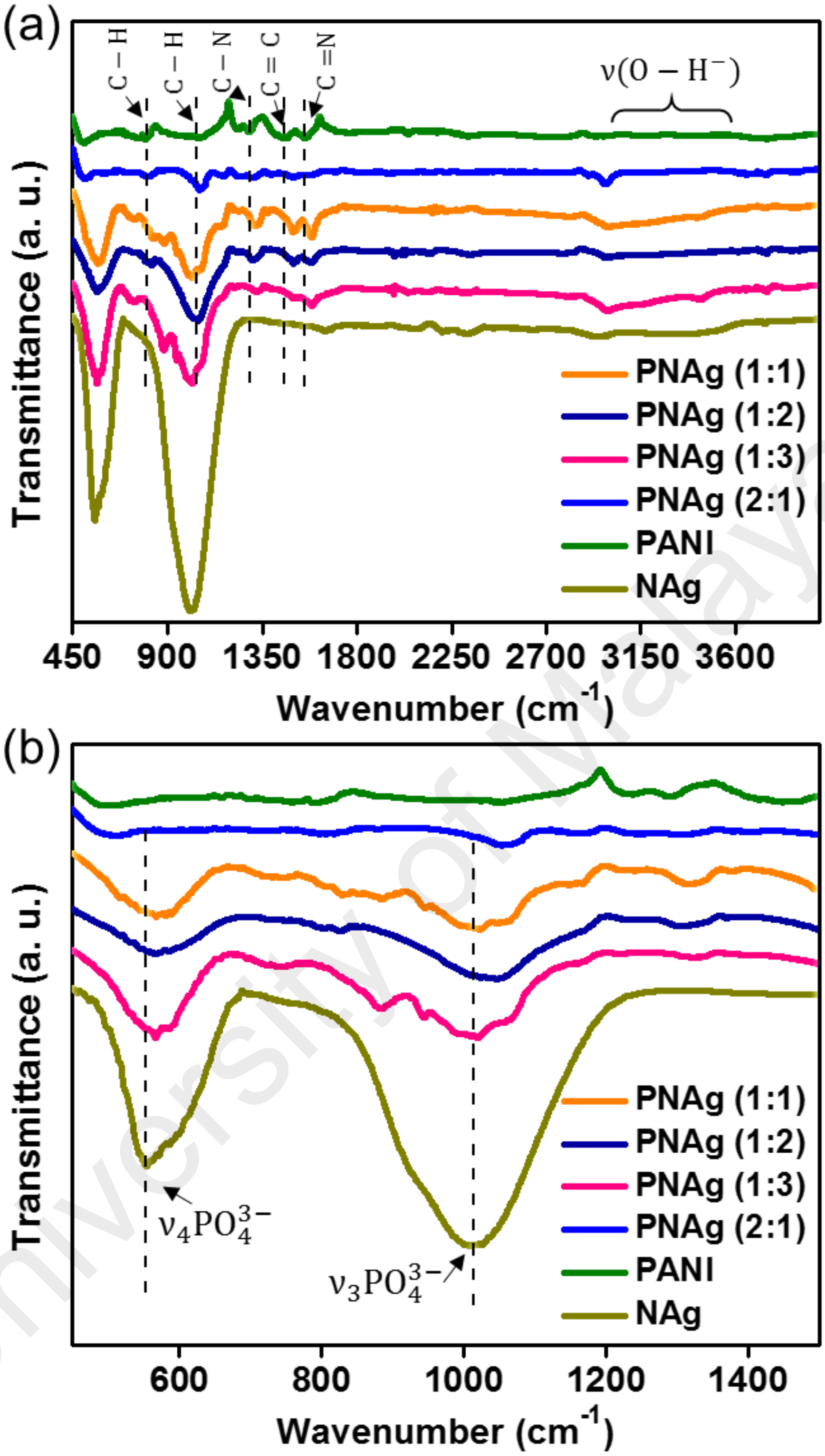

Figure 4.35: FTIR patterns of PANI, NAg, PNAg (2:1), PNAg (1:1), PNAg (1:2) and PNAg (1:3).

4.4.3 XPS

The survey XPS spectrum of PNAg (1:1) displayed several sharp peaks confirmed the existence of N, Ni, Ag, O and P (Figure 4.36(a)). The two peaks at the Ag3d spectra correspond to Ag3d$_{5/2}$ and Ag3d$_{3/2}$, respectively (Figure 4.36b). Unlike NAg, the assignment of Ag3d$_{5/2}$ can be further resolved into three peaks suggesting three different states of silver whichh exist in PNAg (1:1). The peaks at 366.2 and 367.2 eV correspond to the higher oxidation state of Ag (i.e. Ag_3O_4 and Ag_2O) while the peak at 368.8 corresponds to Ag^+ of Ag_3O_4. This finding also detected the existence of the oxidized Ag which is strongly support the XRD results (Kaspar et al., 2010). Based on the peak area ratio of the deconvoluted peaks for PNAg (1:1), about 42.2 % of the total area is contributed from the oxidized Ag. While the high resolution XPS spectra of Ni2p as shown in Figure 4.36c can be deconvoluted into two peaks (Ni 2p$_{3/2}$ and Ni 2p$_{1/2}$) attributed from the spin-orbital splitting accompanied by the satellite signals (sat.1 and sat 2). As compared to Ni 2p spectra shown in Section 4.3.3 (0.1 NAg in System 3), Ni 2p$_{3/2}$ peak in PNAg (1:1) was slightly shifted by 0.4 eV. This postulates that the electronic structure of $Ni_3(PO_4)_2$ (referring to N300) is barely tuned by the presence of conducting PANI. The unchanged in the electronic structure is due to the interaction between 0.1 NAg and PANI was only physical interaction as both materials were only blended using mortar. Figure 4.36d shows the N1s spectrum that was resolved into four peaks. These peaks represents four different oxidation states in PNAg (1:2). The peaks located at 398.5, 399.0, 401.1 and 402.7 eV are assigned to imine $(=\mathrm{N}-)$, amine $(-\mathrm{NH}-)$, protonated amine $(-\mathrm{NH}_2^+)$ and protonated imine $(=\mathrm{NH}^+-)$, respectively. The area of fraction of these peaks is 0.36, 0.29, 0.12 and 0.23, respectively, where the total area from protonated N atoms is 35 %, stipulating the doping level of PANI in PNAg (1:1) was 35 % (Aliev et al., 2016; Tong et al., 2014). These results confirmed the successful preparation of PNAg composites which are consistant with the XRD and FTIR results.

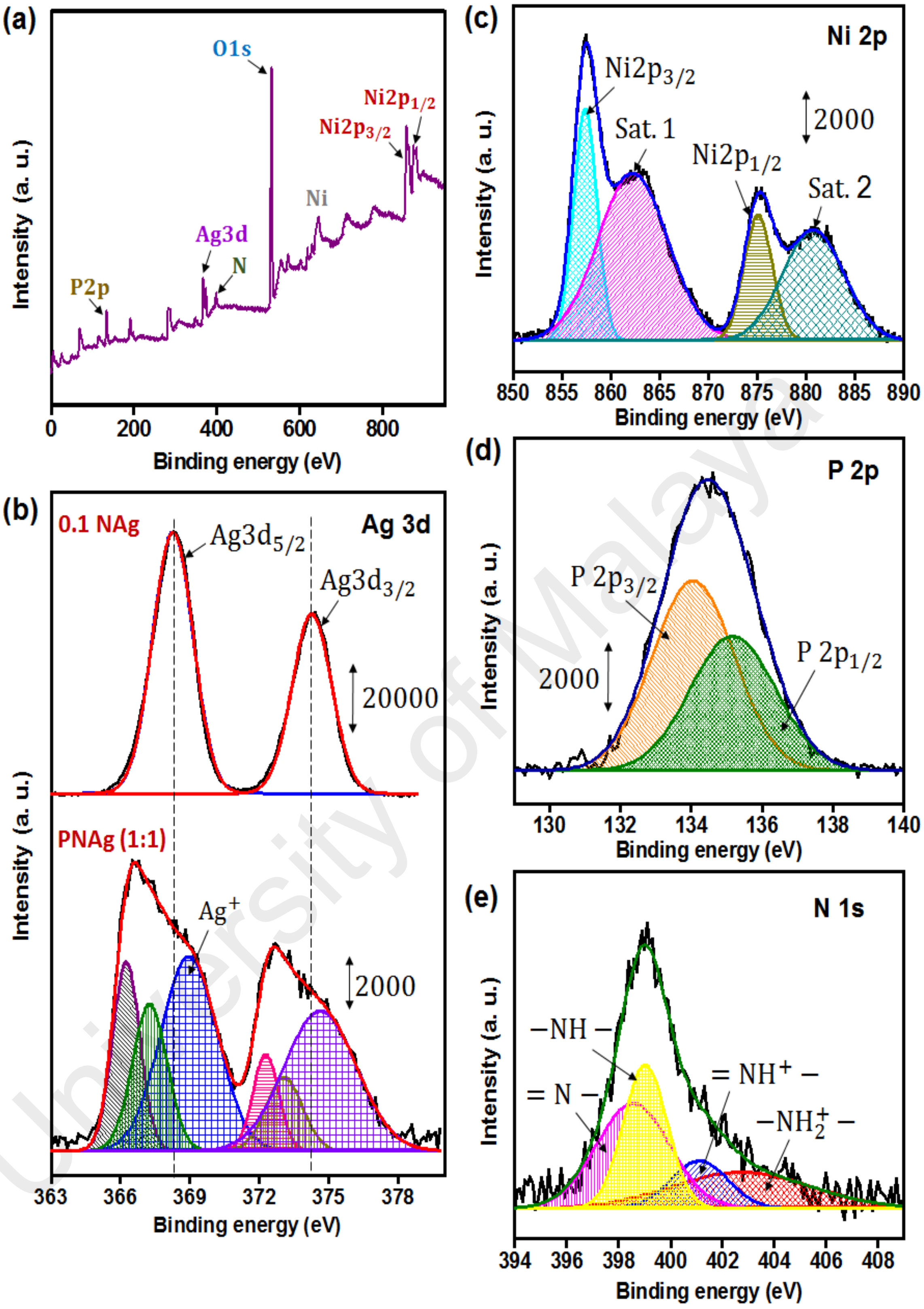

Figure 4.36: (a) XPS survey spectra of PNAg (1:1); XPS spectra of (b) Ag 3d (c) Ni 2p (d) P 2p (e) N 1s.

4.4.4 FESEM

The distribution of 0.1 NAg particles on PANI is viewed using FESEM and EDX analysis. The surface morphologies of PANI and PNAg (1:1) are displayed in Figure 4.37. Figure 4.37(a) shows an interconnected tubular shape PANI with an average diameter of 100 nm. As explained in System 1, the interconnection morphology was observed at PANI caused by the effect of the proton acid doping into PANI increases the polarity of the molecules (Cai et al., 2017). While Figure 4.37(b) displays the gaps between the tubular PANI are filled with 0.1 NAg particles which indicates the good inclusion of 0.1 NAg particles into PANI. Hence, it can be concluded that 0.1 NAg and PANI are support each other and improve the dense of 0.1 NAg particles and PANI.

The elemental distribution and purity of PNAg (1:1) was further investigated by EDX elemental mapping as shown in Figure 4.38. Figure 4.38(a) exhibits the FESEM image of PNAg (1:1) used for analysing EDX elemental mapping. Figure 4.38(b-e) show the uniformly destributed of the independent nitrogen (N), nickel (Ni), silver (Ag) and phosphorus (P) elements, proves the homogenous decoration of 0.1 NAg particles on PANI. The EDX spectrum (Figure 4.38(f)) provides the additional evidence of the detectable elements; oxygen (O), N, Ni, Ag and P in PNAg nanocomposite. 0.1 NAg nanocomposite contain negatively charged phosphate groups while PANI has positively charged $-\mathrm{NH}^+$ groups that are available in its backbone. During physical blending of 0.1 NAg with PANI, 0.1 NAg particles were simply adsorbed on the high surface area of PANI caused by the maximum electrostatic force of attraction (Dey et al., 2012).

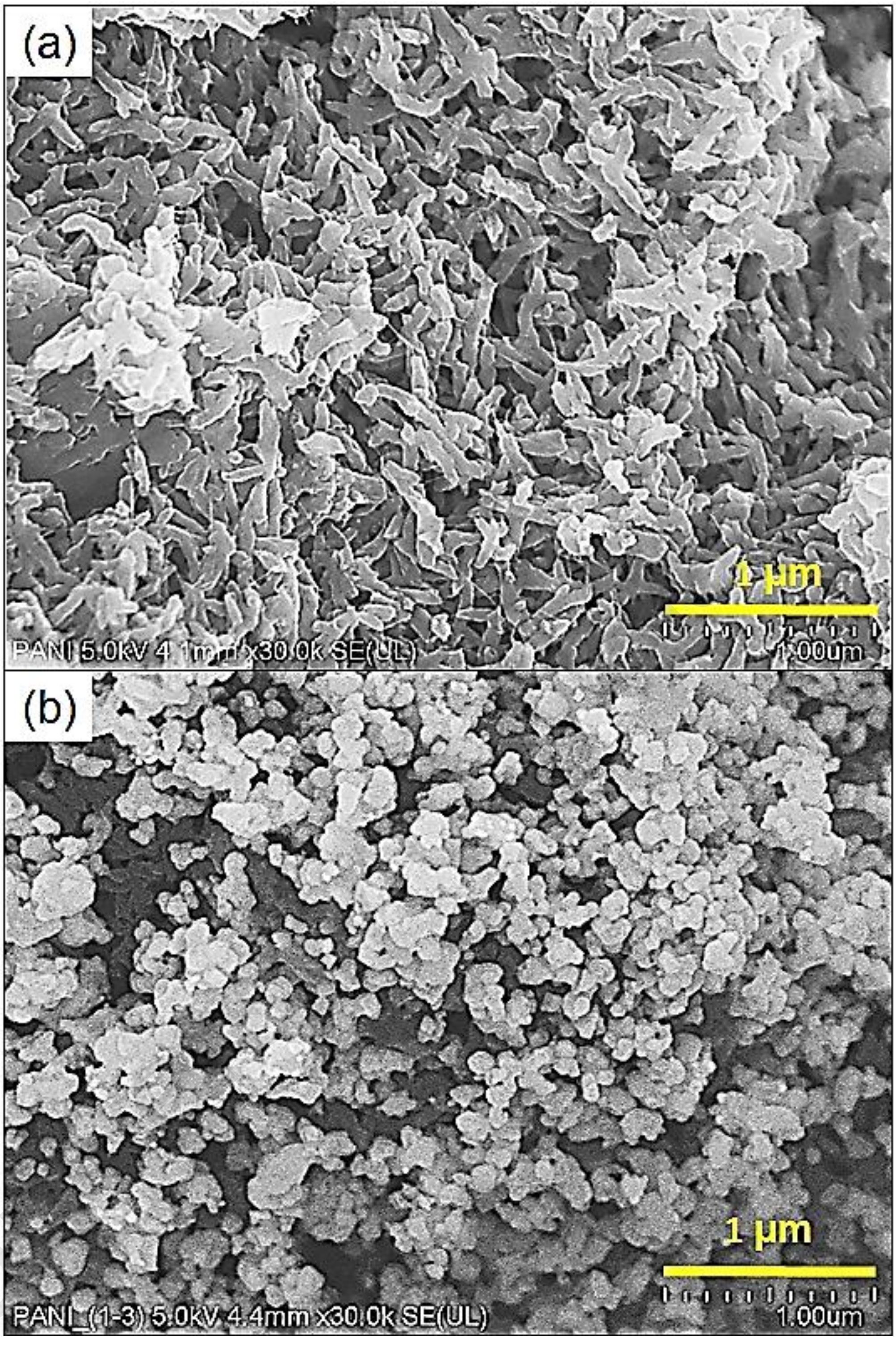

Figure 4.37: FESEM image of PNAg (1:1).

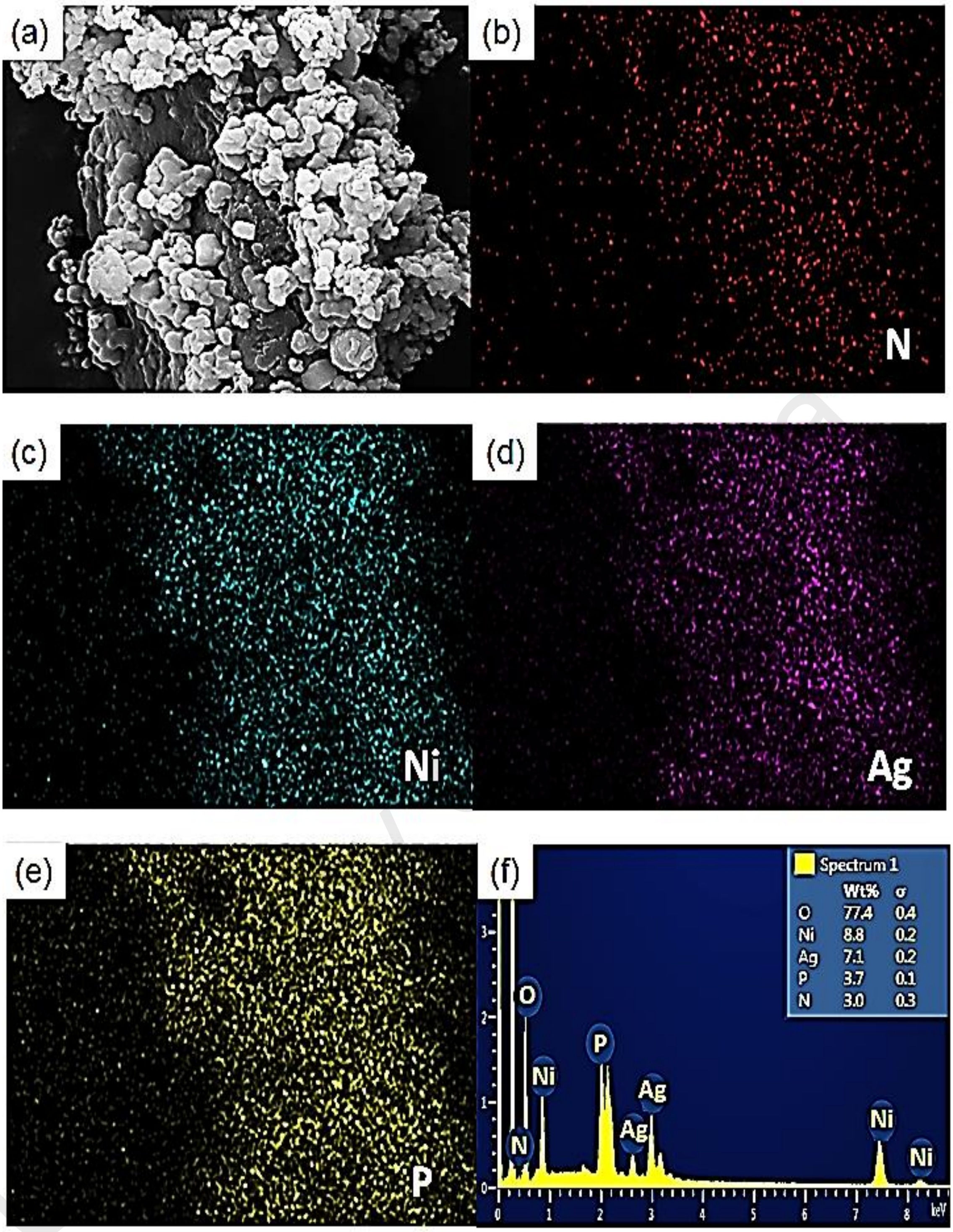

Spectrum 1	Wt%	σ
O	77.4	0.4
Ni	8.8	0.2
Ag	7.1	0.2
P	3.7	0.1
N	3.0	0.3

Figure 4.38: (a) FESEM image of PNAg (1:1); distribution of (b) N, (c) Ni, (d) Ag and (e) P; (f) the EDX pattern of PNAg (1:1).

4.4.5 HRTEM

The morphology and inner structure of PANI and PNAg was further viewed via HRTEM. Figure 4.39(a) shows the tubular morphology of PANI and the irregular edge of PANI can be clearly perceived from the Figure 4.39(b). No lattice was detected and the appearance of PANI was translucent, affirming the short-range order of PANI amorphous structure. Additionally, some dark spot was seen which is due to the overlapping tubular PANI. Figure 4.40(a) and Figure 4.40(b) revealed different magnifications of PNAg (1:1). These images spotlight that the surface of PANI is mostly covered by 0.1 NAg nanocomposite. It was observed that the presence of PANI does not cause an apparent increase or decrease in the particle sizes of 0.1 NAg. Unfortunately, the existence of Ag_3O_4 particle could not be clearly recognized which might be due to distribution of the particles is not dominant in the PNAg (1:1). However, these images are evident for the good contact between PANI and NAg, verifying that the physical blending method is capable of forming composite system. In addition, the differences in surface charge exists in PNAg (1:1) raised the strong electrostatic interaction between PANI and 0.1 NAg (Dey et al., 2012).

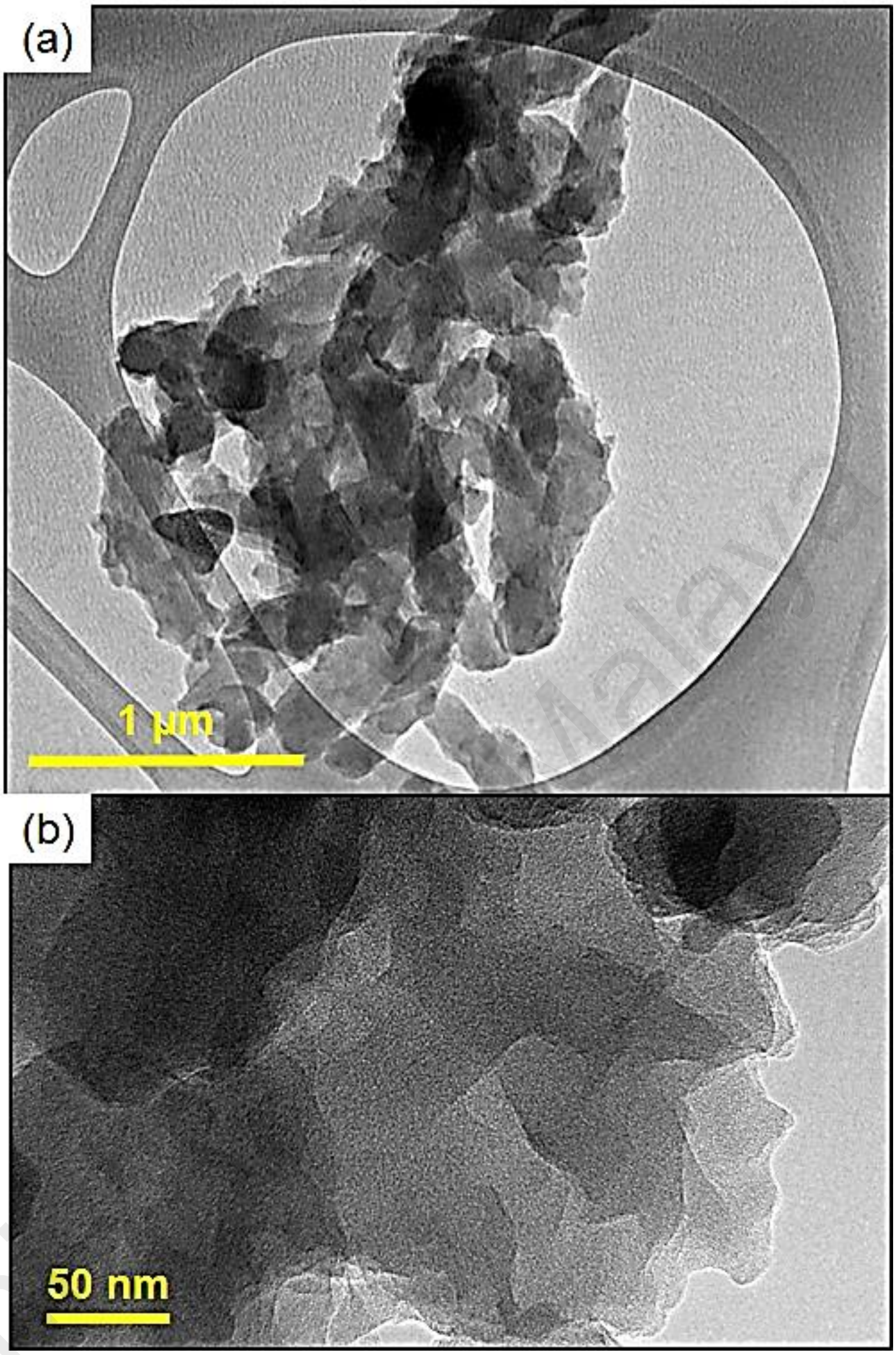

Figure 4.39: HRTEM image of PANI at (a) low and (b) high resolution.

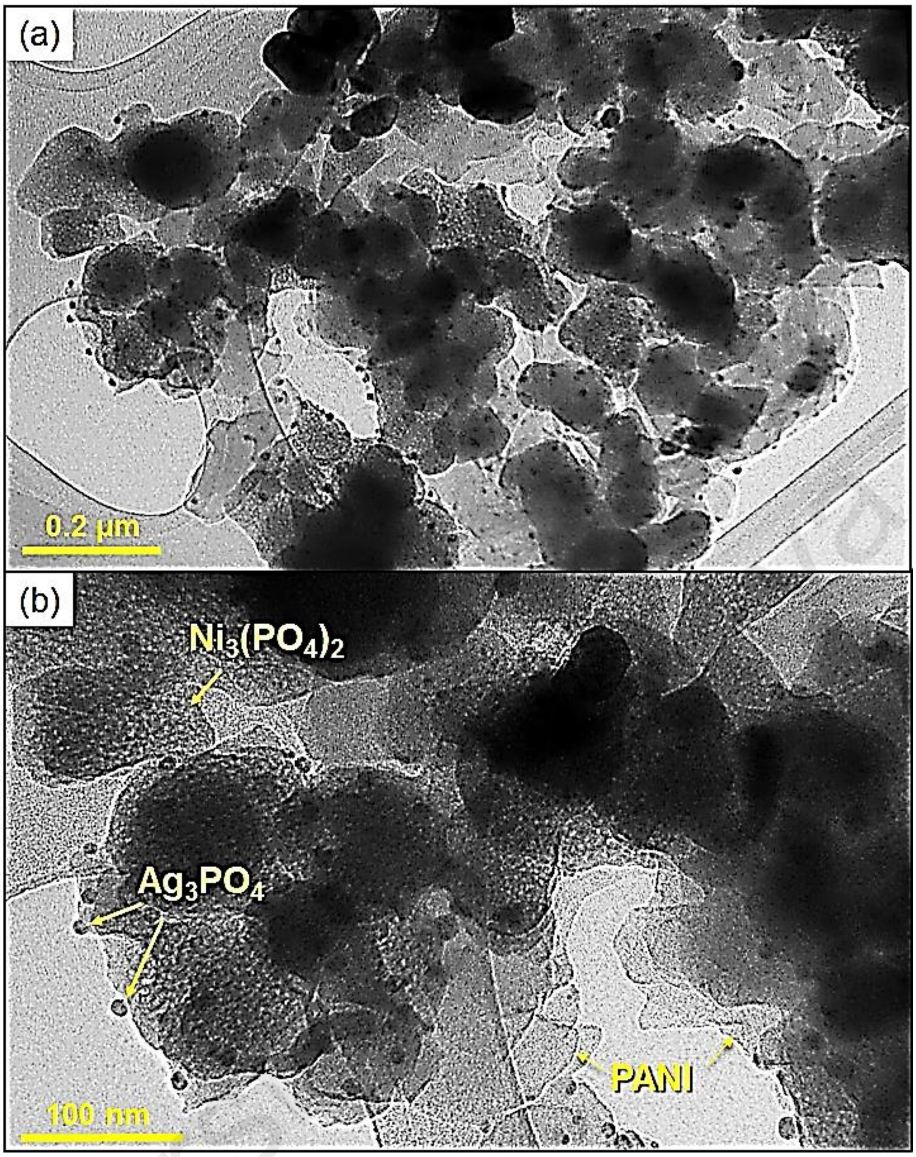

Figure 4.40: HRTEM image of PNAg (1:1) at (a) low and (b) high resolution.

4.4.6 Electrochemical studies (Three-electrode cell)

4.4.6.1 CV

Figure 4.41 depicts the CV shape of PANI as the potential of redox peaks did not seriously impacted with the increasing scan rates. This can be explained by the fast redox reaction happened between PANI and KOH electrolyte which indicates the high electrical conductivity of PANI. As pointed by the arrow, two pairs of redox peaks were observed which corresponds to the electron exchange occured between different oxidation states of PANI. Specifically, C1/A1 peaks were associated with the redox transition between leucoemeraldine (semiconducting state) and polaronic emeraldine (conducting state), while A2/C2 peaks were attributed to the transition between emeraldine and pernigraniline.

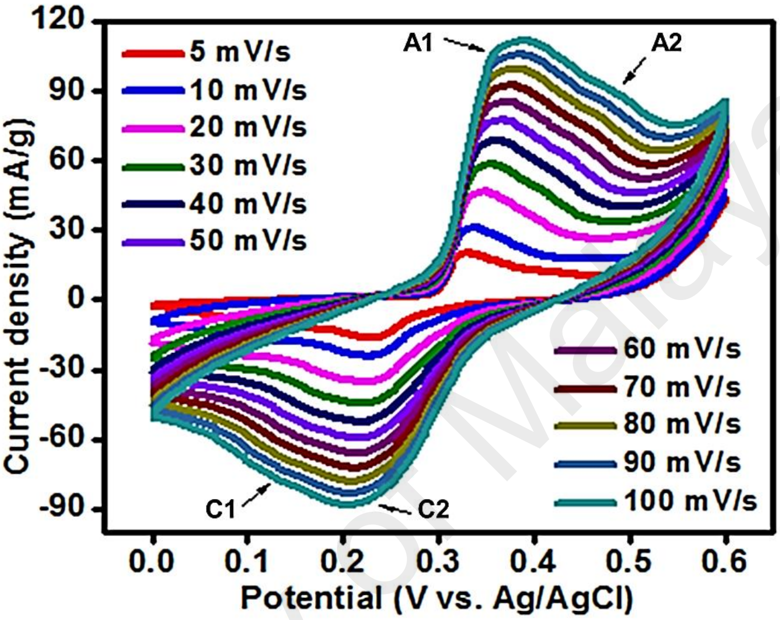

Figure 4.41: CV of PANI at the scan rate of 5 - 100 mV/s.

While the CV curves of PNAg (2:1), PNAg (1:1), PNAg (1:2) and PNAg (1:3) measured at the same scan rates (5 - 100 mV/s) are shown in Figure 4.42. Based on all CV graphs, the redox peak currents of PANI, PNAg (2:1), PNAg (1:1), PNAg (1:2) and PNAg (1:3), respectively, were augmented progressively with the increasing scan rates due to an increase in internal diffusion resistance within the electrode materials. The appreareance of redox peaks at all electrode materials indicated that the charge storage is governed by faradaic reaction. For PNAg (1:1), PNAg (1:2) and PNAg (1:3), the two pairs of oxidation and reduction peaks as observed at PANI can be seen. The disappearance of the peaks of PANI in the nanocomposites suggested that the redox reaction happened during forward and reverse scans was dominated by 0.1 NAg (Chen et al., 2016).

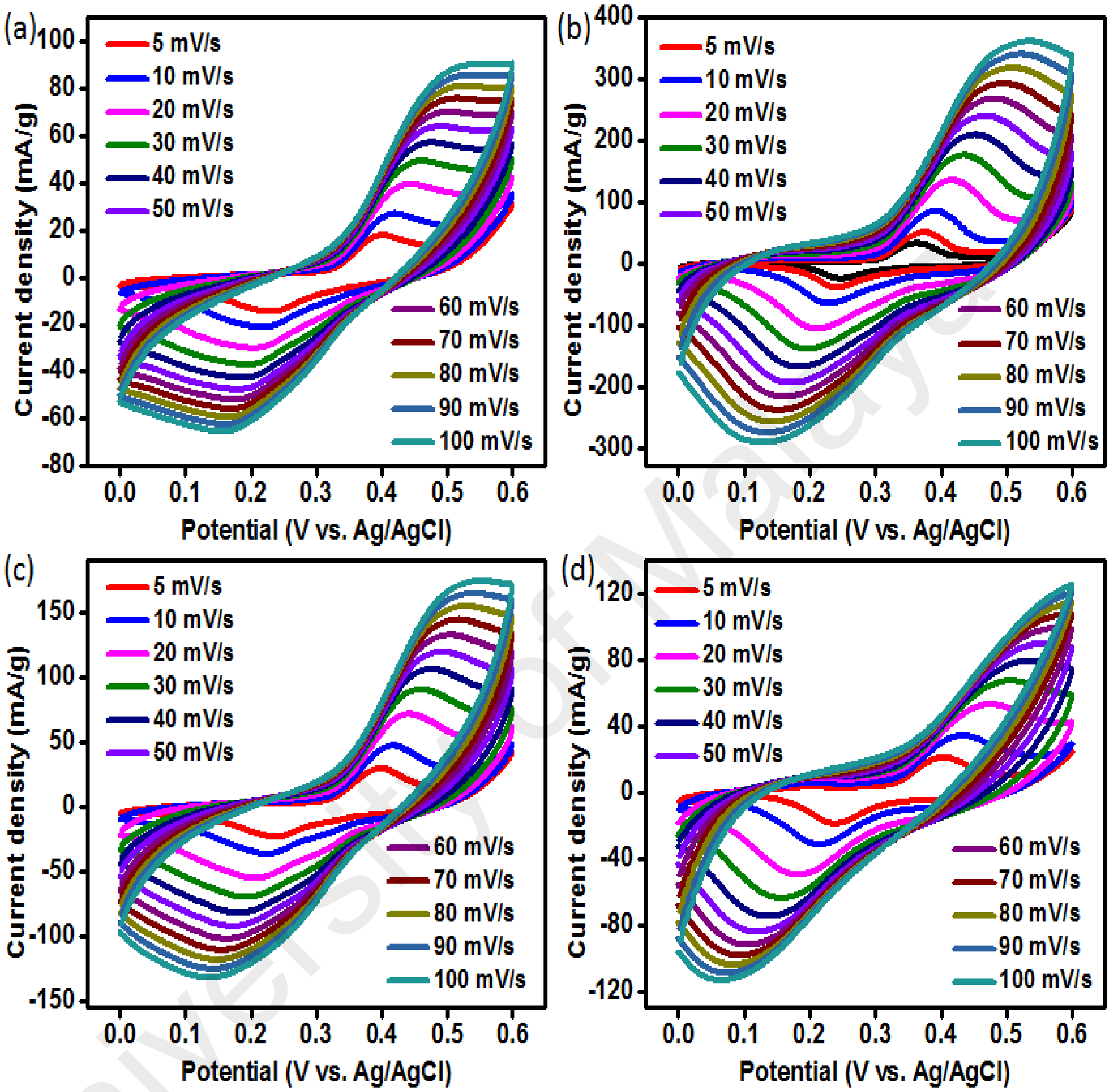

Figure 4.42: CV curves of (a) PNAg (2:1), (b) PNAg (1:1), (c) PNAg (1:2) and (d) PNAg (1:3) at the scan rate of 5 - 100 mV/s.

Figure 4.43 compares the CV curves of PANI, PNAg (2:1), PNAg (1:1), PNAg (1:2) and PNAg (1:3) at the scan rate of 20 mV/s. Each sample exhibited different potential of oxidation and reduction peak, indicating that they have dissimilar electronic transmission path and resulting in different electronc transmission rate. The combination of different ration of PANI and 0.1 NAg influence the ability of the nanocomposite to gain or loss electrons, leading to a different redox potential. Thus, this proposed that the electron and ion mobility is influenced by the amount of PANI, phosphate functional groups as well as the number of metal ions present in the nanocomposite.

The redox peaks observed for PNAg nanocomposites appreared is contributed from the faradaic reaction happened at each component in the nanocomposites; 0.1 NAg and PANI. For 0.1 NAg, when it interacted with OH^- of KOH electrolyte can be expressed by the following redox equations (Pang et al., 2015);

$$Ni_3(PO_4)_2 + OH^- \rightleftharpoons Ni_3(OH)(PO_4)_2 + H_2O + e^- \tag{4.6}$$

$$Ag_3PO_4 + OH^- \rightleftharpoons Ag_3(OH)PO_4 + H_2O + e^- \tag{4.7}$$

While as for PANI when it in contact with OH^-, the redox transitions of PANI corresponds to the conversion between emeraldine and leucoemeraldine state of PANI. Moreover, as PANI is electrical conductive, it allowed for fast electron mobility towards the Ni foam which also contributed to high redox current. Thus, this is sufficient to conclude that the redox process happened at PNAg was cumulated from the synergetic effect of PANI and 0.1 NAg (Chen et al., 2013). As shown in the figure, PNAg (1:1) exhibited the largest CV area as compared to other electrodes. This demonstrates that the electrochemical performance of PNAg (1:1) is significantly improved owing to the right amount ratio of PANI and 0.1 NAg. Nonetheless, PNAg (2:1) exhibited lower redox peak current than PANI which might be due to too less amount of 0.1 NAg particles are present in the nanocomposite. As discussed in the previous system, 0.1 NAg provides a large porous structure to be occupied by the electrolyte ions. Since the amount of 0.1 NAg is small, less interaction between 0.1 NAg and OH^- can happen, thus less electrons can be produced. This also demonstrates that PANI alone is not enough to store high amount of charge. Where as for PNAg (1:2) and PNAg (1:3), the deterioration of performance was observed which might be due to the agglomeration of 0.1 NAg particles that limited the property enhancement of nanocomposites.

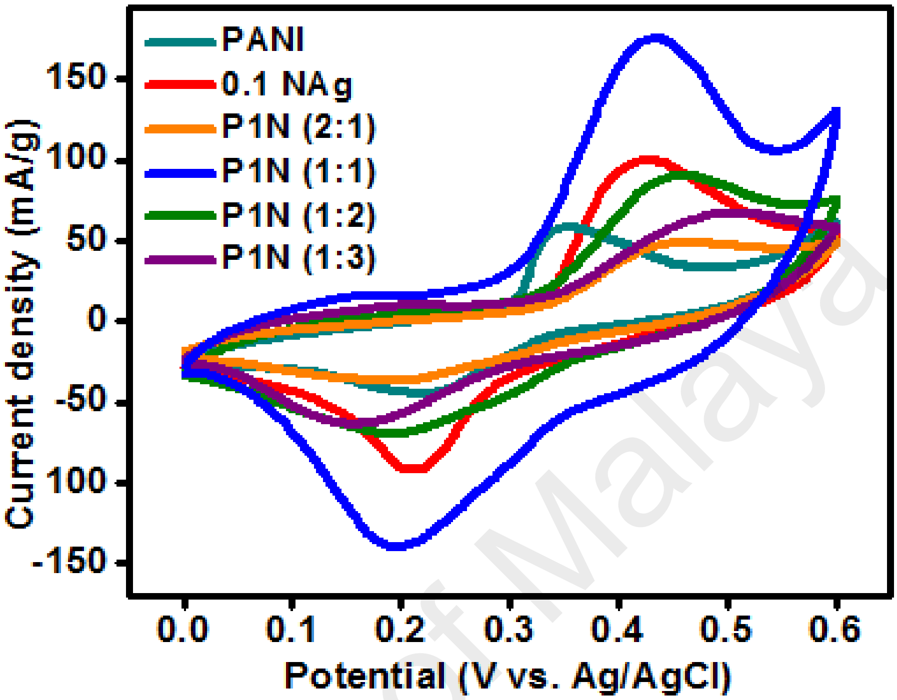

Figure 4.43: CV curves of PANI, 0.1 NAg, PNAg (2:1), PNAg (1:1), PNAg (1:2) and PNAg (1:3) at the scan rate of 20 mV/s.

4.4.6.2 GCD

Figure 4.44 and Figure 4.45 illustrate the charge-discharge curves of PANI, PNAg (2:1), PNAg (1:1), PNAg (1:2) and PNAg (1:3). The non-linear shape of the curves signifies the involvement of faradaic reaction during charging and discharging process which indicates all samples are battery-type materials. The electrodes took longer time to get fully charged and discharged at lower current densities. This is due to the low current rate applied to the electrodes which causes slow the OH^- diffusion throughout the electrode materials. As the current densities increasing, the samples charged and discharged faster due to the fast OH^- diffusion within the cell. Notice that for PANI electrode, it almost reached saturated charging. This means that PANI has smaller electrochemical window and this clearly hints that the incorporation of 0.1 NAg into PANI can enhance the operating potential window of the electrodes.

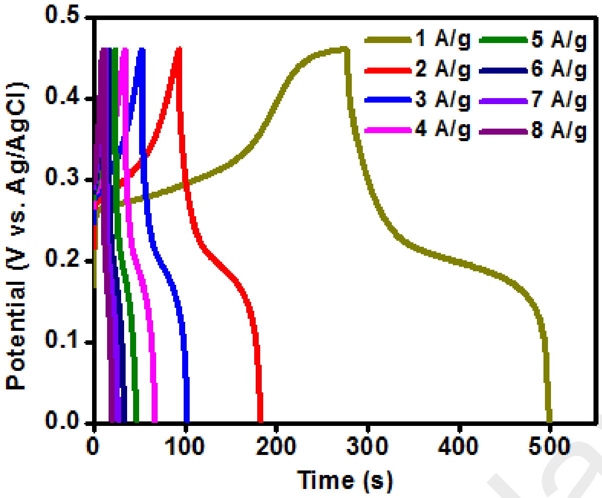

Figure 4.44: GCD of PANI at the current density of 1 - 8 A/g.

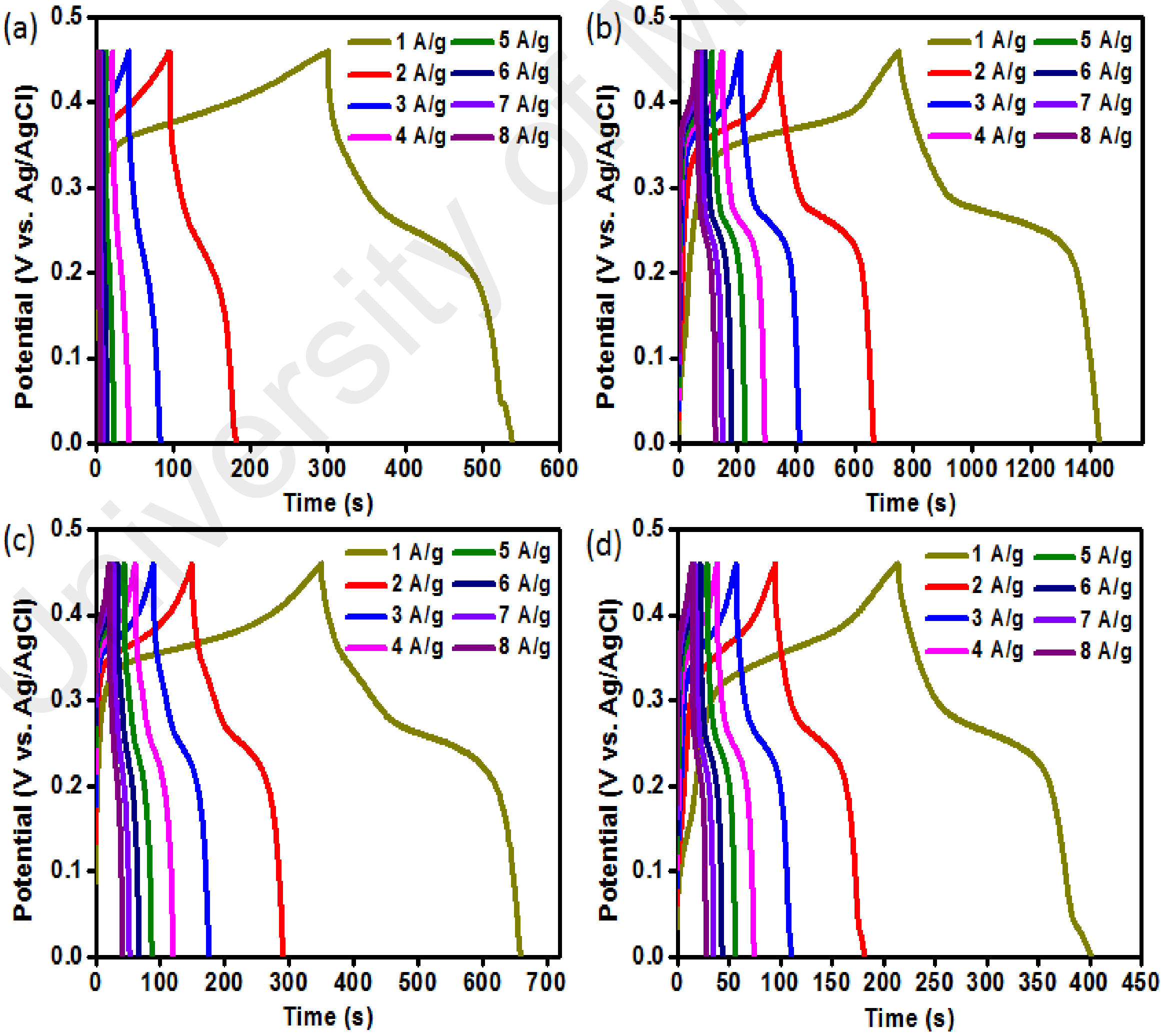

Figure 4.45: GCD curves of (a) PNAg (2:1), (b) PNAg (1:1), (c) PNAg (1:2) and (d) PNAg (1:3) at the current density of 1 - 8 A/g.

Figure 4.46 plots the specific capacity (Q_S) versus current density for all electrodes calculated from the discharge curve of GCD results. For all samples, the calculated specific capacity decreases with increasing current density. This phenomenon is commonly happens for battery-type electrodes due to the incapability of the inner active sites to sustain the redox process at higher current rates. It can be seen that PNAg (1:1) showed the highest specific capacity at all current densities. In addition, PNAg (1:1) exhibited the highest rate capability with 75 % capacity retention at 8 A/g as compared with PANI (33 %), PNAg (2:1) (13 %), PNAg (1:2) (57 %) and PNAg (1:3) (62 %).

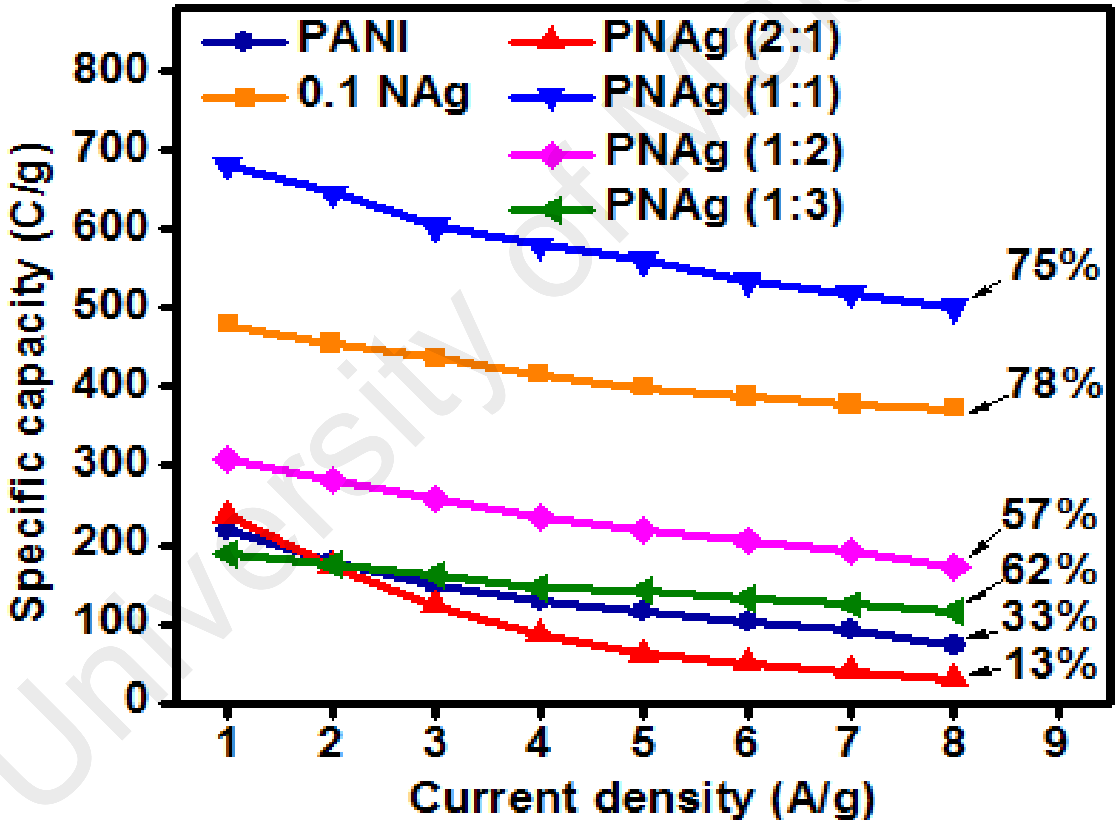

Figure 4.46: Specific capacity of PANI, 0.1 NAg, PNAg (2:1), PNAg (1:1), PNAg (1:2) and PNAg (1:3) at different current densities.

The different in specific capacity and rate capability shown by the nanocomposites as compared to PANI indicates that the optimization of weight ratio between PANI and 0.1

NAg is crucial to get significant boosted performance. Referring to the significantly high specific capacity and rate capability shown by PNAg (1:1), 1:1 is the appropiate ratio between PANI and 0.1 NAg in the nanocomposite. It is also can be understood that eventhough PANI is conductive and also stores charge via faradaic reaction, the redox sites in the PANI backbone are not adequate for the high number of redox reactions in alkaline electrolyte.

4.4.6.3 EIS

The Nyquist plots of PANI, PNAg (2:1), PNAg (1:1), PNAg (1:2) and PNAg (1:3) obtained from EIS analysis were shown in Figure 4.47. As plotted in Figure 4.47 (inset), PNAg (1:1) exhibited the lowest ESR than other samples with the value of 0.68 Ω. The ESR values of PANI, PNAg (2:1), PNAg (1:2) and PNAg (1:3) are 0.97, 0.92, 0.96 and 0.81 Ω, respectively. This typifies that among PNAg nanocomposites, PNAg (1:1) has the highest electrical conductivity. Moreover, PNAg (1:1) displayed the smallest diameter and the most vertical W_d curve, deciphering it has low charge transfer resistance (R_{ct}) and high capacitive behaviour. Referring to the CV, GCD and EIS results, the boosted electrochemical performance of PNAg (1:1) as compared to PANI and 0.1 NAg nanocomposites can be explained by several possible reasons;

(i) Upon the introduction of PANI with 0.1 NAg nanocomposite, PANI acts as a connective layer for 0.1 NAg nanocomposite and thus, unifies the involvement of PANI, Ag_3O_4 and 0.1 NAg during redox process. Besides the charge storage that happen at 0.1 NAg nanocomposite electrode (the mechanism was elaborated under Section 4.2.6), PANI plays its role as well. The branched-like PANI endows a wide spaces for the deposition of 0.1 NAg particles on its surface which can shorten the pathway for the OH^- diffusion through its porous layer (Mantri & Vaidya, 2014).

(ii) The coordination between PANI and 0.1 NAg nanocomposite modifies their electronic conductivity and stimulates more charge transfer (resulted from redox reaction) from the electrode material to the Ni foam.

(iii) The higher specific capacity of PNAg nanocomposites over 0.1 NAg is also contributed from the participation of PANI during redox reaction. As displayed in Figure 4.41, PANI presented two steps of redox transition during charge-discharge process is having more electron transfer (Liu et al., 2013).

(iv) PANI which is highly flexible in nature can easily covers the surface of Ni foam. This reduces the electron transfer resistance between the Ni foam and 0.1 NAg nanocomposite (Maiti & Khatua, 2013).

Therefore, it can be deduced that the huge enhancement in the performance of PNAg (1:1) was attributed to the contributions of all components in the PNAg (1:1) nanocomposite. Figure 4.47 illustrates the schematic illustration of PNAg nanocomposite electrode.

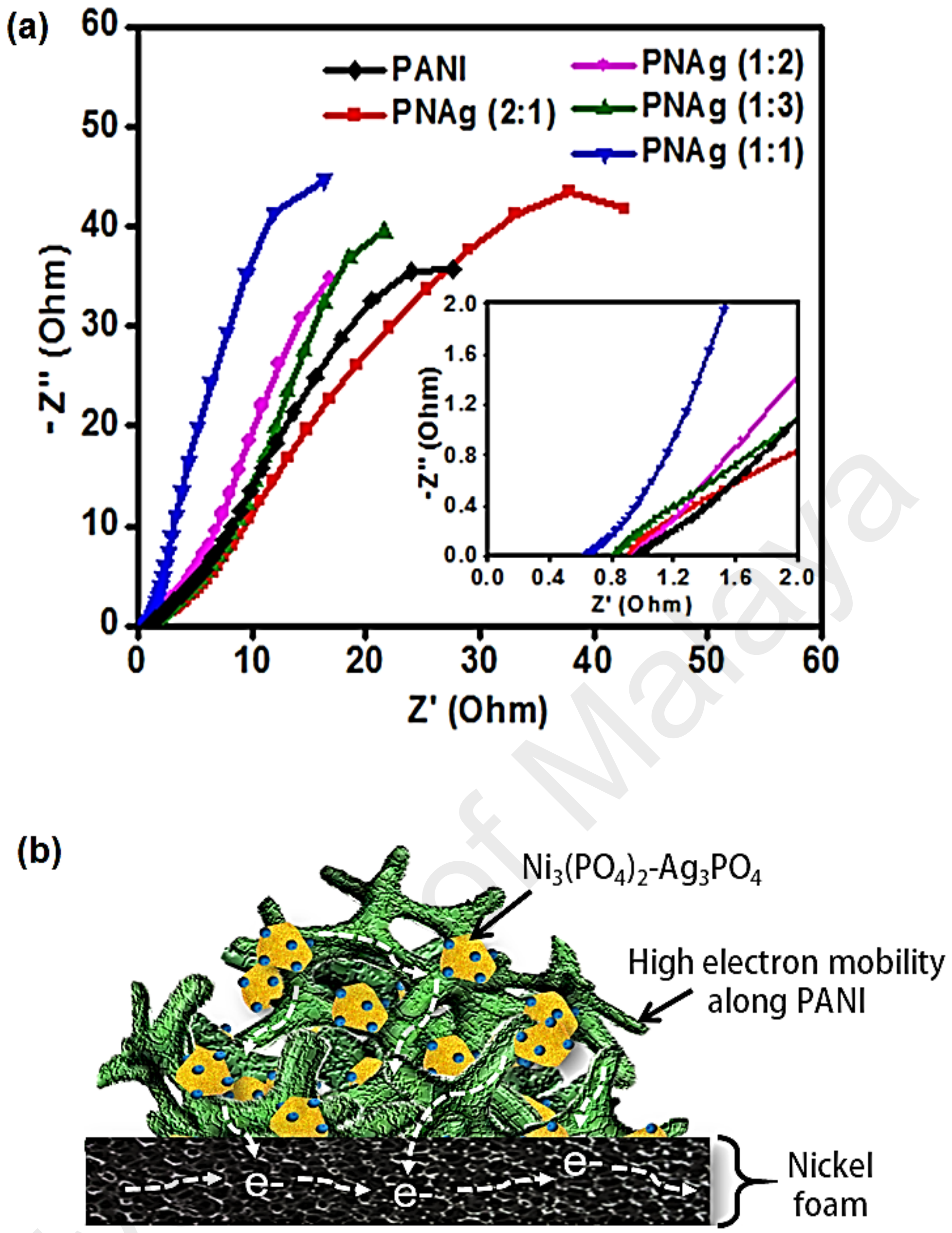

Figure 4.47: (a) Nyquist plots of PANI, PNAg (2:1), PNAg (1:1), PNAg (1:2) and PNAg (1:3); (b) schematic illustration of PNAg electrode.

4.4.7 Electrochemical studies (Two-electrode cell)

Figure 4.48(a) and Figure 4.48(b) show the CVs of PNAg (1:1)//AC measured at different scan rates (5 - 100 mV/s) and the GCD curves that was measured at different current densities (0.5 - 8 A/g) within the potential range of 0 - 1.6 V. 1.6 V has been chosen as the fixed potential window because of the summation of separated stable potential window of AC (from 0 to -1 V) and PNAg (1:1) (from 0 to 0.6 V) electrodes. Based on the figures, the CV shape is well maintained from lower to higher scan rates and the GCD curves were almost symmetric at all current densities. This signifies that PNAg (1:1) has good rate capability. Like other systems, the CV and GCD curves are non-linear due to the influence of faradaic reaction from PNAg (1:1) nanocomposite. In addition, the redox peaks are broad indicates the energy is store by the simultaneous electrostatic and faradaic reaction of AC and PNAg (1:1) electrodes, respectively. Figure 4.48(c) plotted the calculated specific capacity based on GCD with the maximum specific capacity of 175 C/g at 0.5 A/g. The specific capacity retained to 64 % when the current density increased from 0.5 to 8 A/g. This value is higher than that of N300//AC (37 %) and 0.1 NAg//AC (60 %) which clarifies that the rate capability of supercapattery is strongly dependent on the electrical conductivity of electrode materials.

Figure 4.48(d) exhibited the stability of the device over 5000 cycles of charge and discharge process. The capacity percentage was slightly increased to 102 % for the first 600 cycles attributed to the improvement of the electrode surface wettability and progressive activation of the electrode material (Veerasubramani et al., 2016). The capacity degraded gradually to 88 % after 5000 cycles which can be ascribed to the deterioration of PNAg (1:1) stability. As the cycle number increases, the repeated OH^- intercalation and de-intercalation process during the operation of the supercapattery can cause to the frequent volume changes (swelling and shrinking) and delamination of PNAg (1:1). However, the stability of the PNAg (1:1)//AC is still higher than the other fabricated supercapatteries which indicated that PANI has improved the cyclic stability of 0.1 NAg//AC (Zequine et al., 2016).

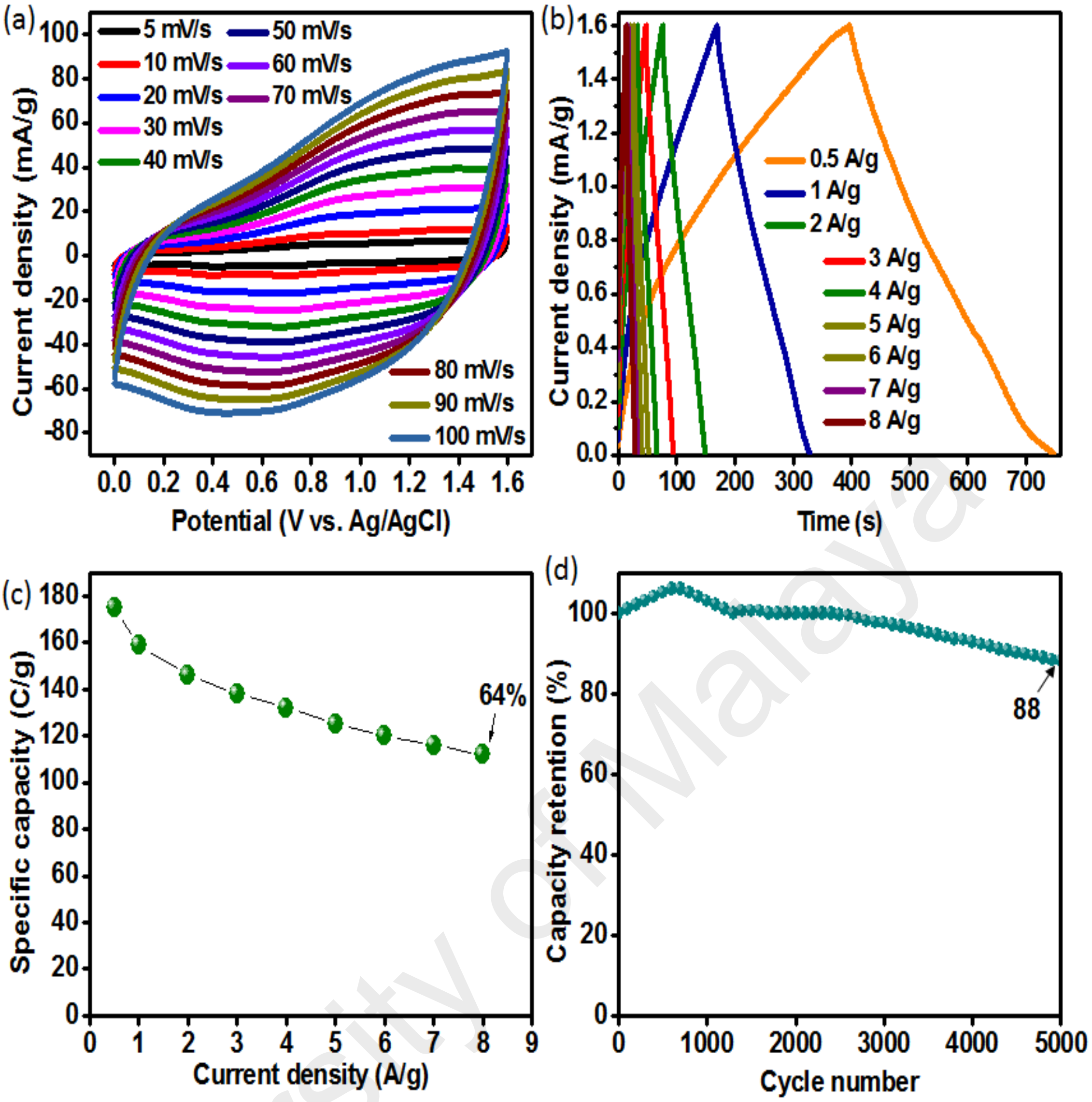

Figure 4.48: (a) CV curves of PNAg (1:1)//AC measured at different scan rates; (b) GCD curves of PNAg (1:1)//AC at different current densities; (c) the calculated specific capacity versus current density; (d) the cylic stability over 5000 cycles.

CHAPTER 5: COMPARISON OF FOUR DIFFERENT SYSTEMS

This chapter is divided into two parts in which the first part includes the comparison of the performance of three different $Ni_3(PO_4)_2$ based electrode materials. In the second part, the electrochemical performance of PANI-$ZnCo_2O_4$ and PNAg (1:1) are compared.

5.1 Comparison between N300, 0.1 NAg and PNAg (1:1)

Figure 5.1 shows the CV (at scan rate of 30 mV/s) and GCD (at current density of 1 A/g) of N300, 0.1 NAg and PNAg (1:1) measured via single electrode measurement. The results in CV measurement (Figure 5.1a) displays the area enclosed by the CV curve and redox peaks intensity increase in this order: N300 < 0.1 NAg < PNAg (1:1). Similarly, GCD graph (Figure 5.1b) shows the discharge curves at the low current density (1 A/g) increase in the order of 0.1 NAg < N300 < PNAg (1:1). However the discharge curves at the high current density (8 A/g) (at Figure 5.1b (inset)) increase in the order of N300 < 0.1 NAg < PNAg (1:1).

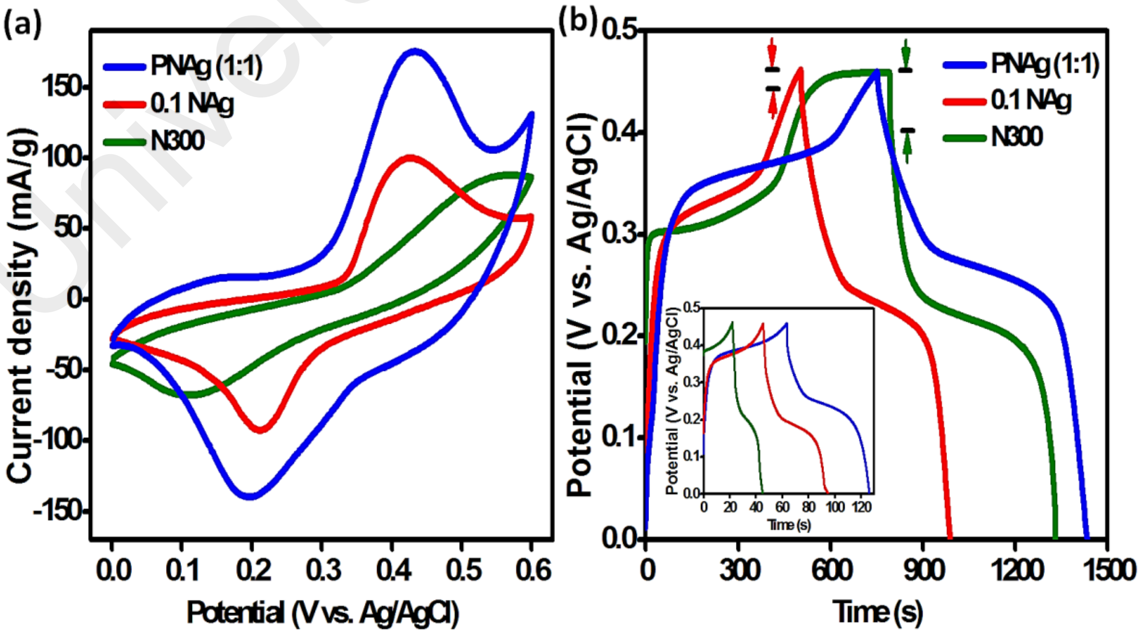

Figure 5. 1 (a) CV and (b) GCD of N300, 0.1 NAg and PNAg (1:1).

It is obvious to observe that N300 showed almost saturation charging towards 0.46 V whereas 0.1 NAg and PNAg (1:1) exhibited almost symmetrical shape of GCD curve. This signifies that the operating potential window for N300 is supposed to be smaller than the other electrodes caused by its low electrical conductivity. In addition, N300 has the largest IR_{drop} as compared to 0.1 NAg and PNAg (1:1) as indicated by the arrow. The IR_{drop} can be related to the energy desipation during the flow of electron that is caused by the internal resistance of the electrode material. In this case, the high IR drop of N300 electrode means the electron transfer between N300 and Ni foam is hindered due to the low electrical conductivity of N300.

The different levels in conductivity of N300, 0.1 NAg and PNAg (1:1) can be supported by the Nyquist plot as shown in Figure 5.2. N300 displayed the highest ESR value and the largest semicircle in comparison with N300 and 0.1 NAg. Whereas PNAg (1:1) exhibited the lowest ESR value, the smallest semicircle and the most verticle W_d line. These observations enough to prove that the incorporation of PANI and Ag_3PO_4 improved the electrical properties of the host N300. The enhancement in electronic conductivity shown by PNAg (1:1) is suggestive of the rapid ion intercalation, larger surface area and shorter pathway for charge mobility which give rise to low internal resistance, good ionic contact and augmented redox reactions. This is undoubtedly contributed from the high redox active sites and conductive nature of both PANI and Ag_3PO_4 nanoparticles that lead to high specific capacity of PNAg (1:1) with a wide working potential window.

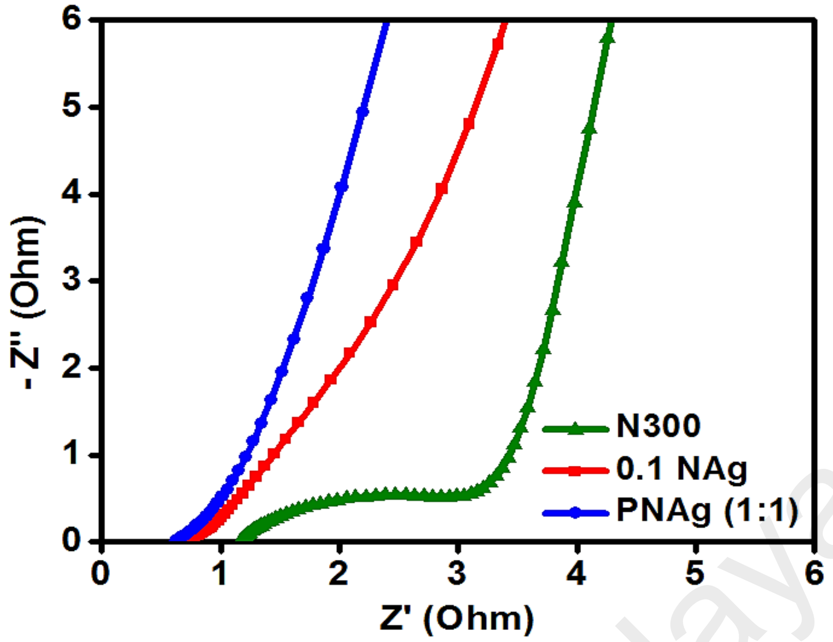

Figure 5.2: Nyquist plots of N300, 0.1 NAg and PNAg (1:1).

Figure 5.3 compares the calculated specific capacity of N300, 0.1 NAg and PNAg (1:1) from the GCD analysis and the rate capability. It is explicitely perceived that PNAg (1:1) augmented the specific capacity of N300 and 0.1 NAg at all curent densities. N300 exhibited higher specific capacity at low current rate. However, at high current rate, the specific capacity of 0.1 NAg is higher than N300 which indicates the low rate capability of N300. As explained in the previous section, the porous structure of amorphous N300 is inadequate to retain its high specific capacity at high current density. This is attributed to the some interior surfaces of N300 that could not be accessed by the electrolyte at a high current rate, thus caused to low specific capacity. Furthermore, N300 has low electrical conductivity which impeded the transfer of electrons. While for 0.1 NAg, the presence of Ag_3PO_4 nanoparticles able to maintain the rate capability due to its crystalline structure and higher electrical conductive than N300. PNAg (1:1) exhibited higher specific capacity than N300 and 0.1 NAg at all current densities. The introduction of PANI to 0.1 NAg enhanced the electrical conductivity of 0.1 NAg and facilitated the charge transfer kinetic towards the Ni foam. Moreover, PANI also participated during faradaic reaction with electrolyte attributed to the existence of its different oxidation states.

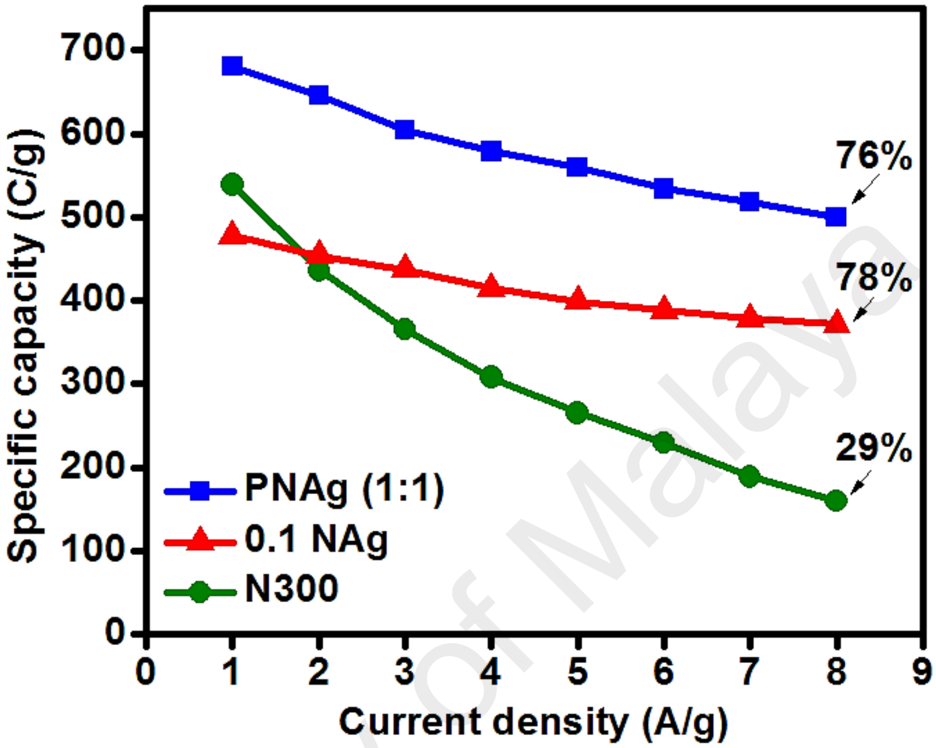

Figure 5.3: The comparison in rate capability between N300, 0.1 NAg and PNAg (1:1) electrodes.

The energy densities and power densities of the fabricated devices (N300//AC, 0.1 NAg//AC and PNAg (1:1)//AC) are provided in Ragone plot as shown in Figure 5.4. The energy densities of all devices decreased slowly with increasing of power densities. Especially for N300//AC, the energy density reduced drastically versus power densities which is due to its low electrical conductivity. The location of PNAg (1:1)//AC at the top of the graph indicates that at constant power density, it has the highest energy storage as compared to 0.1 NAg//AC and N300//AC. The improvement in energy density is due to the minimization of inner resistance in the presence of PANI where it provides conductive pathway to Ni foam. The highest energy density delivered by PNAg (1:1) was 38.9 Wh/kh at 400 W/kg, which is superior than 0.1 NAg//AC (32.4 Wh/kg at 399.5 W/kg) and N300//AC (33.3 Wh/kg at 39.6 W/kg).

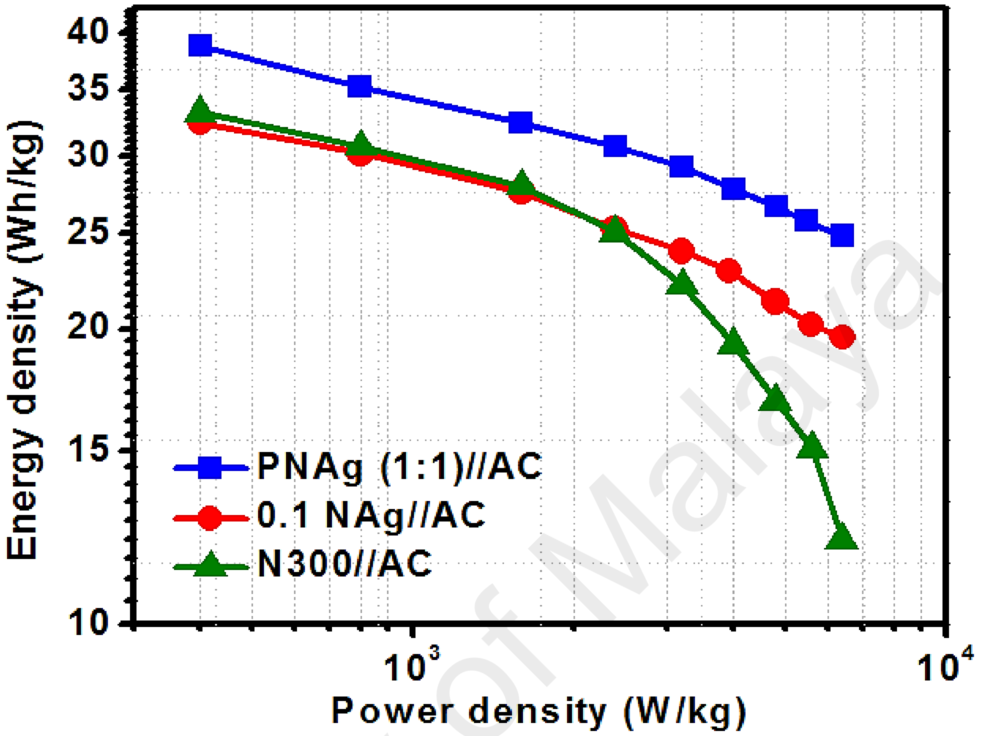

Figure 5.4: Ragone plot of N300//AC, 0.1 NAg//AC and PNAg (1:1)//AC.

The practical implementation of supercapattery stongly depends upon prolong cycling stability which has been verified up to 3000 cycles (for N300//AC) and 5000 cycles (for 0.1 NAg//AC and PNAg (1:1)//AC) at the current density of 1 A/g (Figure 5.5). There was an increase of specific capacity at the beginning of few cycles due to the activation process of the devices. But as the cycling cumber increases, the specific capacity of N300//AC was drop to 72 % at 3000th cycle. On the other hand, the specific capacity of 0.1 NAg//AC and PNAg (1:1)//AC was still stable and reached to 82 % and 88 % capacity retention at 5000th cycle, respectively. Thereby, from these results, it can be concluded that the nanoengineering of electrode material isimportant as it plays a major contribution to the performance of the supercapattery.

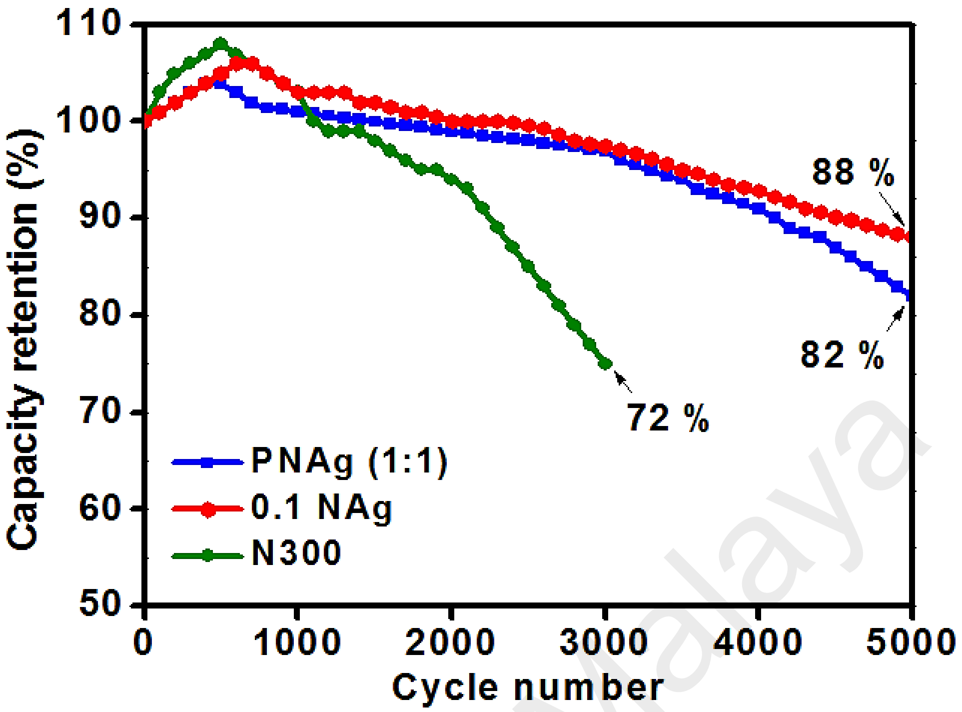

Figure 5.5: Cyclic stability of N300//AC, 0.1 NAg//AC and PNAg (1:1)//AC.

5.2 Comparison between PNAg (1:1) and PANI-$ZnCo_2O_4$

Generally, it is accepted that high concentration of electrolyte contributes to higher amount of ions to involve in faradaic reaction for high performance of supercapacitor. Figure 5.6a and Figure 5.6b depict a comparison of the CV and GCD curves of PANI-$ZnCo_2O_4$ and PNAg (1:1). Based on the figures, it is obvious that PNAg (1:1) has exhibited better parformance than PANI-$ZnCo_2O_4$ even the concentration of KOH electrolyte used for PNAg (1:1) is lower (1 M KOH) than that of PANI-$ZnCo_2O_4$ (2 M KOH). The CV potential window for PNAg (1:1) is 0 - 0.6 V, which is larger than PANI-$ZnCo_2O_4$ (0 - 0.5 V). Likewise for GCD curves, PNAg (1:1) can be fully charged to maximum potential of 0.46 V, which is higher than that of PANI-$ZnCo_2O_4$ (maximum potential of 0.38 V).

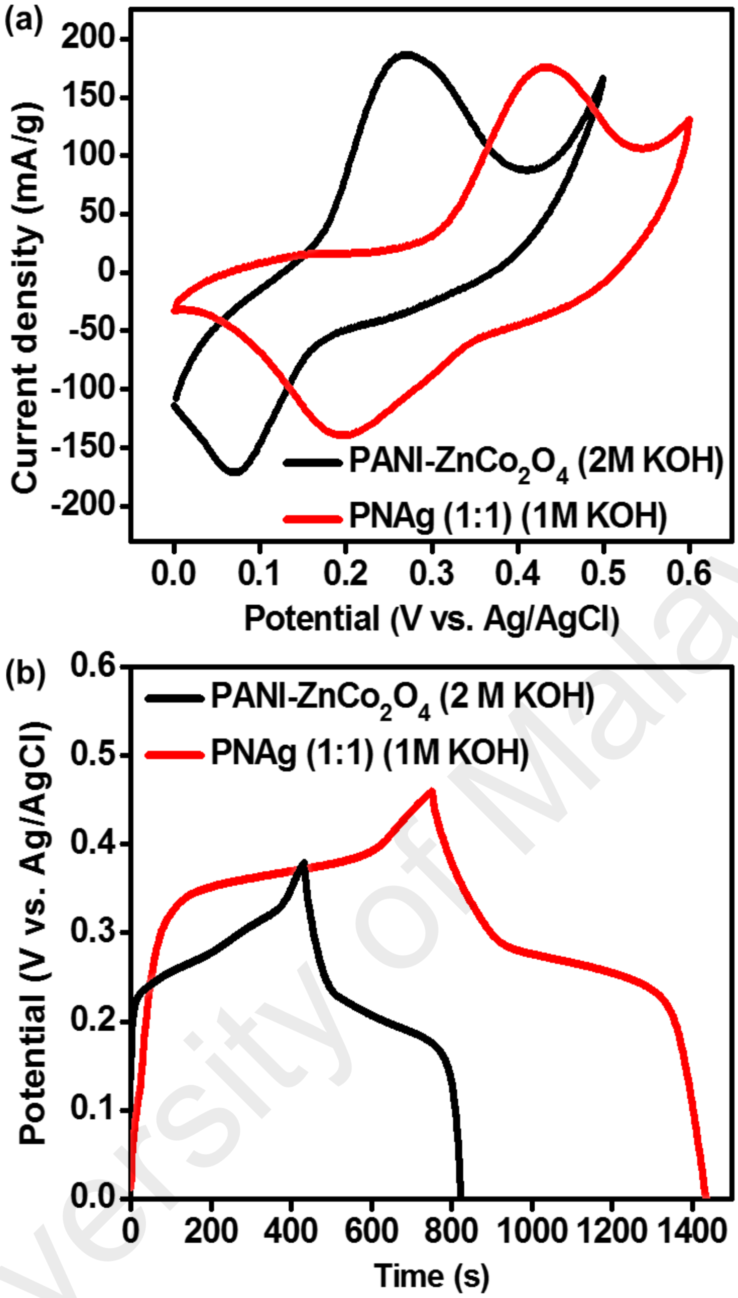

Figure 5.6: The comparison between CV and (b) GCD curves of PANI-ZnCo$_2$O$_4$ (in 2 M KOH) and PNAg (1:1) (in 1 M KOH).

The expanded operating potential window achieved by PNAg (1:1) as compared to PANI-ZnCo$_2$O$_4$ can be ascribed mainly due to the porosity of the nanoparticles (i.e. 0.1 NAg and ZnCo$_2$O$_4$). The porosity of electrode materials accounts for the increased specific surface area, which enhanced the electrolyte peneration and effectively migitated the relaxation time for the electrode, resulting in a high electrochemical performance.

PNAg (1:1) contains highly porous of amorphous N300 which can endow large number of active diffusion channels for electrolyte ions during charging-discharging process and increase faradaic reaction. For PANI-$ZnCo_2O_4$, eventhough it also comprises porous structure contributed from the partially amorphous structure of PANI, the number of pores is considerably insufficient and the size of the pores is relatively smaller than N300.

The incorporation of a proper electrical conductive component into nanoparticles also is important. Besides PANI which has delocalization of electron in a continuosly overlapped π-conjugated electron system, PNAg (1:1) contain Ag_3PO_4 nanoparticles which can also act as a charge transfer medium. In PANI-$ZnCo_2O_4$, eventhough $ZnCo_2O_4$ is a combination of two metal ions (Zn and Co), its electrical conductivity is still lower than Ni_3PO_4-Ag_3PO_4 (0.1 NAg). This has been proved by EIS analysis in which the ESR value and diameter of semicircle (R_{ct}) of 0.1 NAg is smaller than those of $ZnCo_2O_4$. Another advantage of 0.1 NAg is it has strong P–O covalent bonds which make it chemically stable and able to retain its high specific capacity from low to high current rate.

CHAPTER 6: CONCLUSION AND FUTURE WORK

6.1 Conclusion

This research targets on the development of PANI-based nanocomposites for supercapattery application via modulating their properties and morphology. To achieve this target, different parameter such as size, crystallinity and electrical conductivity of nanoparticles have been initially explored as presented in System 1, System 2 and System 3. The electrochemical performance of nanoparticles was further improved by the incorporation of PANI to form nanocomposite. The synthesized samples were characterized comprehensively via different analysis techniques; XRD, FTIR, XPS, FESEM-EDX and HRTEM.

System 1 demonstrated the performance of PANI, $ZnCo_2O_4$ and PANI-$ZnCo_2O_4$ nanocomposite. $ZnCo_2O_4$ is synthesized through hydrothermal method and was physically blended with PANI (synthesized through oxidation polymerization method) to form binary nanocomposite of PANI-$ZnCo_2O_4$. FESEM images showed that the $ZnCo_2O_4$ nanoparticles were anchored along tubular PANI which proved the blending method able to incorporate $ZnCo_2O_4$ with PANI. PANI-$ZnCo_2O_4$ nanocomposite exhibited the maximum specific capacity of 398 C/g (57 % retention) which is higher than PANI (380 C/g with 15 % retention) and $ZnCo_2O_4$ (138 C/g with 35 % retention) at a current density of 1 A/g. This enhancement arose from the augmentation of redox sites and the synergistic effect of PANI and $ZnCo_2O_4$ which caused improvement in the effective charge transportation. Eventhough PANI-$ZnCo_2O_4$ has shown improved electrochemical performance, the obtained specific capacity and potential window (0 - 0.5 V) are considerably small. Thus, the work was proceed with the change of nanoparticles i.e. metal phosphate.

System 2 highlights on the synthesis of different size, structure and morphology of $Ni_3(PO_4)_2$ (N300, N600 and N900) through sonochemical and subsequent calcination at different temperatures. Through XRD and FESEM analysis, the calcination temperature was highly influence the growth of $Ni_3(PO_4)_2$. As calcination temperature increases, the structure changed from amorphous to crystalline phase and the particles size became bigger and aggregated. N300 displayed the highest specific capacity (539 C/g) at 1 A/g in 1 M KOH as compared to N600 (203 C/g) and N900 (66 C/g). This is attributed to the amorphicity, smaller size and fewer agglomeration of N300 which provided high number of channels for ion accessibility. Nonetheless, N300 renders the lowest rate capability when the current density increased from 1 to 8 A/g with 29 % capacity retention. This is caused by its poor electrical conductivity and unaccessed of some interior surfaces by electrolyte ions at high current rate.

The performance of N300 was improved by the incorporation of crystalline Ag_3PO_4 nanoparticles as presented in System 3. Different weight ratios of N0:$AgNO_3$ were prepared using the same method with the fixed calcination temperature of 300 °C, and all the prepared samples were labelled as 0.05 NAg, 0.1 NAg, 0.2 NAg and 0.3 NAg. The morphological studies revealed that the crystalline structure of Ag_3PO_4 (~8 nm) was intimately anchored on the surface of N300 which is beneficial for the efficient charge transfer between the two metal phosphates. The optimized $Ni_3(PO_4)_2$-Ag_3PO_4 nanocomposite (0.1 NAg) electrode exhibited significantly boosted rate capability from 29 % (N300) to 78 % capacity retention with the maximum specific capacity of 478 C/g at 1 A/g in 1 M KOH. The enhancement of rate capability was due to the rapid electrons transfer rate and the augmentation of electroactive sites contributed from both amorphous N300 and conductive Ag_3PO_4. In addition, the crystalline structure of Ag_3PO_4 maintains the occurance of redox reaction by endowing additional surface area to the unutilized surfaces of N300 at high current rate. Unfortunately, N300 still surpassed 0.1 NAg at low current rate which led to System 3.

In System 4, 0.1 NAg was composited with conductive PANI to more enhance its electrical conductivity and electrochemical performance. Different ratios of PANI:0.1 NAg (named as PNAg (2:1), PNAg (1:1), PNAg (1:2) and PNAg (1:3)) were synthesized through physical blending method. XRD revealed the formation of the oxidized Ag with the increment of PANI and this was supported by XPS analysis. Among the samples, PNAg (1:1) exhibited the highest specific capacity from 1 to 8 A/g with the maximum value of 677 C/g (75 % capacity retention at 8 A/g). The enhancement in electrochemical performance can be ascribed to the porous layer of PANI which facilitates the electrolyte ions transport kinetics. Besides, the conductive PANI is flexible which can easily covers the surface of Ni foam, reducing the interfacial resistance between Ni foam and 0.1 NAg.

In overall, the influence of size, crystallinity, number of redox reaction, electrical conductivity and stability of electrode material are highly important for achieving high specific capacity and fast charge-discharge process. The efforts discussed in this thesis might give an insight on the development of new and compatible materials for not only electrode, but also electrolyte. However, deep understanding on nano-architecture and surface chemistry of electrode materials are still essential to improve the performance of energy storage devices. Metal phosphate with the open structure framework and rich redox behaviour, can hold great promise as electrode materials for supercapattery.

6.2 Future work

In this research, non-conductive PVDF has been used as the binder for adhering the electrode materials slurry on the nickel foam and retains the mechanical stability of the electrode. However, this practice is actually detrimental for electrode ion transportation and can cause to poor rate capability of devices. PVDF does not involve in faradaic reaction with electrolyte and hinders the charge storage. In addition, it is non-conductive which can increase the internal resistance of electrode and build an addition interfaces between the electron pathways. Hence, binder-free electrode, namely, self-supported electrode can be fabricated by growing the nanomaterials directly on conductive substrate. This can eliminates the adverse effects of slurry coating during electrode fabrication. Therefore, further research work will be conducted by growing nanomaterial on porous conductive substrate such as Ni foam and carbon cloth. This preparation will be done towards synthesis of nanocomposites comprising different metal compounds (phosphate, sulphide, carbonate etc.) and different conducting materials (PANI, graphene and CNT) by electrochemical deposition and hydrothermal method. The fabricated electrode will be characterized and tested for supercapacitors and electrochemical sensors.

REFERENCES

Aaddane, A., Kacimi, M., & Ziyad, M. (2001). Oxidative dehydrogenation of ethane and propane over magnesium-cobalt phosphates $Co_xMg_{3-x}(PO_4)_2$. *Catalysis Letters, 73,* 47-53.

Aliev, S. B., Samsonenko, D. G., Maksimovskiy, E. A., Fedorovskaya, E. O., Sapchenko, S. A., & Fedin, V. P. (2016). Polyaniline-intercalated MIL-101: selective CO_2 sorption and supercapacitor properties. *New Journal of Chemistry*, *40*(6), 5306-5312.

Amarnath, C. A., Venkatesan, N., Sawant, Doble, M., & Sawant, S., N. (2014). Water dispersible Ag@polyaniline-pectin as supercapacitor electrode for physiological environment. *Journal of Materials Chemistry B*, *2,* 5012-5019.

Bagotsky, V. S., Skundin, A. M., & Volfkovich, Y. M. (2015). *Electrochemical power sources: batteries, fuel cells, and supercapacitors*. John Wiley & Sons.

Bajaj, R., Sharma, M., & Bahadur, D. (2013). Visible light-driven novel nanocomposite ($BiVO_4/CuCr_2O_4$) for efficient degradation of organic dye. *Dalton Transactions, 42*(19), 6736-6745.

Balakrishnan, A., & Subramanian, K. R. V. (Eds.). (2014). *Nanostructured ceramic oxides for supercapacitor applications*. CRC Press.

Benedek, P., Wenzler, N., Yarema, M., & Wood, V. C. (2017). Low temperature hydrothermal synthesis of battery grade lithium iron phosphate. *RSC Advances*, *7,* 17763-17767.

Berzina, C. L., & Borodajenko, N. (2012). Research of calcium phosphates using Fourier transform infrared spectroscopy. In *Infrared Spectroscopy-Materials Science, Engineering and Technology*. InTech.

Boruah, B. D., & Misra, A. (2016). A flexible ternary oxide based solid-state supercapacitor with excellent rate capability. *Journal of Materials Chemistry A*, *4*(44), 17552-17559.

Brousse, T., & Daniel, B. (2015). To Be or Not To Be Pseudocapacitive?. *Journal of the Electrochemical Society*, *162*(5), 5185-5189.

Cai, X., Cui, X., Zu, L., Zhang, Y., Lian, H., Liu, Y., & Wang, X. (2017). Ultra high electrical performance of nano nickel oxide and polyaniline composite materials. *Polymers*, *9*(7), 288-302.

Canobre, S. C., Xavier, F. F. S., Fagundes, W. S., De Freitas, A. C., & Amaral, F. A. (2015). Performance of the chemical and electrochemical composites of PPy/CNT as electrodes in type I supercapacitors. *Journal of Nanomaterials*, *16(1)*, 1-10.

Chen, C., Li, X., Deng, F., & Li, J. (2016). Electropolymerization and electrochemical behavior of nickel schiff base complexes with different groups between imine linkages. *RSC Advances*, *6*(83), 79894-79899.

Chen, G. Z. (2017). Supercapacitor and supercapattery as emerging electrochemical energy stores. *International Materials Reviews, 62*(4), 173-202.

Chen, L. Y., Kang, J. L., Hou, Y., Liu, P., Fujita, T., Hirata, A., & Chen, M. W. (2013). High-energy-density nonaqueous MnO_2@nanoporous gold based supercapacitors. *Journal of Materials Chemistry A, 1*(32), 9202-9207.

Chen, W., Tao, X., Wei, D., Wang, H., Yu, Q., & Li, Y. (2016). High-performance supercapacitor based on actived carbon-MnO_2-polyaniline composite. *Journal of Materials Science: Materials in Electronics, 27*, 1357-1362.

Chen, X., Li, C., Grätzel, M., Kostecki, R., & Mao, S. S. (2012). Nanomaterials for renewable energy production and storage. *Chemical Society Reviews, 41*(23), 7909-7937.

Chong, R., Wang, B., Li, D., Chang, Z., & Zhang, L. (2017). Enhanced photoelectrochemical activity of nickel-phosphate decorated phosphate-Fe_2O_3 photoanode for glycerol-based fuel cell. *Solar Energy Materials and Solar Cells*, *160*, 287-293.

Combes, C., & Rey, C. (2010). Amorphous calcium phosphates: synthesis, properties and uses in biomaterials. *Acta Biomaterialia, 6*, 3362-3378.

Dey, A., Kaushik, A., Arya, S. K., & Bhansali, S. (2012). Mediator free highly sensitive polyaniline-gold hybrid nanocomposite based immunosensor for prostate-specific antigen (PSA) detection. *Journal of Materials Chemistry*, *22*(29), 14763-14772.

Deyab, M. A., Eddahaoui, K., Essehli, R., Benmokhtar, S., Rhadfi, T., De Riccardis, A., & Mele, G. (2016). Influence of newly synthesized titanium phosphates on the corrosion protection properties of alkyd coating. *Journal of Molecular Liquids*, *216*, 699-703.

Ding, J., Li, X., Wang, X., Zhang, J., Yu, D., & Qiu, B. (2015). Fabrication of vertical array CNTs/polyaniline composite membranes by microwave-assisted in situ polymerization. *Nanoscale Research Letters, 10*(1), 493-512.

Djurisic, A. B., Xi, Y. Y., Hsu, Y. F., & Chan, W. K. (2007). Hydrothermal synthesis of nanostructures. *Recent Patents on Nanotechnology*, *1*(1), 121-128.

Duraisamy, N., Numan, A., Fatin, S. O., Ramesh, K., & Ramesh, S. (2016). Facile sonochemical synthesis of nanostructured NiO with different particle sizes and its electrochemical properties for supercapacitor application. *Journal of Colloid and Interface Science, 471*, 136-144.

Duraisamy, N., Numan, A., Ramesh, K., Choi, K. H., Ramesh, S., & Ramesh, S. (2015). Investigation on structural and electrochemical properties of binder free nanostructured nickel oxide thin film. *Materials Letters, 161*, 694-697.

Durif, A. (2013). *Crystal chemistry of condensed phosphates*. Springer Science & Business Media.

Durif, A. (2005). The development of cyclophosphate crystal chemistry. *Solid State Sciences*, *7*, 760-766.

Dutta, A., & Datta, J. (2014). Energy efficient role of Ni/NiO in PdNi nano catalyst used in alkaline DEFC. *Journal of Materials Chemistry A*, *2*(9), 3237-3250.

Eftekhari, A., Li, L., & Yang, Y. (2017). Polyaniline supercapacitors. *Journal of Power Sources*, *347*, 86-107.

Fang, Y., Zhang, J., Xiao, L., Ai, X., Cao, Y., & Yang, H. (2017). Phosphate framework electrode materials for sodium ion batteries. *Advanced Science*, *4*(5), 1-21.

Gao, Z., Wang, X., Chang, J., Wu, D., Wang, L., Liu, X., & Jiang, K. (2015). Fluorescent carbon quantum dots, capacitance and catalysis active porous carbon microspheres from beer. *RSC Advances*, *5*, 48665-48674.

Garg, N., Basu, M., & Ganguli, A. K. (2014). Nickel cobaltite nanostructures with enhanced supercapacitance activity. *The Journal of Physical Chemistry C*, *118*(31), 17332-17341.

González, A., Goikolea, E., Barrena, J. A., & Mysyk, R. (2016). Review on supercapacitors: technologies and materials. *Renewable and Sustainable Energy Reviews*, *58*, 1189-1206.

Gu, C., Ge, X., Wang, X., & Tu, J. (2015). Cation-anion double hydrolysis derived layered single metal hydroxide superstructures for boosted supercapacitive energy storage. *Journal of Materials Chemistry A*, *3*, 14228-14238.

Guan, H., Fan, L. Z., Zhang, H., & Qu, X. (2010). Polyaniline nanofibers obtained by interfacial polymerization for high-rate supercapacitors. *Electrochimica Acta*, *56*, 964-968.

Guillou, N., Gao, Q., Forster, P. M., Chang, J. S., Nogueaǹds, M., Park, S. E., & Cheetham, A. K. (2001). Nickel (II) phosphate VSB-5: a magnetic nanoporous hydrogenation catalyst with 24-ring tunnels. *Angewandte Chemie - International Edition*, *40*(15), 2831-2834.

Guo, X., Yan, H., Zhao, S., Li, Z., Li, Y., & Liang, X. (2013). Effect of calcining temperature on particle size of hydroxyapatite synthesized by solid-state reaction at room temperature. *Advanced Powder Technology*, *24*(6), 1034-1038.

Han, G., Liu, Y., Zhang, L., Kan, E., Zhang, S., Tang, J., & Tang, W. (2014). MnO_2 nanorods intercalating graphene oxide/polyaniline ternary composites for robust high-performance supercapacitors. *Scientific Reports*, *4*, 4824.

Hashimoto, K., Toda, Y., Miura, K., & Hashimoto, K. (1994). Synthetic process and thermal behavior of nickel hydrogen phosphate hydrate prepared by a wet chemical method. *Journal of the Japan Society of Colour Material*, *67*, 614-623.

He, X., Liu, G., Yan, B., Suo, H., & Zhao, C. (2016). Significant enhancement of electrochemical behavior by incorporation of carboxyl group functionalized carbon nanotubes into polyaniline based supercapacitor. *European Polymer Journal*, *83*, 53-59.

Hu, N., Zhang, L., Yang, C., Zhao, J., Yang, Z., Wei, H., & Xu, Z. J. (2016). Three-dimensional skeleton networks of graphene wrapped polyaniline nanofibers: an excellent structure for high-performance flexible solid-state supercapacitors. *Scientific Reports*, *6*, 19777.

Huang, K., Yuan, L., & Feng, S. (2015). Crystal facet tailoring arts in perovskite oxides. *Inorganic Chemistry Frontiers*, *2*(11), 965-981.

Jiang, G., Zhang, M., Li, X., & Gao, H. (2015). $NiMoO_4$@$Ni(OH)_2$ core/shell nanorods supported on Ni foam for high-performance supercapacitors. *RSC Advances*, *5*(85), 69365-69370.

Julien, C. M., & Massot, M. (2004, September). Vibrational spectroscopy of electrode materials for rechargeable lithium batteries III oxide frameworks. In *Proceedings of the International Workshop Advanced Techniques for Energy Sources Investigation and Testing* (pp. 1-17).

Kaspar, T. C., Droubay, T., Chambers, S. A., & Bagus, P. S. (2010). Spectroscopic evidence for Ag (III) in highly oxidized silver films by x-ray photoelectron spectroscopy. *The Journal of Physical Chemistry C*, *114*, 21562-21571.

Khan, W. S., Hamadneh, N. N., & Khan, W. A. (2017). *Techniques, classification and properties*: *in science and applications of tailored nanostructures*. One Central Press (OCP).

Kuang, H., Cao, Q., Wang, X., Jing, B., Wang, Q., & Zhou, L. (2013). Influence of the reaction temperature on polyaniline morphology and evaluation of their performance as supercapacitor electrode. *Journal of Applied Polymer Science*, *130*(5), 3753-3758.

Kumar, V. A., Nakajima, Y., Uchida, T., Hanajiri, T., & Maekawa, T. (2016). Synthesis of nanoparticles composed of silver and silver chloride for a plasmonic photocatalyst using an extract from needles of pinus densiflora. *Materials Letters*, *176*(1), 169-172.

Lee, D. J., Scrosati, B., & Sun, Y. K. (2011). $Ni_3(PO_4)_2$-coated $Li[Ni_{0.8}Co_{0.15}Al_{0.05}]O_2$ lithium battery electrode with improved cycling performance at 55°C. *Journal of Power Sources*, *196*(18), 7742-7746.

Li, S., Teng, F., Chen, M., Li, N., Hua, X., Wang, K., & Li, M. (2014). Interesting electrochemical properties of novel three-dimensional Ag_3PO_4 tetrapods as a new supercapacitor electrode material. *Chemical Physics Letters*, *601*, 59-62.

Li, J., Wang, S., Xiao, T., Tan, X., Xiang, P., Jiang, L., & Li, M. (2017). Controllable preparation of nanoporous Ni_3S_2 films by sulfuration of nickel foam as promising asymmetric supercapacitor electrodes. *Applied Surface Science*, *420*, 919-926.

Li, R., Peng, R., Kihm, K. D., Bai, S., Bridges, D., Tumuluri, U., & Hu, A. (2016). High-rate in-plane micro-supercapacitors scribed onto photo paper using in-situ femtolaser-reduced graphene oxide/Au nanoparticle microelectrodes. *Energy &*

Environmental Science, *9*, 1458-1467.

Liu, C., Neale, Z. G., & Cao, G. (2016). Understanding electrochemical potentials of cathode materials in rechargeable batteries. *Materials Today*, *19*(2), 109-123.

Liu, H., Wang, Y., Gou, X., Qi, T., Yang, J., & Ding, Y. (2013). Three-dimensional graphene/polyaniline composite material for high-performance supercapacitor applications. *Materials Science and Engineering B: Solid-State Materials for Advanced Technology*, *178*(5), 293-298.

Liu, L., Annamalai, K. P., & Tao, Y. (2016). A hierarchically porous $CuCo_2S_4$/graphene composite as an electrode material for supercapacitors. *New Carbon Materials, 31*, 336-342.

Liu, Y., Wang, R., & Yan, X. (2015). Synergistic effect between ultra-small nickel hydroxide nanoparticles and reduced graphene oxide sheets for the application in high-performance asymmetric supercapacitor. *Scientific Reports*, *5*, 11095.

Lu, P., Xue, D., Yang, H., & Liu, Y. (2013). Supercapacitor and nanoscale research towards electrochemical energy storage. *International Journal of Smart and Nano Materials*, *4*(1), 2-26.

Ma, L., Shen, X., Ji, Z., Zhu, G., & Zhou, H. (2014). Ag nanoparticles decorated MnO_2/reduced graphene oxide as advanced electrode materials for supercapacitors. *Chemical Engineering Journal*, *252*, 95-103.

Ma, Y., Jia, Y., Wang, L., Yang, M., Bi, Y., & Qi, Y. (2016). Facile synthesis of three-dimensional flower-like MoO_2-graphene nanostructures with enhanced electrochemical performance. *Journal of Materials Chemistry A*, *4*(27), 10414-10418.

Maiti, S., & Khatua, B. B. (2013). Electrochemical and electrical performances of cobalt chloride ($CoCl_2$) doped polyaniline (PANI)/graphene nanoplate (GNP) composite. *RSC Advances*, *3*(31), 12874-12885.

Mantri, K., & Vaidya, I. (2014). Review article surface area: an exploratory tool. *International Journal of Pharmaceutical Archive*, *3*(6), 460-471.

Mao, Y., Li, T., Guo, C., Zhu, F., Zhang, C., Wei, Y., & Hou, L. (2016). Cycling stability of ultrafine β-$Ni(OH)_2$ nanosheets for high capacity energy storage device via a multilayer nickel foam electrode. *Electrochimica Acta*, *211*, 44-51.

Maybodi, A. S., Karim, S., Nejad, H., & Akhoondi, R. (2011). Synthesis and characterization of nickel phosphate nanoparticles and VSB-5 with quaternary ammonium base. *International Nano Letters*, *1*(1), 52-58.

Mena, A. K. M., Amano, Y., & Machida, M. (2016). Ammonium persulfate oxidized activated carbon fiber as a high capacity adsorbent for aqueous Pb(II). *Journal of Environmental Chemical Engineering*, *4*(4), 4644-4652.

Merkus, H. G., & Meesters, G. M. (Eds.). (2013). *Particulate Products: Tailoring Properties for Optimal Performance* (Vol. 19). Springer Science & Business Media.

Meseguer, S., Tena, M. A., Gargori, C., Nadenes, J. A., Llusar, M., & Monros, G. (2007). Structure and colour of cobalt ceramic pigments from phosphates. *Ceramics International, 33*(5), 843-849.

Michael, R. J. V., Sambandam, B., Muthukumar, T., Umapathy, M. J., & Manoharan, P. T. (2014). Spectroscopic dimensions of silver nanoparticles and clusters in ZnO matrix and their role in bioinspired antifouling and photocatalysis. *Physical Chemistry Chemical Physics, 16*(18), 8541-8555.

Minakshi, M., Ralph, D., Blackford, M., & Ionescu, M. (2011). $LiNiPO_4$ aqueous rechargeable battery. *The Electrochemical Society, 35*(32), 281-292.

Molapo, K. M., Ndangili, P. M., Ajayi, R. F., Mbambisa, G., Mailu, S. M., Njomo, N., Maskini, M., Baker, P., & Iwuoha, E. I. (2012). Electronics of conjugated polymers (I): polyaniline. *International Journal of Electrochemical Science, 7,* 11859-11875.

Nagamuthu, S., Vijayakumar, S., & Ryu, K. (2016). Synthesis of Ag anchored Ag_3VO_4 stacked nanosheets : towards a negative electrode material for high performance asymmetric supercapacitor devices material for high performance asymmetric supercapacitor devices abstract. *The Journal of Physical Chemistry, 120,* 18963-18970.

Omar, F. S., Numan, A., Duraisamy, N., Ramly, M. M., Ramesh, K., & Ramesh, S. (2017). Binary composite of polyaniline/copper cobaltite for high performance asymmetric supercapacitor application. *Electrochimica Acta, 227,* 41-48.

Padhi, A. K., Nanjundaswamy, K., & Goodenough, J. B. (1997). Phospho-olivines as positive-electrode materials for rechargeable lithium batteries. *Journal of the Electrochemical Society, 144,* 1188-1194.

Pang, H., Zhang, Y. Z., Run, Z., Lai, W. Y., & Huang, W. (2015). Amorphous nickel pyrophosphate microstructures for high-performance flexible solid-state electrochemical energy storage devices. *Nano Energy, 17,* 339-347.

Patil, D. S., Pawar, S. A., Devan, R. S., Gang, M. G., Ma, Y. R., Kim, J. H., & Patil, P. S. (2013). Electrochemical supercapacitor electrode material based on polyacrylic acid/polypyrrole/silver composite. *Electrochimica Acta, 105,* 569-577.

Peng, C., Hu, D., & Chen, G. Z. (2011). Theoretical specific capacitance based on charge storage mechanisms of conducting polymers: comment on “vertically oriented arrays of polyaniline nanorods and their super electrochemical properties.” *Chemical Communications, 47*(14), 4105-4107.

Philip, B., Xie, J., Abraham, J. K., & Varadan, V. K. (2005). Polyaniline/carbon nanotube composites: starting with phenylamino functionalized carbon nanotubes. *Polymer Bulletin, 53*(2), 127-138.

Pilban, J., S., Pandikumar, A., Goh, B. T., Lim, Y. S., Basirun, W. J., Lim, H. N., & Huang, N. M. (2015). Influence of particle size on performance of a nickel oxide nanoparticle-based supercapacitor. *RSC Advances, 5*(18), 14010-14019.

Poncelet, G., Martens, J., Delmon, B., Grange, P., & Jacobs, P. A. (Eds.).

(1995). *Preparation of Catalysts VI: Scientific Bases for the Preparation of Heterogeneous Catalysts* (Vol. 91). Elsevier.

Pramanik, M., Salunkhe, R. R., Imura, M., & Yamauchi, Y. (2016). Phosphonate-derived nanoporous metal phosphates and their superior energy storage application. *ACS Applied Materials and Interfaces, 8*(15), 9790-9797.

Rajammal, K., Sivakumar, D., Duraisamy, N., Ramesh, K., & Ramesh, S. (2017a). Influences of sintering temperatures and crystallite sizes on electrochemical properties of $LiNiPO_4$ as cathode materials via sol-gel route for lithium ion batteries. *Journal of Sol-Gel Science and Technology*, *83*(1), 12-18.

Rajammal, K., Sivakumar, D., Duraisamy, N., Ramesh, K., & Ramesh, S. (2017b). Na-doped $LiMnPO_4$ as an electrode material for enhanced lithium ion batteries. *Bulletin of Materials Science*, *40*(1), 171-175.

Raju, K., & Ozoemena, K. I. (2015). Hierarchical one-dimensional ammonium nickel phosphate microrods for high-performance pseudocapacitors. *Scientific Reports*, *5*, 17629.

Reddy, C. S. K., Khan, K. K. A., & Nagaraja, C. (2016). A review on the determination of melting point measurement system. *International Journal of Advanced Research in Electrical, Electronics and Instrumentation Engineering*, *5*(2), 975-979.

Satapathy, S., Ahlawat, A., Paliwal, A., Singh, R., Singh, M. K., & Gupta, P. K. (2014). Effect of calcination temperature on nanoparticle morphology and its consequence on optical properties of Nd:Y_2O_3 transparent ceramics. *CrystEngComm*, *16*(13), 2723-2731.

Shirakawa, H., Louis, J., & Macdiarmid, A. G. (1977). Synthesis of electrically conducting organic polymers : halogene derivatives of polyacetylene, $(CH)_x$. *Journal of the Chemical Society, Chemical Communications*, *16*, 578-580.

Song, E., & Choi, J. W. (2013). Conducting polyaniline nanowire and its applications in chemiresistive sensing. *Nanomaterials*, *3*(3), 498-523.

Stachurski, Z. H. (2011). On structure and properties of amorphous materials. *Materials*, *4*(9), 1564-1598.

Stejskal, J., Sapurina, I., & Trchová, M. (2010). Polyaniline nanostructures and the role of aniline oligomers in their formation. *Progress in Polymer Science (Oxford)*, *35*(12), 1420-1481.

Taurozzi, J. S., Hackley, V. A., & Wiesner, M. R. (2011). Ultrasonic dispersion of nanoparticles for environmental, health and safety assessment - issues and recommendations. *Nanotoxicology*, *5*(4), 711-729.

Thomas, S., & Zaikov, G. E. (2008). *Polymer nanocomposite research advances*. Nova Publishers.

Tong, Z., Yang, Y., Wang, J., Zhao, J., Su, B. L., & Li, Y. (2014). Layered polyaniline/graphene film from sandwich-structured polyaniline/graphene/polyaniline nanosheets for high-performance pseudosupercapacitors. *Journal of Materials Chemistry A*, *2*(13), 4642-4651.

Tran, R., Xu, Z., Radhakrishnan, B., Winston, D., Sun, W., Persson, K. A., & Ong, S. P. (2016). Surface energies of elemental crystals. *Scientific data*, *3*, 160080.

Uchaker, E., Zheng, Y. Z., Li, S., Candelaria, S. L., Hu, S., & Cao, G. Z. (2014). Better than crystalline : amorphous vanadium oxide for sodium-ion batteries. *Journal of Materials Chemistry A*, *2*, 18208-18214.

Umeshbabu, E., Rajeshkhanna, G., Justin, P., & Rao, G. R. (2015). Synthesis of mesoporous $NiCo_2O_4$-rGO by a solvothermal method for charge storage applications. *RSC Advances*, *5*(82), 66657-66666.

Vadivel, S., Maruthamani, D., Kumaravel, M., Saravanakumar, B., Paul, B., Sankar, S., & Muthuraj, V. (2017). Supercapacitors studies on $BiPO_4$ nanoparticles synthesized via a simple microwave approach. *Journal of Taibah University for Science*, *11*(4), 661-666.

Veerasubramani, G. K., Krishnamoorthy, K., & Kim, S. J. (2016). Improved electrochemical performances of binder-free $CoMoO_4$ nanoplate arrays@Ni foam electrode using redox additive electrolyte. *Journal of Power Sources*, *306*, 378-386.

Wang, J., Dong, S., Ding, B., Wang, Y., Hao, X., Dou, H., & Zhang, X. (2017). Pseudocapacitive materials for electrochemical capacitors: from rational synthesis to capacitance optimization. *National Science Review*, *4*(1), 71-90.

Wang, Q., Du, J., Zhu, Y., Yang, J., Chen, J., Wang, C., & Jiao, L. (2015). Facile fabrication and supercapacitive properties of mesoporous zinc cobaltite microspheres. *Journal of Power Sources*, *284*, 138-145.

Wang, R., Lang, J., Liu, Y., Lin, Z., & Yan, X. (2015). Ultra-small, size-controlled $Ni(OH)_2$ nanoparticles : elucidating the relationship between particle size and electrochemical performance for advanced energy storage devices. *NPG Asia Materials*, *7*(6), 183-187.

Wang, T., Hao, Q., Liu, J., Zhao, J., Bell, J., & Wang, H. (2016). High capacitive amorphous barium nickel phosphate nanofibers for electrochemical energy storage. *RSC Advances*, *6*(51), 45986-45992.

Wang, Y., Song, Y., & Xia, Y. (2016). Electrochemical capacitors: mechanism, materials, systems , characterization and applications. *Chemical Society Reviews*, *45*(21), 5925-5950.

Wei, X., Chen, D., & Tang, W. (2007). Preparation and characterization of the spinel oxide $ZnCo_2O_4$ obtained by sol-gel method. *Materials Chemistry and Physics*, *103*(1), 54-58.

Wu, H. Y., & Wang, H. W. (2012). Electrochemical synthesis of nickel oxide nanoparticulate films on nickel foils for high-performance electrode materials of supercapacitors. *International Journal of Electrochemical Science*, *7*(5), 4405-4417.

Xiao, H., Qu, F., & Wu, X. (2016). Ultrathin NiO nanoflakes electrode materials for supercapacitors. *Applied Surface Science, 360*, 8-13.

Xu, H., Zeiger, B. W., & Suslick, K. S. (2013). Sonochemical synthesis of nanomaterials. *Chemical Society Reviews, 42*, 2555-2567.

Xu, M. W., Zhao, D. D., Bao, S. J., & Li, H. L. (2007). Mesoporous amorphous MnO_2 as electrode material for supercapacitor. *Journal of Solid State Electrochemistry, 11*(8), 1101-1107.

Xu, S., Li, X., Yang, Z., Wang, T., Jiang, W., Yang, C., & Zhang, Y. (2016). Nanofoaming to boost the electrochemical performance of $Ni@Ni(OH)_2$ nanowires for ultrahigh volumetric supercapacitors. *ACS Applied Materials & Interfaces, 8*, 27868-27876.

Yan, J. (2015). *Handbook of clean energy systems*. John Wiley & Sons.

Yang, J., Tan, J., Yang, F., Li, X., Liu, X., & Ma, D. (2012). Electro-oxidation of methanol on mesoporous nickel phosphate modified GCE. *Electrochemistry Communications, 23*(1), 13-16.

Yaning, W., Kang, W., & Xitao, W. (2016). Preparation of $Ag_3PO_4/Ni_3(PO_4)_2$ hetero-composites by cation exchange reaction and its enhancing photocatalytic performance. *Journal of Colloid and Interface Science*, *466*, 178-185.

Yun, G., Guan, Q., & Li, W. (2017). The synthesis and mechanistic studies of a highly active nickel phosphide catalyst for naphthalene hydrodearomatization. *RSC Advances*, *7*(14), 8677-8687.

Zequine, C., Ranaweera, C. K., Wang, Z., Singh, S., Tripathi, P., Srivastava, O. N., & Gupta, R. K. (2016). High performance and flexible supercapacitors based on carbonized bamboo fibers for wide temperature applications. *Scientific Reports*, *6*, 31704.

Zhao, J., Wang, S., Run, Z., Zhang, G., Du, W., & Pang, H. (2015). Hydrothermal synthesis of nickel phosphate nanorods for high-performance flexible asymmetric all-solid-state supercapacitors. *Particle & Particle Systems Characterization*, *32*(9), 880-885.

Zheng, C., Yang, H., & Yang, Y. (2017). Pseudocapacitive behavior of Ag_3PO_4 nanospheres prepared by a sonochemical process. *Materials Transactions*, *58*(2), 298-301.

Zhong, C., Deng, Y., Hu, W., Qiao, J., Zhang, L., & Zhang, J. (2015). A review of electrolyte materials and compositions for electrochemical supercapacitors. *Chemical Society Reviews, 44*(21), 7484-7539.

Zhu, Y., Ji, X., Wu, Z., Song, W., Hou, H., Wu, Z., & Banks, C. E. (2014). Spinel $NiCo_2O_4$ for use as a high-performance supercapacitor electrode material: understanding of its electrochemical properties. *Journal of Power Sources, 267*, 888-900.

LIST OF PUBLICATIONS AND PAPER PRESENTED

Omar, F. S., Numan, A., Duraisamy, N., Bashir, S., Ramesh, K., & Ramesh, S. (2016). Ultrahigh capacitance of amorphous nickel phosphate for asymmetric supercapacitor applications. *RSC Advances*, *6*(80), 76298-76306.

Omar, F. S., Numan, A., Bashir, S., Duraisamy, N., Vikneswaran, R., Loo, Y.L, Ramesh, K., & Ramesh, S. (2018). Enhancing rate capability of amorphous nickel phosphate supercapattery electrode via composition with crystalline silver phosphate. *Electrochimica Acta*, *273*, 216-228.

Omar, F. S., Numan, A., Duraisamy, N., Bashir, S., Ramesh, K., & Ramesh, S. (2017). A promising binary nanocomposite of zinc cobaltite intercalated with polyaniline for supercapacitor and hydrazine sensor. *Journal of Alloys and Compounds*, *716*, 96-105.

Omar, F. S., Numan, A., Duraisamy, N., Ramly, M. M., Ramesh, K., & Ramesh, S. (2017). Binary composite of polyaniline/copper cobaltite for high performance asymmetric supercapacitor application. *Electrochimica Acta*, *227*, 41-48.

Omar, F. S., Duraisamy, N., Ramesh, K., & Ramesh, S. (2016). Conducting polymer and its composite materials based electrochemical sensor for Nicotinamide Adenine Dinucleotide (NADH). *Biosensors and Bioelectronics*, *79*, 763-775.

Other publications

Lee, C. C., **Omar, F. S.**, Numan, A., Duraisamy, N., Ramesh, K., & Ramesh, S. (2017). An enhanced performance of hybrid supercapacitor based on polyaniline-manganese phosphate binary composite. *Journal of Solid State Electrochemistry*, *21*(11), 3205-3213.

Nadiah, N. S., **Omar, F. S.**, Numan, A., Mahipal, Y. K., Ramesh, S., & Ramesh, K. (2017). Influence of acrylic acid on ethylene carbonate/dimethyl carbonate based liquid electrolyte and its supercapacitor application. *International Journal of Hydrogen Energy*, *42*(52), 30683-30690.

Duraisamy, N., Numan, A., **Omar, F. S.**, Ramesh, K., & Ramesh, S. (2016). Facile sonochemical synthesis of nanostructured NiO with different particle sizes and its electrochemical properties for supercapacitor application. *Journal of Colloid and Interface Science*, *471*, 136-144.

Numan, A., Duraisamy, N., **Omar, F. S.**, Mahipal, Y. K., Ramesh, K., & Ramesh, S. (2016). Enhanced electrochemical performance of cobalt oxide nanocube intercalated reduced graphene oxide for supercapacitor application. *RSC Advances*, *6*, 34894-34902.

Bidin, M. Z., Ng, H. M.., **Omar, F. S.**, Ramesh, K., & Ramesh, S. (2018). Solid terpolymer electrolyte based on poly(vinyl butyral-co-vinyl alcohol-co-vinyl acetate) incorporated with lithium salt and tetraglyme for EDLCs. *Journal of Applied Polymer Science*, *135*(8), 1-7.

Numan, A., Duraisamy, N., **Omar, F. S.**, Gopi, D., Ramesh, K., & Ramesh, S. (2017). Sonochemical synthesis of nanostructured nickel hydroxide as an electrode material for improved electrochemical energy storage application. *Progress in Natural Science: Materials International*, *27*(4), 416-423.

Numan, A., Shahid, M. M., **Omar, F. S.**, Rafique, S., Bashir, S., Ramesh, K., & Ramesh, S. (2017). Binary nanocomposite based on Co_3O_4 nanocubes and multiwalled carbon nanotubes as an ultrasensitive platform for amperometric determination of dopamine. *Microchimica Acta*, *184*(8), 2739-2748.

Numan, A., Shahid, M. M., **Omar, F. S.**, Ramesh, K., & Ramesh, S. (2017). Facile fabrication of cobalt oxide nanograin-decorated reduced graphene oxide composite as ultrasensitive platform for dopamine detection. *Sensors and Actuators B: Chemical*, *238*, 1043-1051.

Chan, X., Khanmirzaei, M. H., **Omar, F. S.**, Ramesh, K., & Ramesh, S. (2017). Enhanced efficiency in dye-sensitized solar cell based on zinc oxide-modified poly (ethylene oxide) gel electrolyte. *Ionics*, *24*(4), 1221-1226.

Farhana, N. K., Khanmirzaei, M. H., **Omar, F. S.**, Ramesh, S., & Ramesh, K. (2017). Ionic conductivity improvement in poly (propylene) carbonate-based gel polymer electrolytes using 1-butyl-3-methylimidazolium iodide (BmimI) ionic liquid for dye-sensitized solar cell application. *Ionics*, *23*(6), 1601-1605.

Chan, X. H., Khanmirzaei, M. H., **Omar, F. S.**, Ramesh, K., & Ramesh, S. (2018). Enhanced efficiency in dye-sensitized solar cell based on zinc oxide-modified poly (ethylene oxide) gel electrolyte. *Ionics*, *24*(4), 1221-1226.

Chew, J. W., Khanmirzaei, M. H., Numan, A., **Omar, F. S.**, Ramesh, K., & Ramesh, S. (2018). Performance studies of ZnO and multi walled carbon nanotubes-based counter electrodes with gel polymer electrolyte for dye-sensitized solar cell. *Materials Science in Semiconductor Processing*, *83*, 144-149.

Paper presented in conference

Omar, F. S., K. Ramesh, S. Ramesh (2017). Nickel phosphate-silver phosphate nanocomposite based electrode material for hybrid supercapacitor. Paper presented at the International Symposium on Advanced material Research (ISAMR 2017), Seoul, South Korea.